

PULSED SPIN LOCKING IN SPIN-1 NQR:
BROADENING MECHANISMS

by

Michael W. Malone

A Dissertation

Submitted to the

Graduate Faculty

of

George Mason University

In Partial Fulfillment of

The Requirements for the Degree

of

Doctor of Philosophy

Physics

Committee:

_____ Dr. Karen L. Sauer, Dissertation Director

_____ Dr. Robert Honeychuck, Committee
Member

_____ Dr. Yuri Mishin, Committee Member

_____ Dr. Erhai Zhao, Committee Member

_____ Dr. Michael Summers, Director, School of
Physics, Astronomy, and Computational
Sciences

_____ Dr. Timothy L. Born, Associate Dean
for Student and Academic Affairs,
College of Science

_____ Dr. Peggy Agouris, Interim Dean,
College of Science

Date: _____ Summer 2013
George Mason University
Fairfax, VA

Pulsed Spin Locking in Spin-1 NQR: Broadening Mechanisms

A dissertation submitted in partial fulfillment of the requirements for the degree of
Doctor of Philosophy at George Mason University

By

Michael W. Malone
Master of Science
George Mason University, 2011
Bachelor of Arts
St. John's College, 2004

Director: Dr. Karen L. Sauer, Professor
School of Physics, Astronomy, and Computational Sciences

Summer 2013
George Mason University
Fairfax, VA

Copyright © 2013 by Michael W. Malone
All Rights Reserved

Acknowledgments

I'd like to sincerely thank my adviser, Dr Karen L. Sauer. Thank you to George Mason University and the National Science Foundation for funding.

Table of Contents

	Page
List of Tables	vi
List of Figures	vii
Abstract	xi
1 Introduction	1
2 A Theoretical Background of NQR	7
2.1 The Quadrupole Hamiltonian	7
2.2 Fictitious Spin 1/2 Operators and the Rotating Frame	13
2.3 Signal Creation	17
2.4 The Basics of Signal Detection	22
2.5 Pulsed Spin Locking	27
3 Experimental	31
3.1 Experimental Equipment	31
3.2 Experimental Procedure	35
3.3 Automation	39
4 Homonuclear Dipolar Coupling Revealed	41
4.1 Introduction	41
4.2 Theory	42
4.3 Experimental procedure	53
4.4 Experimentally achieving the 180° condition for finite pulses	54
4.5 Experimental Results	57
4.6 Conclusion	65
5 The Role of Imperfect Pulses	68
6 Heteronuclear Dipolar Coupling	76
6.1 Introduction	76
6.2 Theory	77
6.2.1 Evolution	78
6.2.2 The observable	85

6.2.3	Initial density matrix	87
6.3	Experimental procedure	90
6.4	Results	91
6.5	Conclusion	97
7	Conclusions	98
A	The solution to $U = e^{i\theta\mathbf{I}\cdot\hat{\mathbf{b}}}(\mathbf{I}\cdot\hat{\mathbf{a}})e^{-i\theta\mathbf{I}\cdot\hat{\mathbf{b}}}$	100
B	FID processing	103
C	SLSE processing	108
D	A Low Power NQR System	110
D.1	Overview	110
D.2	Abstract	110
D.3	Introduction	110
D.4	The system in detail	111
D.5	Experimental details and observations	119
D.6	Conclusion	121
E	Example Visual Basic Script for Tecmag Automation	123
E.1	Overview	123
F	Java processing code	129
F.1	Overview	129
F.2	Example Code	129
G	A .tnt reader	132
G.1	Overview	132
G.1.1	TNT Class	132
G.1.2	TNTreader Class	132
	Bibliography	137

List of Tables

Table	Page	
2.1	The sums for the general values of θ are on the order of unity,[69] unless θ is small and no evolution takes place between echoes.	28
3.1	The coil parameters for the experiments using sodium nitrite and p-chloroaniline.	31
4.1	The relationship between H_{rf} and H_Q suggests the definition of two fictitious spin-1/2 angular momentum operators, $\mathbf{I}^W = (I_1^W \hat{i}, I_2^W \hat{j}, I_3^W \hat{k})$ and $\mathbf{I}^V = (I_1^V \hat{i}, I_2^V \hat{j}, I_3^V \hat{k})$ which are expressed in terms of the Dirac matrices.	44
4.2	The predicted value of $\Delta\omega$, from Eq. (4.27), and also $T_d = \frac{1}{\sqrt{\langle \Delta\omega^2 \rangle_W}}$ for both a single crystal and a powder under a 90-180 sequence.	53
4.3	The observed full width at half maximum (FWHM) linewidths for both samples at the three NQR transition frequencies show that the broad sample has a larger linewidth for all three frequencies.	54
4.4	The τ dependency of T_{2e} was found by fitting the observed values of T_{2e} at each τ value to Eq. (4.32) for $\Delta f = 0$ for both 90-180 and 90-90 SLSEs with the narrow sample.	63
6.1	The NQR signals from numerous resonant FIDs were averaged together and fit to a Voigt function, Eq. (6.51).	94

List of Figures

Figure	Page	
1.1	In a common NMR system a splitting in energy levels is achieved by placing a spin 1/2 nucleus into a static field B_0	2
1.2	A comparison of the NQR signals acquired from an FID and a SLSE shows a considerable increase in the amount of signal that can be acquired with the SLSE.	3
2.1	A representative FID signal (a), with the origin of time being the end of the rf pulse, decays primarily due to the distribution in ω_x among the various nuclei.	24
2.2	The predicted off-resonant signal (solid lines) calculated using Eqs. (2.62)-(2.63) are compared to the observed signals (dots) for $\theta = 90^\circ$ using two different excitation pulse lengths, 165 and 52 μs	26
2.3	A projection model, Eq. (2.79) that only includes off-resonance effects (thick light lines) does a very good predicting the real signal behavior (dots and thin lines) of the 90-90 sequence on the left.	30
3.1	The circuit diagram generalized for the experiments described in this thesis.	32
3.2	A picture of the actual configuration of the probe circuitry for sodium nitrite experiments shows the experimental simplicity possible with NQR.	33
3.3	The NQR frequency found using the two FIDs (black line) compared to the NQR frequency determined by processing a SLSE signal (red line).	36
3.4	Plots of the data obtained from 204 resonant FIDs taken over 28 consecutive hours.	37
4.1	The eigenenergies are shown for spin- a and spin- b where $ x\rangle$, $ y\rangle$, $ z\rangle$ correspond to the eigenstates of the quadrupole Hamiltonian.	43

4.2	The signal from a 90-90 SLSE sequence is shown for both on-resonance ($\Delta f = 0$) and off-resonance ($\Delta f = 1/(4\tau')$) conditions.	49
4.3	The theoretical (a)-(c) and experimental data (d)-(f) are compared with off-resonance for both 90-90 and 90-180 sequences, the left and right halves of each image respectively, for three values of τ	58
4.4	The percent of the decay in the echo train due to the Gaussian component p_g (a)-(c) and width of the Gaussian contribution T_d (d)-(f) as a function of τ for 90-180 sequences applied at the three transition frequencies.	61
4.5	The value of T_{2e} for 90-180 (black squares) and 90-90 (red triangles) sequences is consistently greater when $\Delta f = 0$ (solid line and symbols) than for $ \Delta f = \frac{1}{4\tau'}$ (dashed line and hollow symbols).	62
4.6	The optimal SNR calculated by integrating Eq. (4.29) for both 90-90 (red) and 90-180 (black) sequences with the experimentally derived fit parameters at ω_y for both the narrow (top row) and broad (bottom row) sample.	64
5.1	A plot of the average signal over 125 ms vs $\Delta f \cdot \tau'$ for fixed τ (335 μ s) shows that the asymmetry between $\Delta f = \pm \frac{1}{4\tau'}$ was reduced by lowering the \mathcal{Q} of the probe.	69
5.2	For $\Delta f = 0$ the echo trains (a) with high \mathcal{Q} (\mathcal{Q}_H , hollow red squares) and low \mathcal{Q} (\mathcal{Q}_L , black circles) are similar, despite their respective pulse shapes, (b) and (c), having very different real (dashed) and imaginary (green solid) components.	70
5.3	(Left) The echo trains (a) show that for a high \mathcal{Q} (\mathcal{Q}_H) probe a strong Gaussian component appeared at $\Delta f = +\frac{1}{4\tau'}$ (blue squares) whose width is somewhat below the prediction from Table 4.2.	71
5.4	Average signal (a) and strength of the Gaussian contribution of the echo train (b) versus p_{th} , the calculated percent of the initial signal due to spins experiencing a 180° net rotation.	72
5.5	The real (black) and imaginary (red) components of an actual (dashed) and simplified (solid) refocusing pulse shape.	74

6.1	The 90-90 SLSE signal on the left (red dots) due a standard sequence has a stronger response as a function of Δf than a nearly identical sequence on the right (black dots).	88
6.2	The fit parameters obtained from the 90-180 SLSE echo trains using Eq. (4.29) for various τ s at $\Delta f = -1/(4\tau')$ for both S1 (thin black line, squares) and S3 (thick red lines, circles).	92
6.3	The average 90-90 SLSE signals (black squares) obtained from the first 63 ms of echoes, to maximize SNR, from S2 for various values of τ' and for various off-resonances ($\Delta f \cdot \tau'$).	96
B.1	A visualization of the typical FID processing necessary to calculate the off-resonance and the phase of the signal, where red corresponds to the real component of the signal, green to the imaginary, and blue to the magnitude.	104
B.2	Calculations of Δf and the FID's phase made using match filtering (thick black lines) show less variation than the same calculations performed without match filtering (thin red lines).	105
B.3	A visualization of the FID processing used to obtain the back projected intercept and lineshape, where red corresponds to the real component of the signal, green to the imaginary, and blue to the magnitude.	107
C.1	A representative view of the first 10 echoes acquired during a SLSE sequence.	108
D.1	An overview of a typical NQR system.	111
D.2	The image on the left shows the shielded processing box holding the A2D, the class-D amplifier, and the FPGA located directly under the amplifier.	112
D.3	A schematic of the main components of the circuitry is shown in A.	114
D.4	The excitation pulse of the class-D amplifier observed using the sniffer coil reveals a difference in the rise ($10.6 \pm 1.1 \mu\text{s}$) and fall ($6.3 \pm 0.1 \mu\text{s}$) times.	115
D.5	Signals obtained by toggling the MOSFETs into the low Q (dashed) and high Q (solid) configuration, as described in Fig. D.3, demonstrate that the Q switching is working.	117

D.6	The circuit diagram of the first preamplifier, showing the virtual short for the input terminal.	118
D.7	Three representative signals obtained with the system obtained after a single excitation pulse.	119
D.8	A comparison of calibration curves for two different filling factors: the ratio of sample volume to main coil volume.	120

Abstract

PULSED SPIN LOCKING IN SPIN-1 NQR: BROADENING MECHANISMS

Michael W. Malone, PhD

George Mason University, 2013

Dissertation Director: Dr. Karen L. Sauer

Nuclear Quadrupole Resonance (NQR) is a branch of magnetic resonance physics that allows for the detection of spin $I > 1/2$ nuclei in crystalline and semi-crystalline materials. Through the application of a resonant radio frequency (rf) pulse, the nuclei's response is to create an oscillating magnetic moment at a frequency unique to the target substance. This creates the NQR signal, which is typically weak and rapidly decaying. The decay is due to the various line broadening mechanisms, the relative strengths of which are functions of the specific material, in addition to thermal relaxation processes. Through the application of a series of rf pulses the broadening mechanisms can be refocused, narrowing the linewidth and extending the signal in time.

Three line broadening mechanisms are investigated to explain the NQR signal's linewidth and behavior. The first, electric field gradient (EFG) inhomogeneity, is due to variations in the local electric environment among the target nuclei, for instance from crystal imperfections. While EFG inhomogeneity can vary between samples of the same chemical composition and structure, the other broadening mechanisms of

homonuclear and heteronuclear dipolar coupling are specific to this composition and structure. Simple analytical models are developed that explain the NQR signal response to pulse sequences by accounting for the behavior of each broadening mechanism. After a general theoretical introduction, a model of pairs of spin-1 nuclei is investigated, and the refocusing behaviors of EFG and homonuclear dipolar coupling are analyzed. This reveals the conditions where EFG is refocused but homonuclear dipolar coupling is not. In this case the resulting signal shows a rapid decay, the rate of which becomes a measure of interatomic distances. This occurs even in the more complex case of a powder sample with its many randomly oriented crystallites, under particular pulsing conditions.

Many target NQR compounds are rich in hydrogen, and therefore might have a significant heteronuclear dipolar coupling component. To incorporate this, a second model is developed composed of two different nuclear species, one spin 1 the other spin 1/2, although the work can be extended to additional spin species. This model reveals that heteronuclear dipolar coupling for this system behaves just like EFG broadening under spin locking, and that the strong homonuclear response is still observable. The experimental results closely match theoretical predictions, and the conclusions greatly expand the number of target substances that are suitable for this measurement technique of homonuclear dipolar coupling.

The combined results explain why certain pulse sequences perform better than others for substance detection: it is because of the relative strengths of the line broadening mechanisms. Therefore the ability to measure homonuclear dipolar coupling's contribution to the linewidth is useful not only for material characterization, but also for substance detection. By explaining the conditions that reveal homonuclear coupling, we make it possible to measure the relative broadening strengths, increasing the efficiency of NQR in these roles.

Chapter 1: Introduction

Nuclear Quadrupole Resonance (NQR) is a magnetic resonance technique with many similarities to Nuclear Magnetic Resonance (NMR). As shown in Fig. 1.1, in NMR the interaction of a spin $1/2$ nuclei's magnetic moment with a static field B_0 produces an energy level splitting. Using a radio frequency (rf) pulse, an alternating magnetic field related to the splitting is detected with a magnetometer. Similarly, NQR exploits the energy splitting governed by a nuclei's electric quadrupole moment with its local electric field gradient (EFG) to produce an alternating magnetic field that can be detected with a magnetometer.[1,2] However, for NQR no static field and associated cooling is required since the energy levels of NQR are intrinsic to the substance being investigated. Consequently, the frequency of the NQR signal is a characteristic of the substance, which makes NQR a promising tool for substance detection.[3,4] However, there are many problems hindering the adoption of NQR as a tool. As discussed below, the target nuclei must be spin $> 1/2$, and the target substance must be a solid, preferably crystalline. The typical NQR frequency is on the order of MHz, and can not be increased with stronger fields as in NMR. The signals are weak, decay rapidly, fall off with distance as $1/r^3$, and T_1 can be long. There is a dependency of the signal strength with the alignment of the rf perturbation, which reduces the signal for powders to 43 % of the value from a crystal,[3] and makes optimal excitation for single crystals difficult.

With such a large number of challenges to overcome, the history of NQR has progressed relatively slowly compared to NMR. In 1950, Pound argued that theoretical

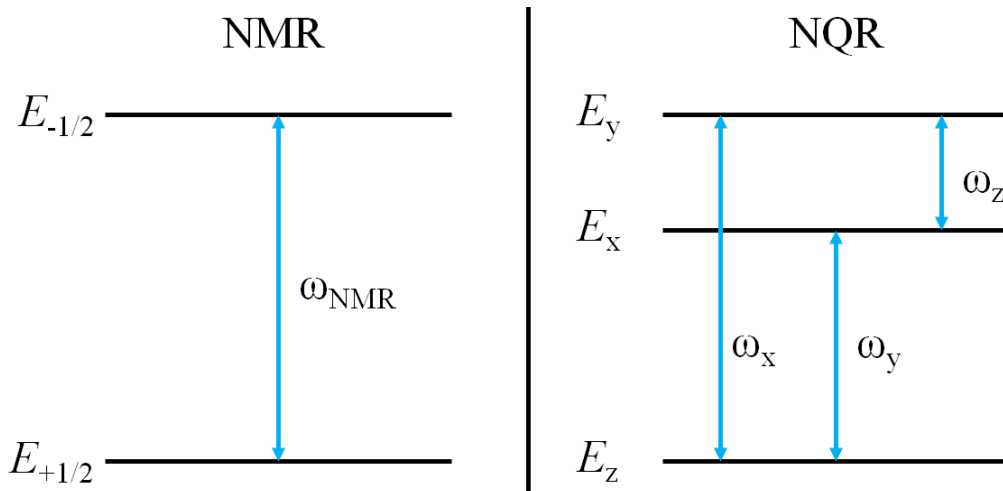


Figure 1.1: In a common NMR system a splitting in energy levels is achieved by placing a spin 1/2 nucleus into a static field B_0 . Resonant perturbations are then applied at a frequency ω_{NMR} related to the difference in the spin-up and spin-down energy states to produce a signal. In spin 1 NQR there are three energy levels, not necessarily distinct, and three corresponding resonant frequencies ω_{NQR} that can be used to create NQR signals.

results meant that the electrical quadrupole moment could dominate the nuclear resonance spectrum of crystals.[5] The same year, the first pure NQR signal was acquired by Dehmelt and Kruger. [6] Pulsed spin locking was applied in 1977 by Marino and Klainer[7] using the canonical spin-lock spin-echo (SLSE) sequence previously used in NMR in 1966.[8] As shown in Fig. 1.2, such a sequence makes NQR much more practical because it can greatly increase the amount of signal that can be acquired compared to that from a free induction decay (FID), the signal due to just a single pulse.

The theoretical work of Vega[9,10] and Cantor and Waugh[11] opened the possibility of using the NQR signal as a tool to analyze materials, and provided much of the operator formalism used in this thesis. Meanwhile, because of the NQR frequency's sensitivity to the molecular electrical environment, NQR has been investigated for many other practical uses including as a thermometer[12–14], a strain gauge,[15] and

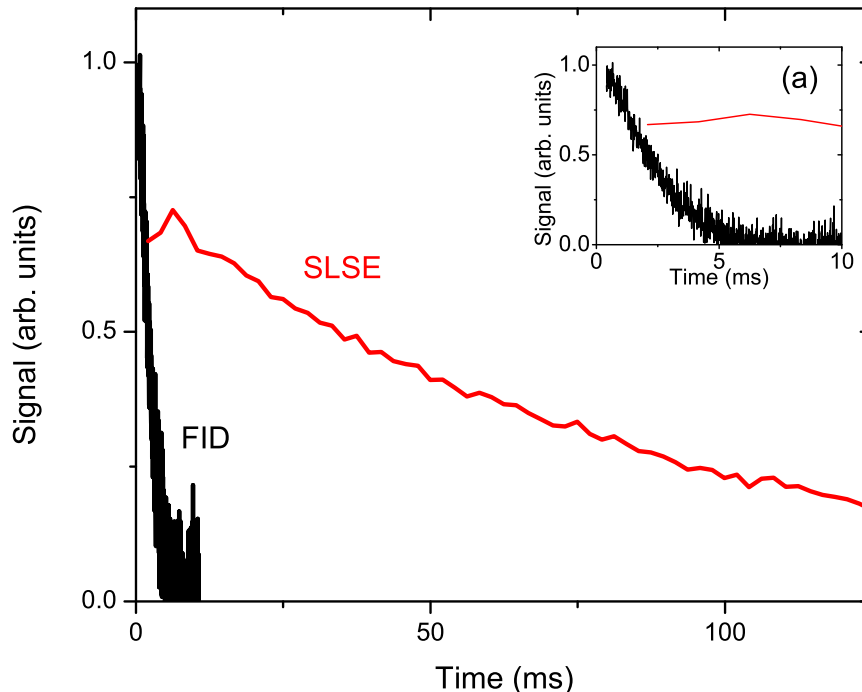


Figure 1.2: A comparison of the NQR signals acquired from an FID and a SLSE shows a considerable increase in the amount of signal that can be acquired with the SLSE. Zooming into the first 10 ms of data (a) shows more detail of the FID's rapid decay, which has an exponential decay constant T_2^* of about 2 ms. In contrast, the decay of the SLSE echo train is governed by an exponential decay constant T_{2e} near 88 ms. The signal is due to the ^{14}N nuclei of the narrow sample of sodium nitrite discussed in Chapter 2. The FID signal is due to a single pulse, and the 90-90 SLSE data is from a series of 60 refocusing pulses spaced $2 \cdot \tau' = 2 \cdot 1.012$ ms apart. Both sequences were resonant to ω_x . Data has been normalized for both experiments to the projected FID signal at $t=0$, as discussed in Appendix B.

as a probe of the electrical environment in superconductors.[16–18] But it has been most actively pursued for substance detection, where it is investigated for identifying counterfeit medicines,[19, 20] narcotics,[21–23] and especially explosives[3, 24–27].

Unfortunately, NQR’s utility is hindered by its typically low signal to noise ratio (SNR). In a highly cited paper Garroway et al. derived an expected SNR for TNT detection on the order of unity or below.[3] Because of this, much of the work in NQR has been in how to increase SNR. On the detection side, this has led to research in designing better antennas,[23, 28, 29] work with ultra-sensitive atomic magnetometers,[30] and advanced signal processing algorithms.[31–34] On the signal creation side, work has been done to excite the sample with multiple frequencies,[35–38] which can increase the amount of time that signal can be acquired. Continuous rf excitation has been suggested,[39, 40] since it allows for signal to be acquired without concern for T_1 . Single pulse echoes have been investigated because of their low power requirements.[41] Additionally, a large amount of work has been performed in double resonance experiments, where the nuclei of some other spin species, typically protons, interacts with the NQR target nuclei through combinations of static and rf fields. This can increase SNR and also allow the NQR target species to relax faster, decreasing T_1 and increasing the repeat rate of experiments.[42–45] Double resonance can also be used to efficiently find NQR frequencies, which is a very useful tool.[46, 47]

As shown in Fig. 1.2, another common way to increase SNR is through multi-pulse sequences. [48–52] Besides the SLSE, the Carr-Purcell Meiboom-Gill (CPMG) sequence has also been adapted from NMR for NQR.[53] Both have the same general form. First an excitation pulse θ_0 of duration t_0 creates the initial signal. This is followed by a series of refocusing pulses θ_1 , of duration t_p , shifted in phase by 90° from the excitation pulse. These SLSE sequences are written, for N repeat units, as

$\theta_{0y} - (\tau - \theta_{1x} - \tau)_N$, where 2τ is the time of the free evolution between the refocusing pulses; y and x refer to the phase of the pulses; and $\tau' = \tau + t_p/2$ will also be used to describe the pulse spacing. The signal is acquired stroboscopically at time τ after each refocusing pulse to create the echo train. The strength of the refocusing pulse varies depending on the desired signal response. Since they are so similar, both the SLSE and CPMG will be referred to as SLSEs: a 90-90 for the true SLSE and a 90-180 for the CPMG.

Previous researches have focused on the long time exponential decay of the echo train.[7,54,55] However, in a powder sample of sodium nitrite we unexpectedly found that certain experimental conditions with a 90-180 SLSE sequence provoked a strong, fast, Gaussian decay. The conditions under which this decay appears, as well as its initial intensity, are well explained with the theoretical argument presented in Chapter 4. It is the result of the homonuclear dipolar coupling not being refocused by the sequence while EFG inhomogeneity is refocused. This causes the envelope of the echo train to behave as though the signal decay was due primarily to the unrefocused dipolar coupling, an observation similar to that observed in NMR.[56–58] Therefore the width of this Gaussian component is a measurement of the homonuclear dipolar coupling within the sample.

The ability to measure the homonuclear dipolar coupling is very valuable for substance detection since its relative contribution to the linewidth determines the off-resonant behavior of the signal, as discussed in Chapter 4. Due to temperature variations of the target substance, the NQR resonance frequencies may only be known to within a certain range. This can result in off-resonant excitation, where the difference between the NQR frequency and the rf frequency,

$$\omega_{rf} - \omega_{NQR} \equiv \Delta\omega \equiv 2\pi\Delta f, \quad (1.1)$$

can cause undesired signals. For an example of the sensitivity of the frequency to temperature, a transition frequency for TNT can change 200 Hz per degree Celsius.[59] Therefore, knowing the behavior of the signal as a function of Δf allows for the optimization of the detection sequence to ensure working in a region of strong signal for the target substance and temperature range.

The work in Chapter 4 was performed on a sample that was not expected to have a large linewidth contribution from heteronuclear dipolar coupling. However, heteronuclear dipolar coupling should be present in a large class of samples important to NQR for substance detection,[9] consequently in Chapter 6 the theory is extended to a model that incorporates heteronuclear dipolar coupling. It is found that heteronuclear dipolar coupling behaves like EFG broadening under spin locking, and the experimental results show that the homonuclear response can still be observed for the same conditions as Chapter 4. Additional analysis of the lineshapes creates a possible procedure for isolating the three broadening mechanisms' contributions to the NQR lineshape.

The net results of the research described in this thesis are therefore relevant for a large set of problems in NQR. By being able to isolate the broadening mechanisms, the ability to fingerprint samples becomes possible. This could be useful to track a sample back to the manufacturer.[60] In particular, the ability to isolate EFG's contribution could make NQR a more useful tool in stress and strain detection. The ability to measure homonuclear dipolar coupling makes NQR a useful tool for analyzing new substances, such as designer narcotics.[61] Knowing how the various broadening mechanisms respond to multipulse sequences is critical for efficient substance detection.

Chapter 2: A Theoretical Background of NQR

2.1 The Quadrupole Hamiltonian

Exploiting the symmetry of the problem, no work is required to reorient a spherical charge distribution in an electric field gradient. But this is not true for a non-spherical charge distribution. Nuclear quadrupole resonance is a result of the work required to reorient non-spherical nuclei in the local electric field gradient of crystalline materials to produce an oscillating magnetic field that can be detected with a magnetometer. In order to introduce the theory of how an NQR signal is created and detected, we closely follow the derivation of the quadrupole Hamiltonian presented by Slichter.[62]

The interaction energy E of a charge distribution $\rho_c(\mathbf{r})$ in an electric potential $V(\mathbf{r})$, where $\mathbf{r} = r\hat{r}$ is the position vector from the origin, is given by

$$E = \int \rho_c(\mathbf{r})V(\mathbf{r})dv. \quad (2.1)$$

Expanding $V(\mathbf{r})$ in a Taylor series about the origin

$$V(\mathbf{r}) = V(0) + \sum_{\alpha} \alpha V_{\alpha} + \frac{1}{2} \sum_{\alpha, \beta} \alpha\beta V_{\alpha\beta} + \dots, \quad (2.2)$$

where α and β can be x , y , or z ; $V_{\alpha} \equiv \frac{\partial V}{\partial \alpha}$ and $V_{\alpha\beta} \equiv \frac{\partial^2 V}{\partial \alpha \partial \beta}$. This allows equation Eq. (2.1) to be rewritten as

$$E = V(0) \int \rho_c(\mathbf{r})dv + \sum_{\alpha} V_{\alpha} \int \alpha \rho_c(\mathbf{r})dv + \frac{1}{2} \sum_{\alpha, \beta} V_{\alpha\beta} \int \alpha\beta \rho_c(\mathbf{r})dv + \dots \quad (2.3)$$

The first term $V(0) \int \rho_c(\mathbf{r})dv$ is just the energy of the nucleus as a point charge. If $\rho_c(\mathbf{r})$ is centered on the origin, the second, or electric dipole, term $\sum_{\alpha} V_{\alpha} \int \alpha \rho_c(\mathbf{r})dv$ is expected to vanish for nuclei, although this is an area of active research.[63] The third term

$$E^{(2)} = \frac{1}{2} \sum_{\alpha, \beta} V_{\alpha\beta} \int \alpha\beta \rho_c(\mathbf{r})dv \quad (2.4)$$

is the quadrupole term and can be simplified by working in a coordinate system $\hat{x}, \hat{y}, \hat{z}$ where $V_{\alpha\beta} = 0$ for $\alpha \neq \beta$. This defines the principal axis frame (PAF) of the EFG tensor, with the additional requirement $|V_{zz}| \geq |V_{yy}| \geq |V_{xx}|$. [64]

In order to remove the spherically symmetric component of the quadrupole term, the $Q_{\alpha\alpha}$ are introduced

$$Q_{\alpha\alpha} = \int (3\alpha^2 - r^2)\rho_c(\mathbf{r})dv. \quad (2.5)$$

These terms deserve closer analysis. For a purely spherical charge distribution with radius R , $Q_{\alpha\alpha} = 0$ for all α . This establishes that the $Q_{\alpha\alpha}$ are a measure of how the charge distribution varies compared to a sphere, since a spherical part of $\rho_c(\mathbf{r})$, centered on the origin, could be removed without changing the value of $Q_{\alpha\alpha}$. For a one dimensional line charge along the x axis between $x = \pm l$, $\frac{4}{3}l^3 \propto Q_{xx}$ and $Q_{xx} = -2Q_{yy} = -2Q_{zz}$. This suggests that the largest $Q_{\alpha\alpha}$ corresponds to the axis

of symmetry of a charge distribution.

The $Q_{\alpha\alpha}$ allow Eq. (2.4) to be rewritten as

$$E^{(2)} = \frac{1}{6} \sum_{\alpha} \left(V_{\alpha\alpha} Q_{\alpha\alpha} - V_{\alpha\alpha} \int r^2 \rho_c(\mathbf{r}) dv \right). \quad (2.6)$$

Because the sum of the $V_{\alpha\alpha}$ is zero by Laplace's equation, and since $\int r^2 \rho_c(\mathbf{r}) dv$ in Eq. (2.6) is independent of $V_{\alpha\alpha}$, $E^{(2)}$ can be expressed as

$$E^{(2)} = \frac{1}{6} \sum_{\alpha} V_{\alpha\alpha} Q_{\alpha\alpha}, \quad (2.7)$$

which provides the quadrupole energy for a classical system.

In order to analyze this system quantum mechanically, the $Q_{\alpha\alpha}$ need to be converted into operators $Q_{\alpha\alpha}^{(op)}$. The charge distribution is given by the location of the nuclei's protons at location \mathbf{r}_p with charge e

$$\rho_c^{(op)}(\mathbf{r}) = e \sum_{\text{protons}} \delta(\mathbf{r} - \mathbf{r}_p), \quad (2.8)$$

which allows $Q_{\alpha\alpha}^{(op)}$ to be expressed as

$$Q_{\alpha\alpha}^{(op)} = e \sum_{\text{protons}} (3\alpha^2 - r^2) \delta(\mathbf{r} - \mathbf{r}_p). \quad (2.9)$$

Through application of the Wigner-Eckart theorem, the position operators of Eq. (2.9) can be rewritten in terms of the angular momentum \mathbf{I} of the nucleus, with operators $\mathbf{I} \cdot \hat{i} = I_i$, for $i = x, y, z$. The $Q_{\alpha\alpha}^{(op)}$ become

$$Q_{\alpha\alpha}^{(op)} = C(3I_\alpha^2 - I^2),$$

where $C = \frac{eQ}{I(2I-1)}$, and the quadrupole moment Q is determined experimentally for each nucleus. Using the operator $Q_{\alpha\alpha}^{(op)}$, $E^{(2)}$ can be written as an operator to define the quadrupole Hamiltonian H_Q

$$H_Q = \frac{1}{6} \sum_{\alpha} V_{\alpha\alpha} Q_{\alpha\alpha}^{(op)} \quad (2.10)$$

$$= \frac{eQ}{6I(2I-1)} [V_{xx}(3I_x^2 - I^2) + V_{yy}(3I_y^2 - I^2) + V_{zz}(3I_z^2 - I^2)]. \quad (2.11)$$

For spin 0 and spin 1/2, $\langle Q_{\alpha\alpha}^{(op)} \rangle = 0$ for any wavefunction, revealing such nuclei have spherical symmetry and making $H_Q = 0$. In addition to the case where all $V_{\alpha\alpha} = 0$, which occurs in fluids where the average EFG is zero, and in certain crystalline solids where the symmetry of the structure leads to the same, the constraint on the spin of the nucleus further limits the target population for NQR to crystalline solids, and some plastics, containing nuclei with spin $I > 1/2$.

The focus in this thesis will be on spin 1, in particular the nuclei of ^{14}N , where there are three eigenvectors of H_Q , listed below in terms of the eigenstates of I_z :

$$|y\rangle = \frac{|+1\rangle + |-1\rangle}{\sqrt{2}} \quad (2.12)$$

$$|x\rangle = \frac{|+1\rangle - |-1\rangle}{\sqrt{2}} \quad (2.13)$$

$$|z\rangle = |0\rangle. \quad (2.14)$$

The corresponding eigenenergies E_y , E_x , E_z lead to three transition frequencies ω_{NQR} , such as $\omega_x = (E_y - E_z)/\hbar$, with cyclic permutation of x , y , z providing the others. The degenerate cases of Fig. 1.1 are not considered in this thesis. Since the transition frequencies are determined by the EFG, which are specific to the local electrical environment, the ω_{NQR} 's are nearly unique between substances. This makes NQR a useful tool for substance detection and studying the local electric environment of nuclei.

The eigenstates of H_Q permit simple expressions for certain operators in terms of back to back operators:

$$H_Q = E_x|x\rangle\langle x| + E_y|y\rangle\langle y| + E_z|z\rangle\langle z| \quad (2.15)$$

$$I_x = |y\rangle\langle z| + |z\rangle\langle y| \quad (2.16)$$

$$I_y = i|z\rangle\langle x| - i|x\rangle\langle z| \quad (2.17)$$

$$I_z = |x\rangle\langle y| + |y\rangle\langle x|. \quad (2.18)$$

The labeling of H_Q 's eigenstates with geometrical terms is not accidental; these eigenstates correspond to the axis of symmetry of the nuclei with regard to the PAF coordinate frame. For instance

$$\langle x|Q_{xx}^{(op)}|x\rangle = -2\langle x|Q_{yy}^{(op)}|x\rangle = -2\langle x|Q_{zz}^{(op)}|x\rangle, \quad (2.19)$$

which, using the example above for a classical charge distribution along \hat{x} , suggests that the axis of symmetry of the charge distribution in the $|x\rangle$ eigenstate is along the \hat{x} axis of the PAF.

While NQR is a product of electrical interactions, it is observed through measurement of the nuclei's magnetic field

$$\vec{B}_d(\mathbf{r}) = \frac{\mu_0 \gamma_I \hbar}{4\pi r^3} [\mathbf{I} - 3\hat{r}(\mathbf{I} \cdot \hat{r})], \quad (2.20)$$

where μ_0 is the permeability of free space, γ_I is the gyromagnetic ratio of the nucleus, and $\mathbf{r} = r\hat{r}$ is the distance from the nucleus to the observation point. Therefore, modeling the signal requires calculating the expectation values $\langle I_x \rangle$, $\langle I_y \rangle$, $\langle I_z \rangle$ as functions of time, which is done by following the evolution of the corresponding density matrix $\varrho(t)$, where $\langle I_i(t) \rangle = \text{Tr}[I_i \varrho(t)]$.

The evolution of $\varrho(t)$ is governed by the Hamiltonian H of the system through the Liouville equation

$$\dot{\varrho}(t) = \frac{i}{\hbar} [\varrho, H]. \quad (2.21)$$

For time independent Hamiltonians, the solution to Eq. (2.21) is

$$\varrho(t) = e^{-\frac{i}{\hbar} H t} \varrho_0 h.c. \quad (2.22)$$

where ϱ_0 is the initial density matrix at $t = 0$, and $h.c.$ is the Hermitian conjugate of the evolution operators to the left of the density matrix. For a statistical sample of isolated nuclei, the initial density matrix is given by the Boltzmann distribution

$$\varrho_0 = \frac{1}{Z} [e^{-E_x/kT} |x\rangle\langle x| + e^{-E_y/kT} |y\rangle\langle y| + e^{-E_z/kT} |z\rangle\langle z|] \quad (2.23)$$

where $Z = \sum_i e^{-E_i/kT}$, T is the temperature and k is Boltzmann's constant. In the high temperature limit this simplifies to

$$\varrho_0 = \frac{1}{3} \left[\mathbf{1} - \left(\frac{E_x}{kT} |x\rangle\langle x| + \frac{E_y}{kT} |y\rangle\langle y| + \frac{E_z}{kT} |z\rangle\langle z| \right) \right], \quad (2.24)$$

or just

$$\varrho_0 = \frac{1}{3} [\mathbf{1} - H_Q/kT], \quad (2.25)$$

where $\mathbf{1}$ is an identity operator.

In the absence of any other interactions, the Hamiltonian is just H_Q , which clearly commutes with the initial density matrix, making $\varrho(t) = \varrho_0$. Similarly the $\langle I_i(t) \rangle$ must be constant, and all can easily be shown to be

$$\langle I_i(t) \rangle = \text{Tr}[I_i \varrho_0] = 0. \quad (2.26)$$

Therefore, there is no observable magnetic field, like one would observe from an ordinary iron magnet, for such a sample of quadrupolar nuclei in thermal equilibrium. In order to extract useful information from a sample, a perturbation is required. However, in order to explain that behavior, some mathematical theory must be introduced.

2.2 Fictitious Spin 1/2 Operators and the Rotating Frame

As shown below, an rf perturbation with strength B , direction \hat{B} , frequency ω_{rf} , and phase ϕ , $\vec{B}_{rf}(t) = B\hat{B} \cos(\omega_{rf}t + \phi)$, can remove the target sample from thermal equilibrium to produce an observable signal. Adding the rf Hamiltonian H_{rf} to H_Q ,

the total Hamiltonian becomes

$$H = H_Q - \gamma_I \hbar (B_x I_x + B_y I_y + B_z I_z) \cos(\omega_{rf} t + \phi), \quad (2.27)$$

where $B_x = B \hat{B} \cdot \hat{x}$, etc. For ω_{rf} near ω_x , the focus of this chapter, the evolution of $\rho(t)$ is easily solved in the interaction representation of the dominant Hamiltonian $H_0 = \frac{\omega_{rf}}{\omega_x} H_Q$. Such an analysis reveals only the I_x term of H_{rf} will lead to any evolution of the system. Therefore only transitions between $|y\rangle$ and $|z\rangle$ are considered for ω_{rf} near ω_x . This transforms the problem from a three level one between the $|x\rangle, |y\rangle, |z\rangle$ eigenstates, into a two level problem between the $|y\rangle, |z\rangle$ eigenstates.

Temporarily ignoring the $|x\rangle$ eigenstate, Eq. (2.27) can be represented as an effective two level Hamiltonian H^* in matrix notation as

$$H^* = \begin{array}{c} \langle y| \\ \langle z| \end{array} \begin{array}{c} |y\rangle \\ |z\rangle \end{array} \begin{bmatrix} E_y & 0 \\ 0 & E_x \end{bmatrix} - \gamma_I \hbar B_x \cos(\omega_{rf} t + \phi) \begin{array}{c} \langle y| \\ \langle z| \end{array} \begin{array}{c} |y\rangle \\ |z\rangle \end{array} \begin{bmatrix} 0 & 1 \\ 1 & 0 \end{bmatrix}. \quad (2.28)$$

This has the same form as the canonical Hamiltonian for a spin 1/2 nuclei with gyromagnetic ratio γ_I in a static field $\vec{B}_0 = B_0 \hat{z}$ and rf field $\vec{B}_1 = B_1 \hat{x} \cos(\omega_{rf} t + \phi)$. [65, 66]

$$H = -\gamma_I \frac{\hbar}{2} \left(\begin{array}{c} | \uparrow \rangle \quad | \downarrow \rangle \\ \langle \uparrow | \begin{bmatrix} B_0 & 0 \\ 0 & -B_0 \end{bmatrix} \\ \langle \downarrow | \end{array} + B_1 \cos(\omega_{rf}t + \phi) \begin{array}{c} | \uparrow \rangle \quad | \downarrow \rangle \\ \langle \uparrow | \begin{bmatrix} 0 & 1 \\ 1 & 0 \end{bmatrix} \\ \langle \downarrow | \end{array} \right). \quad (2.29)$$

Eq. (2.28) can be rewritten in the form of the NMR problem, Eq. (2.29),

$$H^* = -\gamma_I \frac{\hbar}{2} \left(\begin{array}{c} |y\rangle \quad |z\rangle \\ \langle y| \begin{bmatrix} \omega_x/\gamma_I & 0 \\ 0 & -\omega_x/\gamma_I \end{bmatrix} \\ \langle z| \end{array} + 2B_x \cos(\omega_{rf}t + \phi) \begin{array}{c} |y\rangle \quad |z\rangle \\ \langle y| \begin{bmatrix} 0 & 1 \\ 1 & 0 \end{bmatrix} \\ \langle z| \end{array} \right) \quad (2.30)$$

where the zero point of energy has been set to $(E_z + E_y)/2$. Therefore, for the experimentalist, there is no difference in the observables between the NQR system and the system of the fictitious spin 1/2 with angular momentum \mathbf{I}_x . This is referred to as the NMR system and it has the visual simplicity the fictitious spin \mathbf{I}_x being rotated in a 3-d space according to

$$\frac{d\mathbf{I}_x}{dt} \propto \mathbf{I}_x \times \vec{B}_{tot}, \quad (2.31)$$

where $\vec{B}_{tot} = \vec{B}_0 + \vec{B}_1$.

To facilitate analysis, a set of fictitious spin 1/2 operators are defined. The first

three,

$$I_{x1} = \frac{1}{2}I_x = \frac{1}{2} \begin{array}{c} \langle y| \\ \langle z| \end{array} \begin{array}{cc} |y\rangle & |z\rangle \\ \left[\begin{array}{cc} 0 & 1 \\ 1 & 0 \end{array} \right] \end{array} \quad (2.32)$$

$$I_{x2} = \frac{1}{2}(I_y I_z + I_z I_y) = \frac{1}{2} \begin{array}{c} \langle y| \\ \langle z| \end{array} \begin{array}{cc} |y\rangle & |z\rangle \\ \left[\begin{array}{cc} 0 & i \\ -i & 0 \end{array} \right] \end{array} \quad (2.33)$$

$$I_{x3} = \frac{1}{2}(I_z^2 - I_y^2) = \frac{1}{2} \begin{array}{c} \langle y| \\ \langle z| \end{array} \begin{array}{cc} |y\rangle & |z\rangle \\ \left[\begin{array}{cc} 1 & 0 \\ 0 & -1 \end{array} \right], \end{array} \quad (2.34)$$

recreate the Pauli spin matrices from the operators of Eqs. (2.16)-(2.18). These operators are defined by the fictitious space $\hat{x}_1, \hat{x}_2, \hat{x}_3$ with $I_{x1} = \mathbf{I}_x \cdot \hat{x}_1$, etc. For the fictitious spin, \hat{x}_3 corresponds to the direction of the fictitious static field about which it precesses. The operator

$$I_{x4} = I_{y3} - I_{z3} = \frac{1}{2}(\mathbf{1} - 3|x\rangle\langle x|) \quad (2.35)$$

is required to reproduce H_Q

$$H_Q = \hbar(\omega_x I_{x3} + \omega'_x I_{x4}), \quad (2.36)$$

where $\omega'_x = \frac{1}{3}(-1 + \eta)\omega_Q$, $\eta = (V_{xx} - V_{yy})/V_{zz}$, and $\omega_Q = 3eV_{zz}Q/(4\hbar)$. The operators I_{yi} and I_{zi} can be found for transitions involving ω_y and ω_z , respectively, through the cyclic permutation of x, y, z in Eqs. (2.32)-(2.35), and setting $\omega'_y = -\frac{1}{3}(1 + \eta)\omega_Q$ and $\omega'_z = \frac{2}{3}\omega_Q$. I_{x4} clearly commutes with I_{x1}, I_{x2}, I_{x3} , which themselves commute like angular momentum operators when multiplied by \hbar , as would be expected from their origin in the Pauli spin matrices.

By breaking the fictitious \vec{B}_1 into two counter-rotating fields

$$\vec{B}_R = B_x \cos(\omega_{rf}t + \phi)\hat{x}_1 + B_x \sin(\omega_{rf}t + \phi)\hat{x}_2, \quad (2.37)$$

$$\vec{B}_L = B_x \cos(-\omega_{rf}t + \phi)\hat{x}_1 + B_x \sin(-\omega_{rf}t + \phi)\hat{x}_2, \quad (2.38)$$

depending on the sign of γ_I , it is natural to work in a reference frame rotating about \hat{x}_3 with frequency $\pm\omega_{rf}$. In such a frame either \vec{B}_R or \vec{B}_L will be static, while the other will be oscillating so quickly that it can be ignored, using the secular approximation. This rotating frame will be useful for providing simple intuitions into the system because it removes high frequency oscillations.

2.3 Signal Creation

To create a signal, the initial population is perturbed from thermal equilibrium with a brief rf pulse. During the pulse $H = H_Q + H_{rf}(t)$. Since H is not static, the evolution of the density matrix is not given by Eq. (2.22). By defining the dominant Hamiltonian $H_0 = \frac{\omega_{rf}}{\omega_x}H_Q$ and the perturbing Hamiltonian $H_1 = -\Delta H_Q + H_{rf}(t)$, where $\Delta H_Q = \frac{\Delta\omega}{\omega_x}H_Q$, the problem can be simplified by entering the interaction

representation of H_0 , where $\tilde{\varrho}(t) = e^{\frac{i}{\hbar}H_0t}\varrho(t)e^{-\frac{i}{\hbar}H_0t}$ and $\tilde{H}_a = e^{\frac{i}{\hbar}H_0t}H_a e^{-\frac{i}{\hbar}H_0t}$. In the interaction representation, the Liouville equation becomes

$$\dot{\tilde{\varrho}}(t) = \frac{i}{\hbar}[\tilde{\varrho}, \tilde{H}_1]. \quad (2.39)$$

If the secular terms of \tilde{H}_1 are time independent, the solution to Eq. (2.39) is given by

$$\tilde{\varrho}(t) = e^{-\frac{i}{\hbar}\tilde{H}_1t}\tilde{\varrho}_0e^{\frac{i}{\hbar}\tilde{H}_1t}, \quad (2.40)$$

where $\tilde{\varrho}_0 \equiv \tilde{\varrho}(t=0) = \varrho(t=0) \equiv \varrho_0$.

An explicit calculation of \tilde{H}_1 means finding $\Delta\tilde{H}_Q = \Delta H_Q$ and $\tilde{H}_{rf}(t)$. ΔH_Q is clearly time independent. Using the fictitious spin operators, the expression for \tilde{H}_{rf} is

$$\tilde{H}_{rf} = -2\gamma_I\hbar e^{\frac{i}{\hbar}H_0t}(B_xI_{x1} + B_yI_{y1} + B_zI_{z1})e^{-\frac{i}{\hbar}H_0t}\cos(\omega_{rf}t + \phi). \quad (2.41)$$

We start by focusing on the \tilde{I}_{x1} term:

$$\tilde{I}_{x1} = e^{\frac{i}{\hbar}H_0t}I_{x1}e^{-\frac{i}{\hbar}H_0t}\cos(\omega_{rf}t + \phi) \quad (2.42)$$

$$= e^{i\frac{\omega_{rf}}{\omega_x}(\omega_x I_{x3} + \omega'_x I_{x4})t}I_{x1}e^{-i\frac{\omega_{rf}}{\omega_x}(\omega_x I_{x3} + \omega'_x I_{x4})t}\cos(\omega_{rf}t + \phi). \quad (2.43)$$

The I_{x4} term commutes with I_{x1} and I_{x3} , therefore

$$\tilde{I}_{x1} = e^{i\omega_{rf}I_{x3}t}I_{x1}e^{-i\omega_{rf}I_{x3}t}\cos(\omega_{rf}t + \phi). \quad (2.44)$$

The angular momentum terms

$$e^{i\omega_{rf}I_{x3}t}I_{x1}e^{-i\omega_{rf}I_{x3}t} \quad (2.45)$$

can be expressed more generally as

$$e^{i\theta\mathbf{I}_x\cdot\hat{b}}(\mathbf{I}_x\cdot\hat{a})e^{-i\theta\mathbf{I}_x\cdot\hat{b}} = \mathbf{I}_x\cdot\hat{a}', \quad (2.46)$$

where \hat{a}' is found by rotating \hat{a} clockwise about \hat{b} through an angle θ , as shown in Appendix A, making

$$\hat{a}' = \cos\theta\hat{a} + (1 - \cos\theta)\hat{b}(\hat{b}\cdot\hat{a}) + \sin\theta(\hat{a}\times\hat{b}). \quad (2.47)$$

For Eq. (2.45) this has the effect of rotating \hat{x}_1 by the angle $\omega_{rf}t$ about \hat{x}_3 . Returning the cosine term and continuing the derivation

$$\tilde{I}_{x1} = (I_{x1}\cos\omega_{rf}t - I_{x2}\sin\omega_{rf}t)\cos(\omega_{rf}t + \phi) \quad (2.48)$$

$$= \frac{1}{4}[I_{x1}(e^{i\omega_{rf}t} + e^{-i\omega_{rf}t}) + iI_{x2}(e^{i\omega_{rf}t} - e^{-i\omega_{rf}t})](e^{i(\omega_{rf}t+\phi)} + e^{-i(\omega_{rf}t+\phi)}) \quad (2.49)$$

$$= \frac{1}{4}[I_{x1}(e^{-i\phi} + e^{i\phi}) + iI_{x2}(e^{-i\phi} - e^{i\phi})] \quad (2.50)$$

$$= \frac{1}{2}[I_{x1}\cos\phi - I_{x2}\sin\phi] \quad (2.51)$$

which is static. The same derivation performed for the \tilde{I}_{y1} and \tilde{I}_{z1} terms, however, does not yield any secular behavior. Setting $\cos\Psi = \hat{B}\cdot\hat{x}$, the surviving expression for \tilde{H}_1 is

$$\tilde{H}_1 = -\omega_1 \hbar (I_{x1} \cos \phi - I_{x2} \sin \phi) - \Delta H_Q, \quad (2.52)$$

where $\omega_1 = \gamma_I B \cos \Psi$. The density matrix at time t_0 in the interaction representation of H_0 becomes

$$\tilde{\varrho}(t_0) = e^{i[\omega_1(I_{x1} \cos \phi - I_{x2} \sin \phi) + \Delta H_Q]t_0} \frac{1}{3} [\mathbf{1} - H_Q/kT] h.c., \quad (2.53)$$

which seems quite involved. Fortunately, many of the terms simplify. The identity matrix will not contribute to the expectation value of Eq. (2.20) since the trace of all $I_i = 0$. Additionally, the I_{x4} terms in H_Q will not contribute to the expectation value because they commute with all the remaining terms, and their trace with the $I_{xi} = 0$. Introducing the reduced density $\varrho(t)$, with initial value $\varrho_0 = A_0 I_{x3}$, where $A_0 = \hbar \omega_x / 3kT$, the evolution due to the excitation pulse is easily expressed as

$$\tilde{\varrho}(t_0) = A_0 [e^{i\theta'_0 \mathbf{I}_x \cdot \hat{n}_0} (\mathbf{I}_x \cdot \hat{x}_3) e^{-i\theta'_0 \mathbf{I}_x \cdot \hat{n}_0}] = A_0 \mathbf{I}_x \cdot \hat{x}'_3 \quad (2.54)$$

where $\theta'_0 \hat{n}_0 = \theta_0 (\cos \phi \hat{x}_1 - \sin \phi \hat{x}_2) + \Delta \omega t_0 \hat{x}_3$, with $\theta_0 = \omega_1 t_0$. Taking an excitation pulse with $\phi = \pi/2$, making $\theta'_0 \hat{n}_0 = -\theta_0 \hat{x}_2 + \Delta \omega t_0 \hat{x}_3$, the evolution operators effectively rotate \hat{x}_3 in Eq. (2.54) to \hat{x}'_3 as

$$\hat{x}'_3 = \left[\cos \theta'_0 \hat{x}_3 + \sin \theta'_0 \frac{\theta_0}{\theta'_0} \hat{x}_1 + \frac{\Delta \omega t_0}{\theta'_0} (1 - \cos \theta'_0) \left(\frac{-\theta_0 \hat{x}_2 + \Delta \omega t_0 \hat{x}_3}{\theta'_0} \right) \right]. \quad (2.55)$$

The signal will be a function of $\langle I_{x1} \rangle$, $\langle I_{x2} \rangle$ and $\langle I_{x3} \rangle$ in the frame rotating at ω_{rf} about \hat{x}_3 . For I_{x1} this is simply

$$\langle \tilde{I}_{x1}(t) \rangle = Tr[\tilde{\varrho}(t)I_{x1}], \quad (2.56)$$

when ϱ is solved in the interaction representation of $H_0 = \frac{\omega_{rf}}{\omega_x} H_Q$. Similarly, the rotating frame components of I_{x2} and I_{x3} are

$$\langle \tilde{I}_{x2}(t) \rangle = Tr[\tilde{\varrho}(t)I_{x2}] \quad (2.57)$$

$$\langle \tilde{I}_{x3}(t) \rangle = Tr[\tilde{\varrho}(t)I_{x3}]. \quad (2.58)$$

After the pulse, using Eq. (2.55) the expectation value of $\langle \tilde{I}_{x1} \rangle$ is given by

$$\begin{aligned} \langle \tilde{I}_{x1}(t_0) \rangle &= Tr[I_{x1}\tilde{\varrho}(t_0)] \quad (2.59) \\ &= A_0 Tr \left[\cos \theta'_0 I_{x1} I_{x3} + \sin \theta'_0 \frac{\theta_0}{\theta'_0} I_{x1}^2 + \frac{\Delta\omega t_0}{\theta'_0} (1 - \cos \theta'_0) \left(\frac{-\theta_0 I_{x1} I_{x2} + \Delta\omega t_0 I_{x1} I_{x3}}{\theta'_0} \right) \right]. \end{aligned} \quad (2.60)$$

This contains three terms $Tr[I_{x1}^2]$, $Tr[I_{x1}I_{x2}]$, $Tr[I_{x1}I_{x3}]$, but only the $Tr[I_{x1}^2] = 0.5$ term is non-zero. With the density matrix expressed in terms of I_{xi} it is easy to see that $\langle I_y \rangle$ and $\langle I_z \rangle$ will also be zero for this transition, since their trace with the I_{xi} terms are also zero. This means that for transitions near ω_i only the I_i term survives. The value of I_x out of the rotating frame will be

$$\langle I_x(t_0 + t) \rangle = 2[\langle \tilde{I}_{x1}(t_0) \rangle \cos \omega_x t + \langle \tilde{I}_{x2}(t_0) \rangle \sin \omega_x t]. \quad (2.61)$$

Therefore the rf pulse has created an oscillating magnetic field with frequency ω_x that can be detected with a magnetometer. We stop to point out that back in the rotating

frame, the three components of \mathbf{I}_x after the excitation pulse are

$$\langle \tilde{I}_{x1}^0 \rangle = \frac{\hbar\omega_x}{6kT} \sin \theta'_0 \frac{\theta_0}{\theta'_0} \quad (2.62)$$

$$\langle \tilde{I}_{x2}^0 \rangle = -\frac{\hbar\omega_x}{6kT} \frac{\Delta\omega t_0 \theta_0}{(\theta'_0)^2} (1 - \cos \theta'_0) \quad (2.63)$$

$$\langle \tilde{I}_{x3}^0 \rangle = \frac{\hbar\omega_x}{6kT} \left(\cos \theta'_0 + \left(\frac{\Delta\omega t_0}{\theta'_0} \right)^2 (1 - \cos \theta'_0) \right). \quad (2.64)$$

This is interpreted as though \mathbf{I}_x has gone from being aligned entirely along \hat{x}_3 to having some component in the x_1x_2 -plane. These values will be useful for later derivations of the system's evolution.

2.4 The Basics of Signal Detection

For the system described here, the detector consists of the same coil of wire used to excite the sample. Through Faraday induction a voltage is created in the coil due to the oscillating \vec{B}_d of Eq. (2.20) that is observed through a spectrometer. Taking the \hat{B} axes as the axes of the coil, the signal S is proportional to $B_x \langle \hat{\mathbf{I}} \cdot \hat{x} \rangle$. But this will be proportional to the sum of the $\langle I_{x1} \rangle$ and $\langle I_{x2} \rangle$ components of the fictitious spin rotating with frequency ω_x :

$$S(t) = \langle I_x(t) \rangle \quad (2.65)$$

$$= 2[\langle \tilde{I}_{x1}^0 \rangle \cos \omega_x t + \langle \tilde{I}_{x2}^0 \rangle \sin \omega_x t] \cos \Psi. \quad (2.66)$$

The detector, however, only sees the combined signal

$$S(t) = M \cos(\omega_x t + \phi'), \quad (2.67)$$

where $M = \cos \Psi \sqrt{\langle \tilde{I}_{x1}^0 \rangle^2 + \langle \tilde{I}_{x2}^0 \rangle^2}$, with phase ϕ' resulting from the electronics. Using quadrature detection,[67] Eq. (2.67) is decomposed into “real” and “imaginary” components where

$$\text{real}(\phi') = M \cos \phi' \cos \omega_x t \quad (2.68)$$

$$\text{imaginary}(\phi') = M \sin \phi' \sin \omega_x t. \quad (2.69)$$

Recognizing that $\langle \tilde{I}_{x2}^0 \rangle = 0$ when $\Delta f = 0$, for most sequences, it is possible to find ϕ' and decompose the acquired signal into the predicted components.

A real NQR system will be composed of a very large number of nuclei. These nuclei will experience a distribution in their $V_{\alpha\alpha}$ due to inhomogeneity in the local EFG. This leads to a distribution in the resonance frequency about some center frequency, which is taken as ω_{NQR} . Additionally, for the common powder samples of NQR there will be a distribution in the angle of \hat{x} with respect to \hat{B} . By operating at $\Delta f = 0$, the signal S due to an individual nuclei will be given by Eq. (2.62)

$$S = A_0 \sin \theta'_0 \frac{\theta_0}{\theta'_0} \cos \Psi. \quad (2.70)$$

In the limit of delta function linewidths, where $\theta_0 = \theta'_0 = \gamma_I B t_0 \cos \Psi$, S is proportional to

$$S \propto \sin(\theta \cos \Psi) \cos \Psi, \quad (2.71)$$

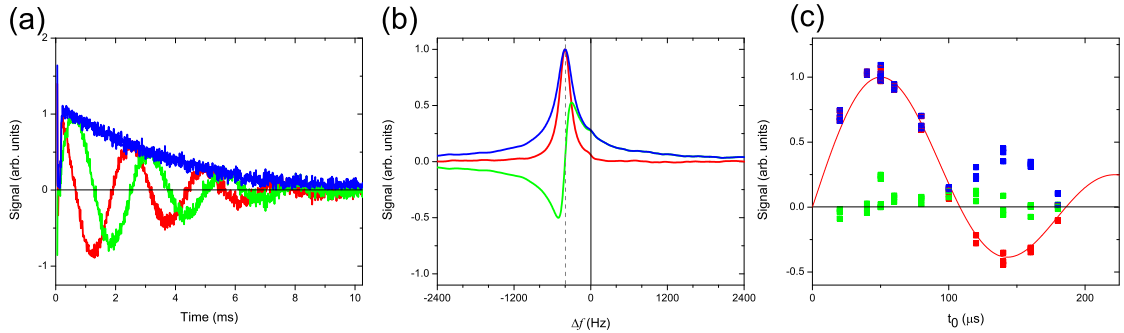


Figure 2.1: A representative FID signal (a), with the origin of time being the end of the rf pulse, decays primarily due to the distribution in ω_x among the various nuclei. A large voltage due to the pulse and acquisition artifacts dominate the first 0.2 ms of data, so those points are typically dropped before further analysis, as discussed in Appendix B. The magnitude of the observed signal S (blue) is processed as though it was acquired in a rotating frame, so the real (red) and imaginary (green) components oscillate due to the non-zero Δf . The Δf of the signal is found through the Fourier transform of the FID signal (b), which has its peak magnitude at $\Delta f = -402$ Hz. Defining the FID signal intensity as the peak of the signal in frequency space, a series of FIDs (c), taken at $\Delta f = 0$ using a consistent B and various lengths for t_0 , shows that the signal intensity follows the Bessel function of Eq. (2.72) (red line). Similarly the imaginary component stays close to zero, as expected for FID signals at $\Delta f = 0$. The negative values of the real signal are understood as the signal being 180° out of phase with the positive signal. Data is from a powder sample of p-chloroaniline, and performed at ω_x .

where $\theta = \gamma_I B t_0$. For a single crystal, the signal varies like a sine function, unless $\hat{B} \cdot \hat{x} = 0$ when no signal at all is observed. This is impossible for a powder, where the random orientation of \hat{x} with \hat{B} will ensure a finite θ for some fraction of nuclei. Integrating over the entire solid angle, the dependency of the powder's signal with respect to θ is given by a $3/2$ Bessel Function,[68] which has the features of a damped sinusoid, as shown in Fig. 2.1(c):

$$S_{pow} \propto \frac{\sin \theta - \theta \cos \theta}{\theta^2}. \quad (2.72)$$

This pattern in the signal behavior is useful for calibrating the system. As shown in Fig. 2.1(c) the Bessel function fits very well to the signals observed from various FIDs where θ has been altered by varying the pulse lengths. This can be used to determine the strength of B , or to measure γ_I , depending on the experimental unknowns. The calibration curves also allow for the definition of 90° or $\pi/2$ pulses. These are the smallest values of θ that produces a maximum signal, a definition true for both the powder and the single crystal. For an optimally aligned crystal, where $\Psi = 0$, this corresponds to a pulse that rotates \mathbf{I}_x from \hat{x}_3 to the x_1x_2 -plane, a rotation $\theta = 90^\circ$. For the more complex case of a powder, such an optimal pulse corresponds to $\theta = 119^\circ$, however it is still referred to as a 90° or $\pi/2$ pulse. Additionally, we can define 180° or π pulses as $\theta = 2 \cdot 119^\circ = 238^\circ$. For the 90-90 sequences, both the excitation and refocusing pulses will be $\theta = 119^\circ$ pulses; for the 90-180s, the excitation pulse will be a $\theta = 119^\circ$ pulse, with $\theta = 2 \cdot 119^\circ$ for the refocusing pulses.

In practice some time must elapse after the excitation pulse and before the signal acquisition, as shown in Fig. 2.1(a), since the pulse energy must be removed from the coil for the NQR signal to be detected. During this “dead time” the signal evolves, causing a phase shift which should be accounted for during the signal decomposition.

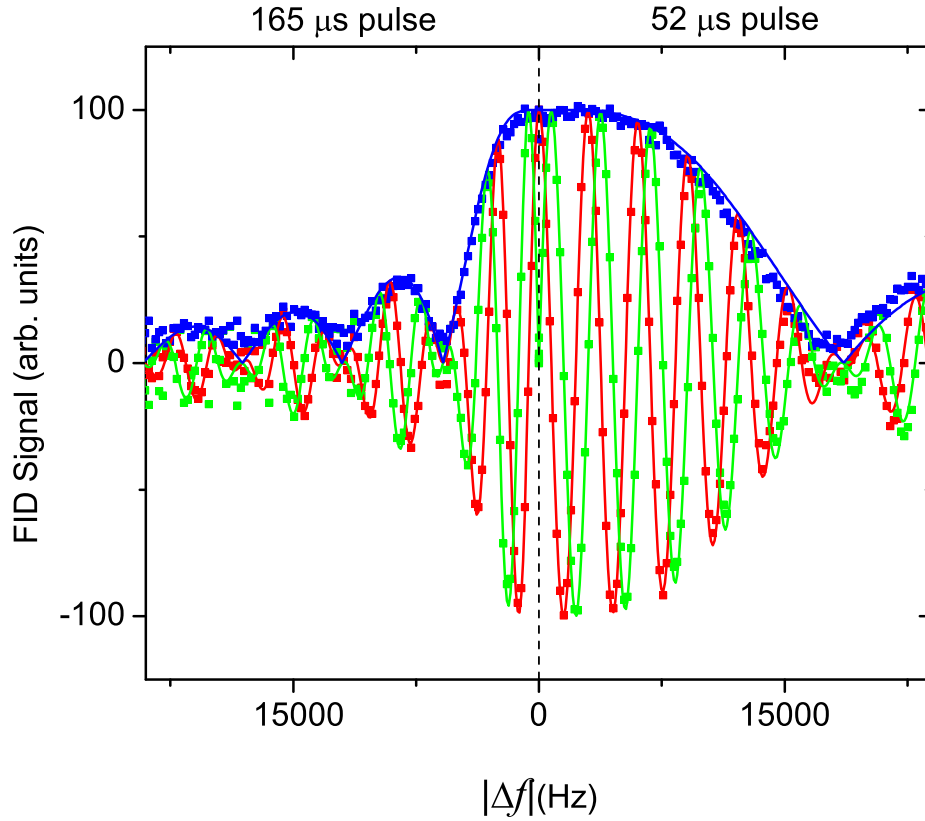


Figure 2.2: The predicted off-resonant signal (solid lines) calculated using Eqs. (2.62)-(2.63) are compared to the observed signals (dots) for $\theta = 90^\circ$ using excitation pulse lengths of 165 and 52 μs . The blue data corresponds to the magnitude of the signal, red to the real component $\langle \tilde{I}_{x1} \rangle$, and blue to the imaginary component $\langle \tilde{I}_{x2} \rangle$. The model agrees very well with the data, and confirms that longer pulses produce a weaker signal in general. Data is from the S1 powder sample of p-chloroaniline described in Chapter 6, and taken at ω_x with both halves normalized to the same value at $\Delta f = 0$. The dead time was 100 μs .

As shown in Fig. 2.2 by accounting for this phase adjustment the fictitious spin 1/2 model of the excitation captures the behavior of the signal due to Δf very well for a sample of p-chloroaniline, even though the model ignores the contributions to the NQR signal due to all other interactions.

2.5 Pulsed Spin Locking

The evolution due to a single pulse is well understood as a function of Δf , but this parameter alone will be insufficient to analyze the signal due to a SLSE. For the series of pulses in pulsed spin locking, the increased signal is due to some component of the signal being constant, or locked, over the series of echoes. The goal becomes finding that component. For certain cases, the evolution U due to the repeat unit, the $(\tau - \theta_{1x} - \tau)$ portion of the SLSE, can be expressed with the form $U = e^{i\theta_{tot}\mathbf{I}_x \cdot \hat{n}_{tot}}$ for a single repeat unit, or $U = e^{in\theta_{tot}\mathbf{I}_x \cdot \hat{n}_{tot}}$ for the n^{th} echo. With the signal properly phased, the expected signal for each echo will be a function of

$$\langle \tilde{I}_{x1}(2n\tau') \rangle = Tr[I_{x1}U\rho_b U^\dagger] \quad (2.73)$$

$$= Tr[e^{-in\theta_{tot}\mathbf{I}_x \cdot \hat{n}_{tot}}(\mathbf{I}_x \cdot \hat{x}_1)e^{in\theta_{tot}\mathbf{I}_x \cdot \hat{n}_{tot}}\rho_b], \quad (2.74)$$

where ρ_b is the density matrix immediately before the application of the repeat unit, and U^\dagger is the Hermitian conjugate of U . In order to focus on the evolution of $\mathbf{I}_x \cdot \hat{x}_1$, a new coordinate system $\hat{n}_1, \hat{n}_2, \hat{n}_3$, with corresponding operators $\mathbf{I}_x \cdot \hat{n}_i = I_{ni}$ is defined that is related to the original $\hat{x}_1, \hat{x}_2, \hat{x}_3$ system such that $\hat{n}_{tot} = \hat{n}_1$ and $\hat{x}_1 \cdot \hat{n}_3 = 0$. This set of operators allows the evolution of $\mathbf{I}_x \cdot \hat{x}_1$ to be expressed as

Table 2.1: The sums for the general values of θ are on the order of unity,[69] unless θ is small and no evolution takes place between echoes.

	Sum of N
cos $n\theta$ terms	$\sum_{n=1}^{n=N} \cos n\theta = \cos \frac{N\theta}{2} \sin \frac{N+1}{2}\theta \csc \frac{\theta}{2} - 1$
sin $n\theta$ terms	$\sum_{n=1}^{n=N} \sin n\theta = \sin \frac{N\theta}{2} \sin \frac{N+1}{2}\theta \csc \frac{\theta}{2}$

$$e^{-in\theta_{tot}\mathbf{I}_x \cdot \hat{n}_{tot}} [(\hat{x}_1 \cdot \hat{n}_{tot})I_{n1} + (\hat{x}_1 \cdot \hat{n}_2)I_{n2}] h.c., \quad (2.75)$$

which has the known solution, through Appendix A, of

$$(\hat{x}_1 \cdot \hat{n}_{tot})I_{n1} + (\hat{x}_1 \cdot \hat{n}_2)(I_{n2} \cos n\theta_{tot} + I_{n3} \sin n\theta_{tot}). \quad (2.76)$$

This shows that the I_{n1} term is unaltered by the evolution. Table 2.1 shows that sums of the remaining, orthogonal terms, I_{n2} , I_{n3} , over the N echoes will remain on the order of unity for all but the smallest θ_{tot} , i.e. when no evolution takes place: a physically unreasonable situation for our class of problems. Therefore, while the sum of the I_{n1} term grows as $(\hat{x}_1 \cdot \hat{n}_{tot})N$ the contribution from the orthogonal terms is insignificant, and we can ignore them from further analysis. While only the I_{n1} term is locked by a series of pulses, it should be expressed in terms of the original space:

$$I_{n1} = (\hat{x}_1 \cdot \hat{n}_{tot})I_{x1} + (\hat{x}_2 \cdot \hat{n}_{tot})I_{x2} + (\hat{x}_3 \cdot \hat{n}_{tot})I_{x3}. \quad (2.77)$$

Using Eq. (2.74), the locked signal is given by

$$\langle \tilde{I}_{x1}(2n\tau') \rangle = (\hat{x}_1 \cdot \hat{n}_{tot})^2 \langle I_{x1}^b \rangle + (\hat{x}_1 \cdot \hat{n}_{tot}) [(\hat{x}_2 \cdot \hat{n}_{tot}) \langle I_{x2}^b \rangle + (\hat{x}_3 \cdot \hat{n}_{tot}) \langle I_{x3}^b \rangle] \quad (2.78)$$

where $\langle I_{xi}^b \rangle = \text{Tr}[I_{xi}\rho_b]$ is the expectation value of I_{xi} before application of the repeat unit. As discussed in Chapters 4 and 6, \hat{n}_{tot} will not have a component along \hat{x}_2 , removing any $\langle I_{x2}^b \rangle$ contribution from the signal. Additionally, phase cycling will remove the contribution of $\langle I_{x3}^b \rangle$, as discussed in Chapter 4. As a result of these simplifications, the locked signal for each echo is given by what we call the projection model

$$\langle \tilde{I}_{x1}(2n\tau') \rangle = (\hat{x}_1 \cdot \hat{n}_{tot})^2 \langle I_{x1}^b \rangle, \quad (2.79)$$

due to its relationship between the projection of \hat{n}_{tot} along \hat{x}_1 . While this is true for SLSEs where one can determine $\theta_{tot}\hat{n}_{tot}$, finding such an expression is not always feasible. For example, the projection model was used to predict the signal response from the two SLSE sequences. As shown in Fig. 2.3, it did a very good job predicting the off-resonance response for a 90-90, but this was not true for a nearly identical 90-180 sequence. Implicit in the discussion of signal evolution so far is the idea that the evolution is governed solely by Δf . The failure of the projection model for the 90-180 shows that other behaviors must be accounted for in order to understand the SLSE signal behavior. These additional effects will become the focus of the remainder of this thesis.

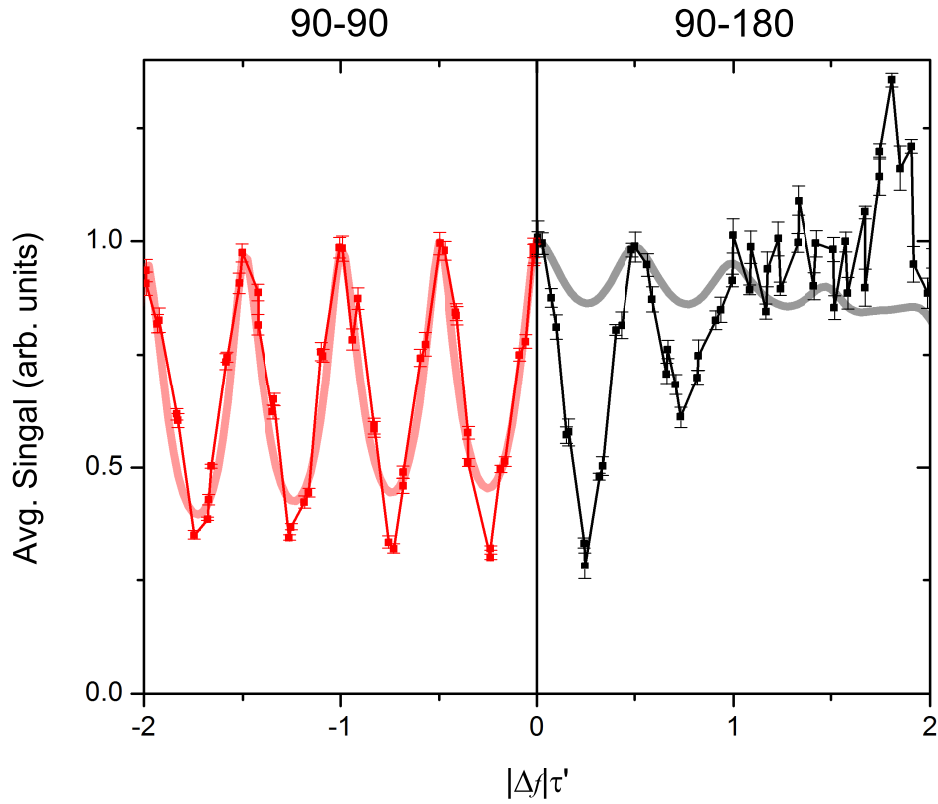


Figure 2.3: A projection model, Eq. (2.79) that only includes off-resonance effects (thick light lines) does a very good predicting the real signal behavior (dots and thin lines) of the 90-90 sequence on the left. However, for the 90-180 on the right, and for the weakest signals of the 90-90, this is not the case. Additional effects must be added to the evolution in order to account for the 90-180 response. Data is from the narrow sample of sodium nitrite described in Chapter 4, with $\tau' = 0.877$ ms and $t_p = 100$ μ s for both the 90-90 and 90-180. Data is averaged over 125 ms, and is symmetrical about $\Delta f = 0$.

Chapter 3: Experimental

3.1 Experimental Equipment

The experiments in this thesis, whether the sodium nitrite of Chapter 4 or the p-chloroaniline of Chapter 6, used mostly the same procedure and experimental equipment, such as shown in Fig. 3.1. The only exceptions are the imidazole experiments using a custom low power NQR system described in detail in Appendix D. The typical electronics, matched to 50 Ω s, used a Tecmag Apollo spectrometer to generate the rf pulses and analyze the NQR signal. The output of the Tecmag went into an AMT rf amplifier which could amplify the signal to powers of 1 kW. The output of the rf amplifier went through a set of crossed diodes before going into the probe circuitry. This was to ensure that only the high voltage of the rf pulses came into the probe circuitry from the amplifier.

The probe circuits for each compound were only slightly different, both being resonant circuits matched to 50 Ω s and tuned using variable capacitors. For reasons discussed in Chapter 5, the quality factor Q of the probe was kept low. As shown in

Table 3.1: The coil parameters for the experiments using sodium nitrite and p-chloroaniline. Both coils snugly held their respective sample containers.

	Sodium Nitrite	P-Chloroaniline
Coil length	10.5 cm	20.0 cm
Inner Coil diameter	4.1 cm	7.8 cm
Wire Diameter	2.2 mm	2.1 mm
Coil inductance	27 μ H	202 μ H
Typical operating Q	\sim 20	\sim 35

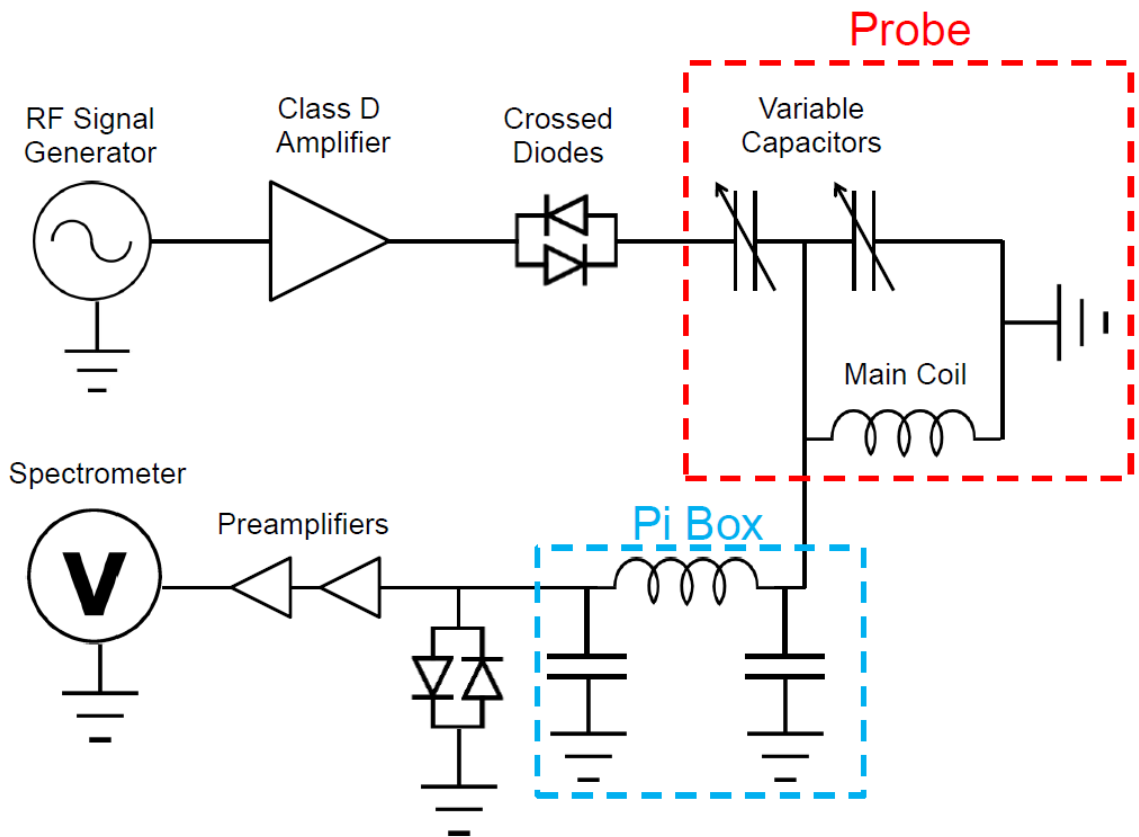


Figure 3.1: The circuit diagram generalized for the experiments described in this thesis. In addition to the resistive elements in the main coil, resistors were added in series to decrease the Q .

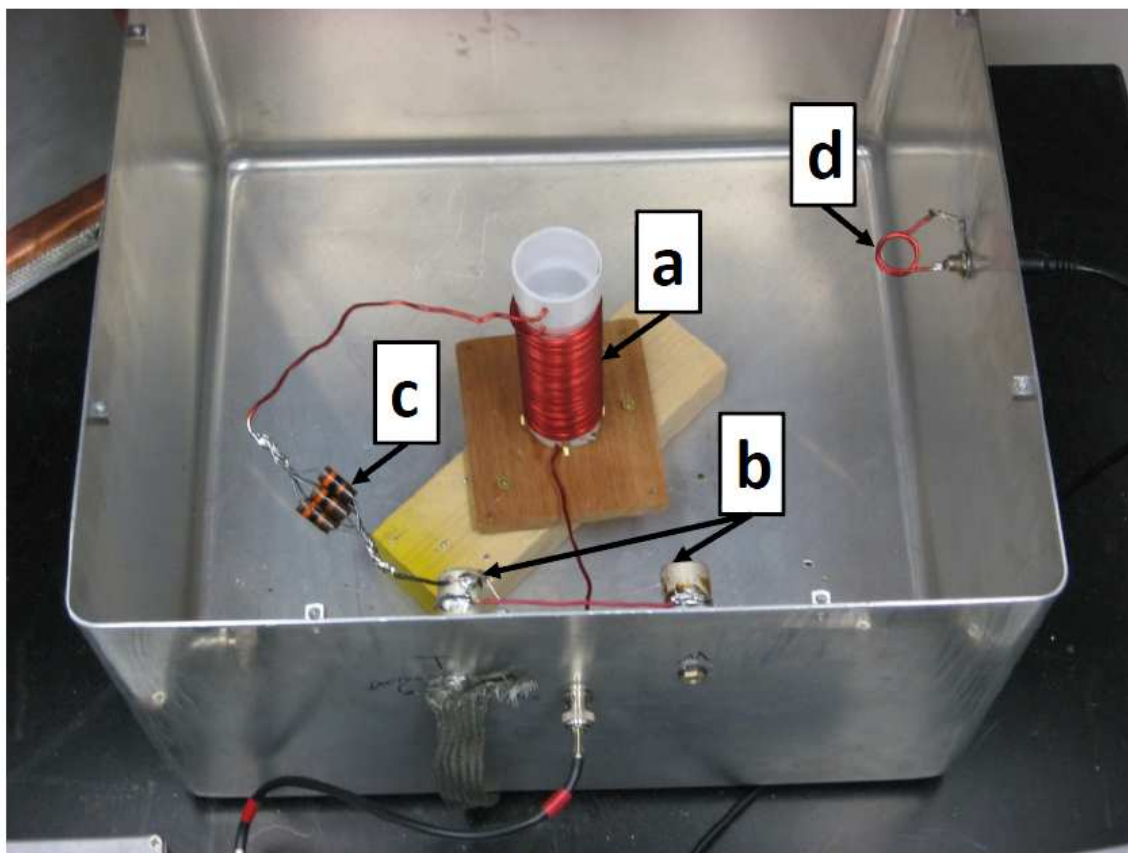


Figure 3.2: A picture of the actual configuration of the probe circuitry for sodium nitrite experiments shows the experimental simplicity possible with NQR. The main coil (a) is elevated with wooden boards to keep it from coupling to the metal box. The tuning capacitors (b) are accessible from outside the box. To lower the Q of the probe, $45\ \Omega$ have been added (c) in series with the main coil. The sniffer coil (d) is small and located some distance from the main coil to prevent interference.

Table 3.1 the configurations mainly differed in the size of the main coil which held the sample and detected the signal. An actual configuration for sodium nitrite is shown in Fig. 3.2. To remove external rf noise, the probes were kept in an aluminum box 40.5 cm long by 40.5 cm wide by 26 cm tall, with walls 1.8 mm thick, and the lid of the box screwed on during experiments. In addition to a signal line to the probe, and access to the tuning capacitors, another input on the box was left for a sniffer coil, a tool also discussed in Chapter 5 and Appendix D. The sniffer coil consisted of three 2 cm diameter loops of wire. Through Faraday induction, the magnetic field of the pulses in the main coil produced a proportional sniffer voltage. A switch triggered by the Tecmag's TTL line allowed the Tecmag to receive either the NQR signal, or the sniffer signal. This sniffer signal could easily saturate the Tecmag, and was typically reduced by 30 dB in order to produce a safe input for the Tecmag.

The output of the main coil then passed through a π -filter, to remove noise, and a set of crossed diodes. The diodes were grounded to prevent the large voltages from the rf pulses from overpowering the receiver circuitry. In particular the pair of pre-amplifiers were frequently damaged during experiments if the system was not configured properly and they were exposed to a high voltage. These had a nominal gain of 30 dB and were necessary to increase the signal to a value large enough for the Tecmag spectrometer. The Tecmag itself contained a built in pre-amplifier with the specific gain determined experimentally to ensure working in a linear region for the expected frequencies.

Tuning the system to a particular frequency was only a function of varying the resonance frequency of the probe circuit. One method to tune was with a function generator and a bidirectional coupler connected to the probe circuit. The function generator would generate a constant output voltage as it swept through a frequency range, and the bidirectional coupler could then sample the absorption spectrum of the

probe with the result displayed on an oscilloscope. The peak absorption frequency corresponded to the resonance frequency of the probe, and the width of the absorption spectrum was the only method used to determine Q . An easier, and more desirable way to set the resonance frequency was to adjust the tuning capacitors to maximize the output of the sniffer coil during an actual rf pulse of known frequency. This ensured that the entire system was tuned, instead of just the probe circuit. This was found to produce a noticeable difference in the speed of the tuning, since nothing needed to be disconnected.

As discussed in Chapter 2, there are advantages to using harder pulses with the largest possible B field. For the p-chloroaniline configuration in particular, the area and number of loops created a large voltage across the main coil. This would lead to arcing, which would reduce the pulse strength considerably. By running experiments with the roof of the box open and the lights off, it was possible to visually identify which areas were arcing. Resoldering the connections frequently helped reduce arcing, but the most useful solution was to simply wrap the arcing section of the probe in Teflon® tape. This made it possible to regularly operate at the maximum power of the power amplifier, and achieve harder pulses.

3.2 Experimental Procedure

The experiments consisted of performing pulse sequences on each sample at various off-resonances. A typical trial consisted of 8 – 80 scans, a single execution of the entire pulse sequence, at a given off-resonance in order to provide a useful SNR. In order to efficiently perform SLSE experiments at the correct Δf , it was necessary to know f_{NQR} as precisely as possible, preferably before taking the SLSE. One possible technique was to use the SLSE signal to determine Δf after the experiment, although

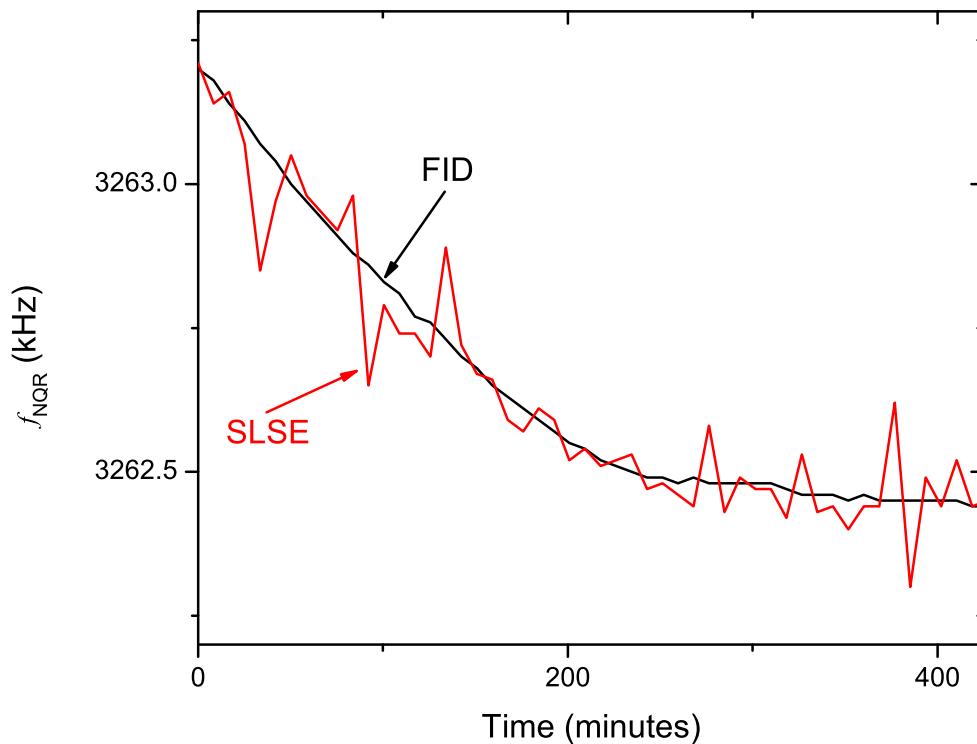


Figure 3.3: The NQR frequency found using the two FIDs (black line) compared to the NQR frequency determined by processing a SLSE signal (red line). Data for this comparison was taken from p-chloroaniline at ω_x . The SLSE data comes from a 90-90 sequence, with $\tau = 335 \mu\text{s}$ and $t_p = 55 \mu\text{s}$. Compared to the FID result, the SLSE data is not good enough to reliably determine the resonance frequency. Since the SLSEs were taken up to 5.5 kHz off resonance for this data, this is not surprising. But this shows how inaccurate the SLSE can be when determining Δf .

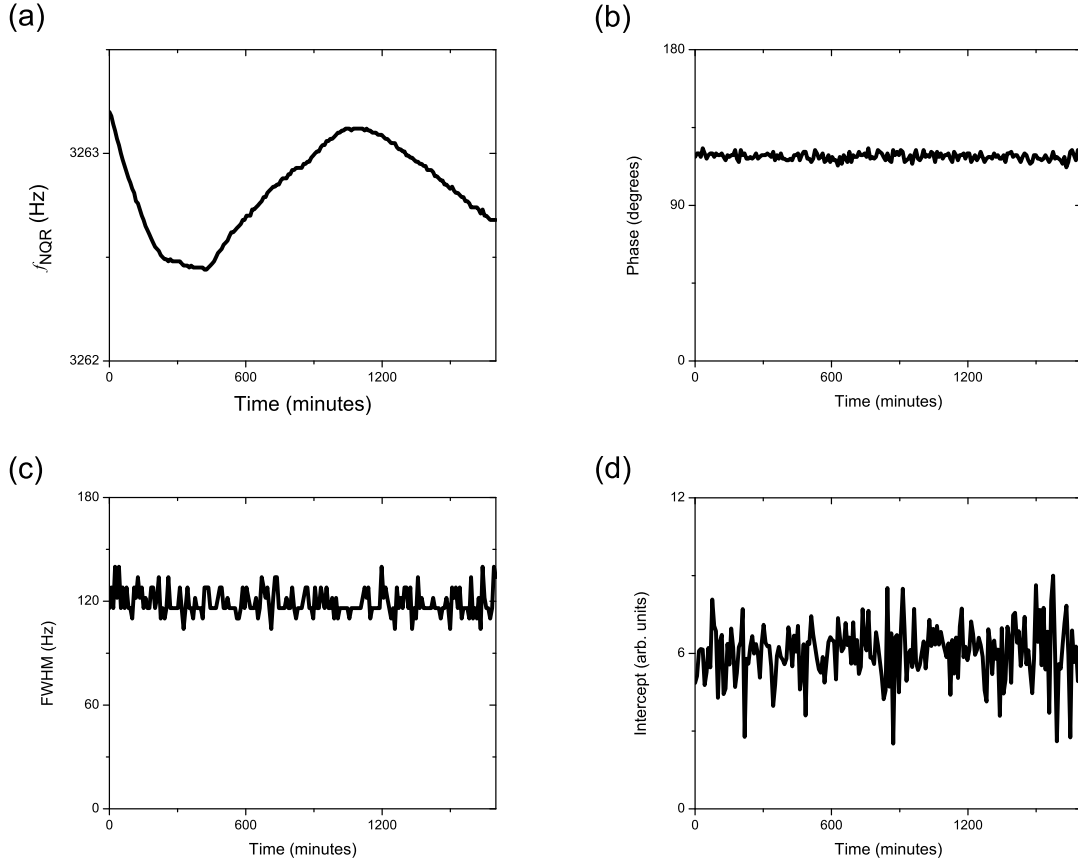


Figure 3.4: Plots of the data obtained from 204 resonant FIDs taken over 28 consecutive hours. (a) The daily cycle in f_{NQR} related to the daily temperature fluctuation in the lab is useful to show how much f_{NQR} can drift during signal acquisition. The peak df_{NQR}/dt observed in this run is ± 3 Hz per minute. Despite this variation in frequency there are still very consistent measurements of the FID's (b) phase and (c) FWHM. Additionally, while (d) shows a considerable scatter in the back projected intercept of the FID, which is used for normalization, the average is consistent over the 28 hours. The consistency of these results shows that no unexpected behavior occurs in the sample or the electronics over the course of the experiments. Data is from S1 of Chapter 6, and was taken at ω_x . The processing procedure for obtaining these values is given in Appendix B.

as shown in Fig. 3.3 this was not very accurate. Instead, f_{NQR} was determined using a series of FIDs. The first FID was taken with ω_{rf} at a value expected to be close to the NQR frequency. By determining the Δf of the first FID, a process described in Appendix B, a revised value for f_{NQR} was calculated. This was then used as ω_{rf} for what we call the “resonant FID.” The resonant FID’s signal was also processed to obtain Δf , further improving the estimate of f_{NQR} used for the SLSE experiments. The advantages of using the two FIDs were that it provided f_{NQR} with an accuracy of 12 Hz, and it provided a large amount of diagnostic information about the evolution of the system, such as shown in Fig. 3.4, since the resonant FIDs were saved. Unfortunately, this method is only possible for samples with a T_2^* long enough to produce a useable FID signal, and a T_1 short enough to make such data collection feasible. This was true for both sodium nitrite and p-chloroaniline, but such a procedure is not as practical for ammonium nitrate.[42]

In order to verify that the experimental system did not drastically change during the course of a typical set of experiments, the first and last trials would be performed at $\Delta f = 0$. This way, if the data for these trials disagreed significantly, it was an indicator that something may have gone wrong with the experiment, in addition to the information from the resonant FIDs. While establishing the experimental procedure described in this thesis, it was found that the SLSE sequences were heating the sample when the experiments were performed too rapidly. For the shortest values of τ , the sample could experience 162π pulses in 0.13 s for each scan. Since there could be dozens of scans, the relatively large average power in the probe would cause the linewidth to change. For sodium nitrite, the linewidth was observed to double when experiments were performed too rapidly. In order to control the linewidth behavior, a delay was introduced between each SLSE’s scan, which greatly increased the experimental time, but led to consistent linewidths between each trial. Typical

delays were on the order to 10 s, and after each trial the system was left alone for 5 minutes to cool. Unfortunately, the increased length of the trial meant that the resonance frequency would change somewhat while taking scans, adding to the error of the measurement. For p-chloroaniline the frequency could drift only as much as 30 Hz over the course of the typical six minute trial.

3.3 Automation

The Tecmag system has a Visual Basic Scripting Edition interface which allowed for the creation of scripts (VBS) to help automate the data acquisition. Large numbers of experiments were performed using a single VBS, an excerpt of which is given in Appendix E. For reasons described in Sec. 3.2, each trial began with a measurement of f_{NQR} , which began by taking a single FID near the expected resonance frequency. That spectrum was then saved to a temporary Tecmag .tnt file. The VBS then invoked a Java program that determined the off resonance of the temporary FID and saved the updated estimate for f_{NQR} to a text file. The VBS then read the text file, and updated the Tecmag rf frequency with that number. This involved process of interfacing Java and VBS was found to be faster and more reliable than using VBS alone to do the data processing. With the updated rf frequency, the resonant FID was then acquired, the resulting spectra saved to a permanent file, and the resonance frequency updated using the Java program. If too much drift was observed in the NQR frequency, the FID series was repeated until it was reasonable. With f_{NQR} known to within 12 Hz, it was then possible to perform the particular trial at the desired off-resonance. After each SLSE trial, the sample was left alone for five minutes to cool before the next trial was taken. With the automation, experiments could regularly be left alone for days while acquiring data.

This automation of the data collection made it possible to take a lot of granular data rapidly, and precisely. But such a large amount of data could not be realistically processed using the traditional point and click interface of the spectrometer software. In order to process the data efficiently, a large set of Java software was written called TecmagReader. This was itself based on two very useful free Java libraries. The first, Michael Thomas Flanagan's Java Scientific Library,[70] was used to perform the Fourier transforms and to fit the data. Sadly it is no longer publicly available. The second, JFreeChart,[71] was used to generate simple plots and helped to visualize the data. In addition to these libraries, TecmagReader could read the binary .tnt data files of the Tecmag system, and perform the standard data processing commands, such as removing baselines, truncation, phasing, and outputting the results into text files. The increased flexibility in data processing sped up the task by orders of magnitude. For instance the 204 spectra in Fig. 3.4 were processed in 4.4 s.

Naturally for Java, the software takes an object oriented approach to processing the data. The main class is the TNT class, which is built around the data available in the Tecmag .tnt file. However, the software does not require a .tnt file to be useful, in fact the data from the custom spectrometer described in Appendix D was easily incorporated. A TNT object contains the array of real and imaginary data, observation frequencies, dwell time, and other .tnt field parameters. Unfortunately, there was not enough time to extract the full pulse sequence parameters. While the TNT class is the root of the software, it is through the Set class, which is just an array of TNT files, that data processing is most often performed. The entire Java code used to extract the data from the .tnt file data is given in Appendix G. An excerpt from a sample Java program that uses the full TecmagReader suite is in Appendix F.

Chapter 4: Homonuclear Dipolar Coupling Revealed

4.1 Introduction

The theory introduced in Chapter 2 was suitable to explain the behavior of some NQR experiments, but not all. In this chapter, we demonstrate the significance of homonuclear dipolar coupling to the NQR signal under pulsed spin locking by modeling a system composed of just two coupled nuclei. The theoretical and experimental analysis is performed at the ω_y transition, with some exceptions, because the relative strength of the homonuclear contribution was the strongest at this frequency for our sample of choice. The theory, however, can easily be extended to the other transitions. Additionally, while the previous work was with the 2×2 matrices of the fictitious spin $1/2$, for this system it was found that a similar family of 4×4 matrices could describe the evolution. This chapter is based on work previously published in two papers.[72, 73]

As mentioned in Chapter 1, previous analyses of the NQR signal's decay during multipulse sequences focus on its exponential behavior.[7, 54, 55] However, we unexpectedly found that under certain off-resonant conditions the signal detected with a 90-180 SLSE sequence for a powder of spin-1 nuclei begins with a strong, fast, Gaussian decay. The conditions under which this decay appears, as well as its initial intensity, are well explained with the theoretical argument presented in Section 4.2. The decay is due to the homonuclear dipolar coupling not being rephased by the

refocusing pulses, while EFG inhomogeneity is rephased. This causes the envelope of the echo train to behave as though the signal decay was due entirely to the unrefocused dipolar coupling, an observation similar to that observed in NMR.[56–58] Therefore, the width of this Gaussian component in time is a measurement of the dipolar coupling of the sample.

To observe the homonuclear dipolar coupling in NMR requires pulses that give a nutation angle of $\theta = \pi$, or complicated excitation sequences to simulate the same. In NQR, however, the effective nutation angle of a pulse depends on the orientation of an individual crystallite with respect to the direction of the applied rf pulse, and is therefore not at all homogeneous across the powder sample. It is not surprising, therefore, that while the NMR experiments revealing homonuclear dipolar coupling are done with resonant pulses, the same resonant experiment in NQR does not reveal a similar result. However, we find for certain off-resonant pulses that the combined nutation angle of the pulse and off-resonance evolution does give an effective π pulse over the sample. These conditions allow a robust and direct measurement of homonuclear dipolar coupling in a powder sample at zero field, demonstrated in this chapter on a sample not expected to have any additional broadening mechanisms.

4.2 Theory

Building upon a previous framework,[11, 74] a theoretical derivation of the signal detected from spin-1 nuclei due to the time varying SLSE Hamiltonian is given by examining the evolution of the density matrix for a system composed of two such nuclei: spin- a and spin- b . For the two spin model there are nine permutations of the system's eigenstate $|ab\rangle$, shown in Fig. 4.1, where a is the quadrupole eigenstate of

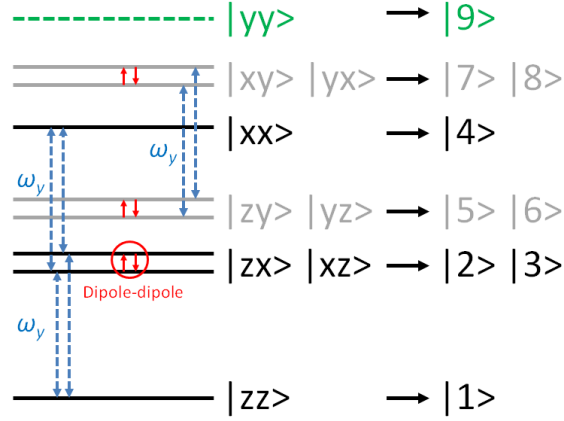


Figure 4.1: The eigenenergies are shown for spin- a and spin- b where $|x\rangle$, $|y\rangle$, $|z\rangle$ correspond to the eigenstates of the quadrupole Hamiltonian. The allowed transitions due to the rf Hamiltonian under the secular approximation in the interaction representation are given for $\omega_{rf} = \omega_y$. Similarly the transitions allowed by the dipolar coupling are highlighted by separating the degenerate states. No transitions between the sets of gray and black levels, the V and W -levels respectively, are possible under these assumptions. Additionally, no transitions involving the single green level are possible.

spin- a and likewise for b . The quadrupole Hamiltonian can be expressed as

$$\begin{aligned}
H_Q = & 2E_z|1\rangle\langle 1| + (E_z + E_x)(|2\rangle\langle 2| + |3\rangle\langle 3|) + 2E_x|4\rangle\langle 4| \\
& + (E_z + E_y)(|5\rangle\langle 5| + |6\rangle\langle 6|) + (E_x + E_y)(|7\rangle\langle 7| \\
& + |8\rangle\langle 8|) + 2E_y|9\rangle\langle 9|.
\end{aligned} \tag{4.1}$$

For simplicity, we assume the PAFs of the two spins are aligned with each other.

Perturbations from the homonuclear dipolar coupling H_I and rf Hamiltonians H_{rf} during the SLSE sequence will govern the transitions between levels. H_I is expressed as

$$H_I = \frac{\mu_0}{4\pi} \frac{\gamma_I^2 \hbar^2}{r^3} [\mathbf{I}_a \cdot \mathbf{I}_b - 3(\mathbf{I}_a \cdot \hat{r})(\mathbf{I}_b \cdot \hat{r})], \tag{4.2}$$

Table 4.1: The relationship between H_{rf} and H_Q suggests the definition of two fictitious spin-1/2 angular momentum operators, $\mathbf{I}^W = (I_1^W \hat{i}, I_2^W \hat{j}, I_3^W \hat{k})$ and $\mathbf{I}^V = (I_1^V \hat{i}, I_2^V \hat{j}, I_3^V \hat{k})$ which are expressed in terms of the Dirac matrices.[75] The superscripts indicate the set of levels the operator acts on, e.g.

$$I_1^W = \sum_{p=1}^4 \sum_{q=1}^4 [\rho_1(p, q) + \sigma_1(p, q)] |p\rangle \langle q|$$

$$I_1^V = \sum_{p=5}^8 \sum_{q=5}^8 [\rho_1(p-4, q-4) + \sigma_1(p-4, q-4)] |p\rangle \langle q|.$$

	I_1^i	I_2^i	I_3^i
$\mathbf{I}^W \equiv$	$(\rho_1 + \sigma_1)/2$	$(\rho_2 + \sigma_2)/2$	$(\rho_3 + \sigma_3)/2$
$\mathbf{I}^V \equiv$	$\rho_1/2$	$\rho_2/2$	$\rho_3/2$

where $\mathbf{r} = r\hat{r}$ is the displacement vector of the two nuclei, \mathbf{I}_a is the angular momentum operator for spin- a , and similarly for spin- b . H_{rf} is given by

$$H_{rf} = -\gamma_I \hbar [\hat{B} \cdot (\mathbf{I}_a + \mathbf{I}_b)] \cos(\omega_{rf} t - \phi), \quad (4.3)$$

where we assume ω_{rf} is close to ω_y for this derivation.

The time evolution of the density matrix is governed by the Liouville equation, Eq. (2.21), with the Hamiltonian for this system being

$$H = H_0 - \Delta H_Q + H_{rf} + H_I. \quad (4.4)$$

Note that the quadrupole Hamiltonian has again been split into two components

$$H_Q = H_0 - \Delta H_Q, \text{ with } H_0 \equiv \frac{\omega_{rf}}{\omega_y} H_Q, \Delta H_Q \equiv \frac{\Delta\omega}{\omega_y} H_Q.$$

Entering the interaction representation of H_0 , Eq. (2.21) becomes

$$\dot{\tilde{\rho}} = \frac{i}{\hbar} [\tilde{\rho}, -\Delta H_Q + \tilde{H}_{rf} + \tilde{H}_I]. \quad (4.5)$$

As shown in Fig. 4.1, transitions are only possible within two sets of four levels, the W and V -levels, under the secular approximation. Since the set of W -levels does not interact with the set of V -levels, only 4×4 matrices are needed to represent the action

of an operator on each set of levels. Working in the space $(\hat{i}, \hat{j}, \hat{k})$, Dirac matrices are used to rewrite H_{rf} and H_Q , shown in Table 4.1, because of their convenient commutation relationships. With this notation H_Q becomes

$$H_Q = \hbar\omega_y(I_3^W + I_3^V) + \frac{\epsilon_+}{2}(4|9\rangle\langle 9| + \mathbf{1}^W + \mathbf{1}^V), \quad (4.6)$$

with a similar expression for $\Delta\tilde{H}_Q = \Delta H_Q$. Recognizing $I_y = I_y^a + I_y^b = 2(I_2^V + I_2^W)$, it can be shown under the secular approximation that \tilde{H}_{rf} is time independent:[74]

$$\tilde{H}_{rf} = -\gamma_I \hbar B \cos \Psi (\cos \phi [I_2^W + I_2^V] + \sin \phi [I_1^W + I_1^V]), \quad (4.7)$$

where $\cos \Psi = \hat{B} \cdot \hat{y}$ for this transition.

\tilde{H}_I under the secular approximation can be expressed as

$$\begin{aligned} \tilde{H}_I \approx & \alpha_y (|2\rangle\langle 3| + |3\rangle\langle 2|) + \alpha_x (|5\rangle\langle 6| + |6\rangle\langle 5|) \\ & + \alpha_z (|7\rangle\langle 8| + |8\rangle\langle 7|), \end{aligned} \quad (4.8)$$

with the coefficients given as $\alpha_y = \frac{\mu_0 \gamma_I^2 \hbar^2}{4\pi r^3} [1 - 3(\hat{y} \cdot \hat{r})^2]$, and similarly for α_x, α_z .

While \tilde{H}_I can also be written in terms of Dirac matrices it is not illuminating to the discussion. In its present form, however, it is easy to see both the flip-flop terms that drive the interaction and that \tilde{H}_I commutes with H_Q and ΔH_Q .

The SLSE excitation pulse is assumed for simplicity here to be a delta function pulse. During the delays of duration τ between pulses, \tilde{H} consists of just \tilde{H}_I and ΔH_Q . During a pulse it is assumed that \tilde{H}_{rf} is so much greater than \tilde{H}_I that the dipolar coupling's contribution can be dropped and $\tilde{H} \approx \tilde{H}_{rf} - \Delta H_Q$. As confirmation of the validity of this approximation for our experiments, we also numerically solved

for the evolution of the signal incorporating the dipolar coupling during the pulse and found that the two results were indistinguishable within computational error. Recognizing that \tilde{H}_{rf} and \tilde{H}_I are independent of time under the secular approximation, the evolution of $\tilde{\rho}$, after N refocusing pulses of length t_p , is

$$\tilde{\rho}(2N\tau') = (DPD)^N \rho(t = 0^+) (DPD)^{\dagger N}. \quad (4.9)$$

Here we distinguish evolution due to the dipolar coupling

$$D \equiv e^{-\frac{i}{\hbar} \tilde{H}_I \tau}, \quad (4.10)$$

from evolution due to the pulse and the free evolution

$$P \equiv e^{\frac{i}{\hbar} \Delta H_Q \tau} e^{-\frac{i}{\hbar} (\tilde{H}_{rf} - \Delta H_Q) t_p} e^{\frac{i}{\hbar} \Delta H_Q \tau}, \quad (4.11)$$

and define $\rho(t = 0^+)$ as the density matrix after the excitation pulse.

The initial density matrix is found using the equipartition theorem in the high temperature limit: $\rho_0 = \frac{1}{9}(\mathbf{1}^W + \mathbf{1}^V + |9\rangle\langle 9| - \frac{H_Q}{kT})$. The behavior of the magnetic moments in the lab frame produces the signal, given by

$$\langle I_y \rangle = Tr[\rho I_y] = Tr[\tilde{\rho} \tilde{I}_y], \text{ with} \quad (4.12)$$

$$\tilde{I}_y = 2(I_2^V + I_2^W) \cos \omega_{rf} t + 2(I_1^V + I_1^W) \sin \omega_{rf} t. \quad (4.13)$$

Since the identity matrices and the $|9\rangle\langle 9|$ term commute with P and D , and since their trace with $\mathbf{1}^V$ and $\mathbf{1}^W$ is zero, those terms can be ignored in ρ_0 . By a similar argument, they can also be dropped from ΔH_Q . This allows ρ_0 to be reduced to

$$\varrho_0 = -\frac{\hbar\omega_y}{9kT}(I_3^W + I_3^V). \quad (4.14)$$

After the initial pulse of duration t_0 and phase ϕ_0 , the density matrix becomes[74]

$$\varrho(t = 0^+) = \frac{\hbar\omega_y}{9kT} \sin \theta'_0 (\mathbf{I}^W + \mathbf{I}^V) \cdot \hat{i}, \quad (4.15)$$

The components of \mathbf{I}^W and \mathbf{I}^V in the \hat{k} direction are dropped from $\varrho(t = 0^+)$ through phase cycling. This is performed by subtracting subsequent experiments with $\phi_0 = 0$ and $\phi_0 = \pi$ to eliminate any signals that might arise from either the \hat{k} component or probe ringing due to the refocusing pulses.

While Eqs. (4.9) and (4.14) give the complete solution to the evolution of the signal, it is instructive to look for symmetries in the solution, particularly with regard to the frequency and strength of the refocusing pulse. We therefore turn to examining the operator P of Eq. (4.11) more closely and note that the relevant operators within it consist exclusively of the operators given in Table 4.1. This allows P to be treated as the sum of three rotations, where the first and the third rotation are determined by off-resonance alone, and the second rotation by the effects of the refocusing pulse and the off-resonance condition. We can write the three rotations as: $\theta_a \hat{n}_a = \theta_c \hat{n}_c = 2\pi \Delta f \tau \hat{k}$ for the delays of duration τ ; and $\theta_b \hat{n}_b = \theta_1 \hat{i} + \theta_a \frac{t_p}{\tau} \hat{k}$ during the pulse. For a given crystallite orientation the net rotation $\theta_{tot} \hat{n}_{tot}$ is the same for both the W and V -levels and can be found using quaternions.[76] P becomes

$$P = e^{i\theta_{tot} \mathbf{I}^W \cdot \hat{n}_{tot}} e^{i\theta_{tot} \mathbf{I}^V \cdot \hat{n}_{tot}}, \quad (4.16)$$

where

$$\cos \frac{\theta_{tot}}{2} = \cos \theta_a \cos \frac{\theta_b}{2} - \sin \theta_a \sin \frac{\theta_b}{2} \hat{n}_a \cdot \hat{n}_b, \text{ and} \quad (4.17)$$

$$\begin{aligned} \sin \frac{\theta_{tot}}{2} \hat{n}_{tot} &= \sin \frac{\theta_b}{2} \hat{n}_b + \sin \theta_a \cos \frac{\theta_b}{2} \hat{n}_a \\ &+ (\cos \theta_a - 1) \sin \frac{\theta_b}{2} \hat{n}_a (\hat{n}_a \cdot \hat{n}_b). \end{aligned} \quad (4.18)$$

The operator P is clearly periodic in θ_a and $\frac{\theta_b}{2}$, so the signal will be periodic in these as well. In the limit of delta function pulses, where $\hat{n}_a \cdot \hat{n}_b = 0$ and $\hat{n}_b = \hat{i}$, θ_{tot} is insensitive to the sign of the off-resonance, while the \hat{k} component of \hat{n}_{tot} flips sign. Due to both the phase cycling of the pulse sequence and the idealized pulse shape, this flip will not impact the signal, which will be symmetrical as a function of off-resonance. In the same delta function limit, an increase in θ_a by π should produce the same signal, so the signal repeats off resonance with a period of $\frac{1}{2\tau}$, which is a periodicity seen for various sequences.[54, 55, 74, 77] Within this periodicity we observe extremes in the signal behavior at $\Delta f = \frac{m}{2\tau}$, for integer m , corresponding to $\theta_{tot} \hat{n}_{tot} = \theta_b \hat{i}$; and at $\Delta f = \frac{1}{4\tau} + \frac{m}{2\tau}$, corresponding to $\theta_{tot} \hat{n}_{tot} = \pi(\sin \frac{\theta_b}{2} \hat{i} + \cos \frac{\theta_b}{2} \hat{k})$. Note that if $\theta_b = \pi$ then $\hat{n}_{tot} = \hat{i}$ regardless of Δf . This means $\tilde{\varrho}$, starting from Eq. (4.15), is essentially locked along \hat{i} , making the evolution due to EFG inhomogeneity refocus under this condition. However, for $\theta_b = \frac{\pi}{2}$, $\theta_{tot} \hat{n}_{tot}$ varies from $\frac{\pi}{2} \hat{i}$ for $\Delta f = \frac{m}{2\tau}$ to $\pi(\frac{\hat{i}}{\sqrt{2}} + \frac{\hat{k}}{\sqrt{2}})$ for $\Delta f = \frac{1}{4\tau} + \frac{m}{2\tau}$. The latter results in $\tilde{\varrho}$ experiencing anti-resonant kicking as it alternates between the ij -plane and the k -axis between echoes. This can produce a rapidly oscillating initial signal, like that shown in Fig. 4.2, since $Tr[I_3^{W,V} I_{1,2}^{W,V}] = 0$.

The evolution of the signal under D and P for a given net rotation is performed numerically, but under certain conditions, namely $\hat{n}_{tot} = \hat{i}$, an analytical solution is

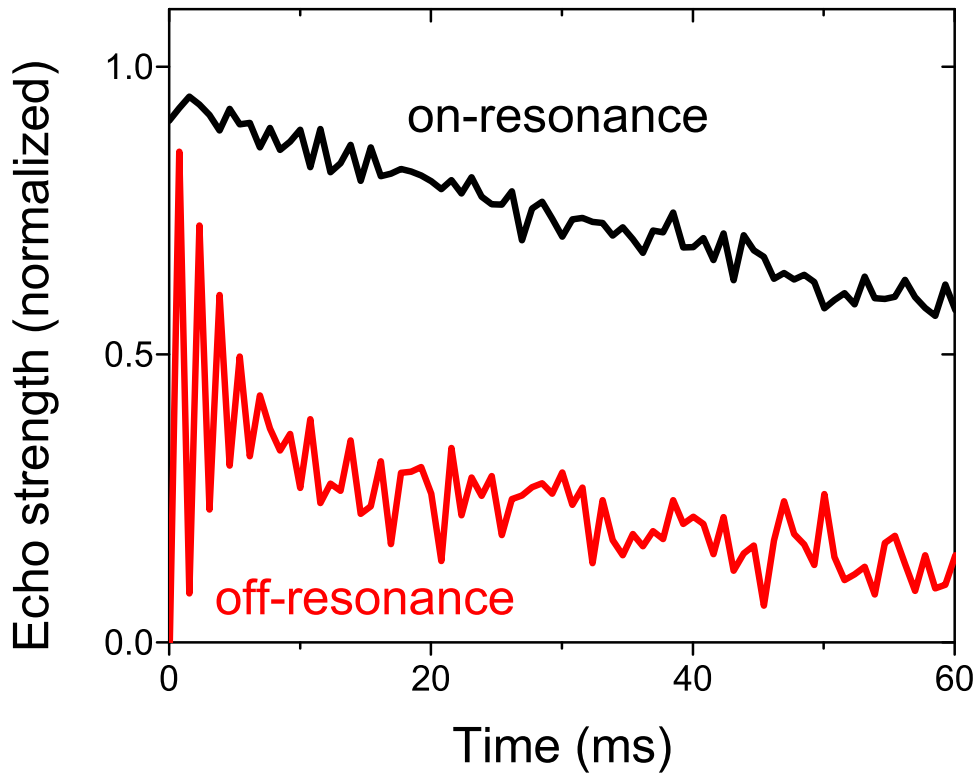


Figure 4.2: The signal from a 90-90 SLSE sequence is shown for both on-resonance ($\Delta f = 0$) and off-resonance ($\Delta f = 1/[4\tau']$) conditions. The heavy oscillations in the off-resonance signal are due to the large \hat{k} component of \hat{n}_{tot} causing the magnetization to oscillate between the ij -plane and the k -axis. Data was taken at ω_y with $\tau = 335 \mu\text{s}$ and $t_p = 100 \mu\text{s}$ with the narrow sample described in Section 4.3. Data here, and elsewhere, has been normalized to the amplitude of the $\Delta f = 0$ signal at $t = 0$.

readily available.[11] We briefly review this solution here and characterize the average echo response for a large number of echoes.

The signal for the n^{th} echo, detected by the same coil that provided the excitation pulses, is given by

$$\begin{aligned} \langle \mathbf{I} \rangle \cdot \hat{B} &= \hat{y} \cdot \hat{B} \langle I_y \rangle \\ &= \frac{2\hbar\omega_y}{3kT} \cos\psi \sin\omega_{rf}t \sin\theta_0 \left[\frac{2}{3}g^W + \frac{1}{3}g^V \right], \text{ where} \end{aligned} \quad (4.19)$$

$$g^i = 1 - 2F^i \sin^2 nx^i, \quad (4.20)$$

$x^i = \cos^{-1}[\cos\theta^i \cos d^i]$, $F^i = \frac{\cos^2\theta^i \sin^2 d^i}{1 - \cos^2\theta^i \cos^2 d^i}$, and θ^i , for the W and V -levels, is $\theta^W = \theta_{tot}$ and $\theta^V = \frac{\theta_{tot}}{2}$. Likewise d^i , the angle of the rotation due to dipolar coupling evolution, varies between the W and V -levels: $d^W = \alpha_y\tau$ and $d^V = (\alpha_z - \alpha_x)\tau$. Focusing on the W -levels that provide $\frac{2}{3}$ rds of the signal, we drop the superscripts. Using the standard sum for $\sin^2 nx$, [69] the average signal over a number of echoes N is proportional to the average value of g ,

$$\bar{g} = 1 - \left(1 - \frac{\cos[(N+1)x] \sin Nx}{N \sin x} \right) F, \quad (4.21)$$

which reduces to

$$\bar{g} \approx 1 - F, \quad (4.22)$$

for large N and $d \ll 1$. The restriction on the size of d follows from the need to keep τ small enough for the signal to be well refocused. For $\theta_{tot} = m\pi$, $F = 1$ and the average signal will disappear. However, for $\theta_{tot} = (2m+1)\frac{\pi}{2}$ the average signal will go to a

maximum as $\bar{g} = 1$. This corresponds to the full refocusing of the dipolar coupling evolution. We note that for the V -levels the signal will disappear for $\theta_{tot} = 2m\pi$, and go to a maximum for $\theta_{tot} = (2m + 1)\pi$. Therefore, for $\theta_{tot} = \pi$ the signal from the V -levels will be refocused, while the signal from the W -levels will decay.

The sensitivity of the loss of signal to $\theta_{tot} = \pi$ is found by expanding θ_{tot} as $\pi + \Delta\theta$, where $\Delta\theta$ is considered a perturbation. This allows F to be approximated as

$$F \approx \frac{d^2}{\Delta\theta^2 + d^2}, \quad (4.23)$$

which provides a simple relationship relating the expected size of the signal due to the dipolar coupling decay to $\Delta\theta$ and the size of d :

$$\Delta\theta^2 = \left(\frac{\bar{g}}{1 - \bar{g}}\right)d^2. \quad (4.24)$$

This says that for the signal to be half the maximum, $\Delta\theta$ and d should be equal.

We conclude that the dipolar coupling decay in the W -levels should be clearly observable in $\frac{2}{3}$ rds of the signal when

$$\theta_{tot} = \pi \pm d \text{ and } \hat{n}_{tot} = \hat{i}. \quad (4.25)$$

These requirements define the 180° condition. While this is impossible to achieve for all crystallites in the powder, under certain conditions, namely $\Delta f = \frac{1}{4\tau} \pm \frac{m}{2\tau}$, the constraint on θ_{tot} can be met. We previously found for this off-resonant condition with delta-function pulses that $\theta_{tot}\hat{n}_{tot} = \pi(\sin\frac{\theta_b}{2}\hat{i} + \cos\frac{\theta_b}{2}\hat{k})$. Therefore the net rotation will be π for the entire powder sample. The direction of \hat{n}_{tot} can be brought close to \hat{i}

by choosing the pulse strength such that a large portion of the signal producing spins experiences a θ_b close to π . This corresponds to $\theta = 2 \cdot 119^\circ$. Under these conditions we can expect to see a large decay. For those crystallites experiencing $\theta_b \neq \pi$, so that $\hat{n}_{tot} \neq \hat{i}$, the effect is to reduce the decay rate by $\sin^2(\frac{\theta_b}{2})$ as determined by numerical simulations. This effect is understood by looking at $\theta_b = \frac{\pi}{2}$ where the signal is only apparent every other echo because of the anti-resonant kicking, as demonstrated in Fig. 4.2. Since there is no evolution of the signal absent an echo, the decay rate is decreased by a factor of 1/2. Looking at a powder, the apparent decay rate is predicted to be 86% of the value for the single crystal result.

For nuclei a the contribution to the second moment of its NQR signal due to each neighbor b comes from Vega,[9]

$$\langle \Delta\omega^2 \rangle = \sum_b \frac{1}{3} \frac{(d_{ab}^V)^2}{\tau^2} + \frac{2}{3} \frac{(d_{ab}^W)^2}{\tau^2}. \quad (4.26)$$

Since our sequence will refocus the signal from the V -levels, the observed decay in time is determined by the contribution of the W -levels to the second moment:

$$\langle \Delta\omega^2 \rangle_W = \sum_b \frac{2}{3} \frac{(d_{ab}^W)^2}{\tau^2}, \text{ where} \quad (4.27)$$

$$\sum_b \frac{(d_{ab}^W)^2}{\tau^2} = \sum_b \alpha_{y_{ab}}^2 \equiv \alpha_{y_{eff}}^2. \quad (4.28)$$

The last line defines an effective dipolar coupling frequency $\alpha_{y_{eff}}$ that takes into account the multi-spin nature of the system.

Using calculations performed by Sauer and Klug for sodium nitrite,[74] the predicted width of the Gaussian component of the echo train T_d follows, with the results

Table 4.2: The predicted value of $\Delta\omega$, from Eq. (4.27), and also $T_d = \frac{1}{\sqrt{\langle\Delta\omega^2\rangle_W}}$ for both a single crystal and a powder under a 90-180 sequence. In calculating the second moment, all nitrogen within a sphere with a radius four times the largest length of the unit cell were considered.[74]

f_{NQR} (MHz)	$\frac{\sqrt{\langle\Delta\omega^2\rangle_W}}{2\pi}$ (Hz)	Predicted values of T_d (ms)	
		Single crystal	Powder
$\frac{\omega_x}{2\pi} = 4.64$	21	7.5	8.7
$\frac{\omega_y}{2\pi} = 3.60$	35	4.5	5.2
$\frac{\omega_z}{2\pi} = 1.04$	21	7.5	8.7

shown in Table 4.2 for both a single crystal and a powder.

4.3 Experimental procedure

Using the procedure of Chapter 3, experiments were performed on two powder samples of sodium nitrite NaNO_2 encased in wax to reduce piezoelectric effects: a 32 g sample (97.1% purity) manufactured by Fisher Scientific in 1979, and a 27 g sample (99.5% purity, super free-flowing), manufactured by Sigma-Aldrich in 2005. Despite having a lower purity, the quarter century older sample had a narrower linewidth, measured with an FID, due to a smaller EFG inhomogeneity. This was because of the considerably larger crystallites of the sample, as was demonstrated by grinding the narrow sample with a mortar and pestle and finding the linewidth was now comparable to the broader linewidth of the Sigma-Aldrich sample. We therefore call the Fisher Scientific sample the “narrow sample” and the Sigma Aldrich sample the “broad sample”, with their linewidths given in Table 4.3. This variation in linewidth due to crystallite size explains, at least in part, the variation in linewidths reported in the literature for sodium nitrite at room temperature.[78–81] Another group has demonstrated a similar dependency of NQR linewidth on crystal size for other substances.[60]

Both 90-90 SLSEs and 90-180 SLSEs were compared. Both the excitation and

Table 4.3: The observed full width at half maximum (FWHM) linewidths for both samples at the three NQR transition frequencies show that the broad sample has a larger linewidth for all three frequencies. The EFG component is found by decomposing the linewidth’s Voigt profile into the predicted Gaussian (dipolar coupling) and Lorentzian (EFG) components. Measurements for all linewidths are accurate to within 20 Hz.

f_{NQR}	Narrow sample		Broad sample	
	Total width (Hz)	EFG (Hz)	Total width (Hz)	EFG (Hz)
ω_x	185	125	390	361
ω_y	154	97	309	280
ω_z	143	67	215	163

refocusing pulses for all 90-90 sequences used pulse lengths of 100 μs , with the same rf-amplitude. For the 90-180 sequences a fixed rf-amplitude was used for each pulse, but the refocusing pulse was twice as long as the excitation pulse. For ω_x and ω_y the excitation pulse was 50 μs long, while the ω_z experiments used 100 μs pulses due to limitations in the amplifier that required weaker pulses at the lower frequency. For delta function pulses, the signal’s off-resonance behavior is predicted to have a period of $\frac{1}{2\tau}$, as discussed above. For finite pulses, we observe experimentally that this periodicity is close to $1/(2\tau')$, particularly for the 90-90 sequences. For this reason, our experimental graphs where the rf frequency is varied are expressed in terms of $\Delta f \cdot \tau'$. For the ω_x and ω_y transitions, data was taken between $\pm 2/\tau'$. Due to the low SNR and electronics limitations, data for ω_z was only taken on-resonance and at $\Delta f = \pm \frac{1}{4\tau'}$.

4.4 Experimentally achieving the 180° condition for finite pulses

The acquired SLSE data was processed as described in Appendix C to provide an average echo, and an echo train. All observed echo trains were fit to the function

$$S(t) = A \left(p_g \exp \left[-\frac{1}{2} \left(\frac{t}{T_d} \frac{\tau}{\tau'} \right)^2 \right] + [1 - p_g] \exp \left[-\frac{t}{T_{2e}} \right] \right), \quad (4.29)$$

where A is amplitude at $t = 0$, T_{2e} is the long term decay constant, p_g is the percent of the signal due to the Gaussian decay, and T_d is the width of the Gaussian decay associated with the strength of the dipolar coupling. The addition of the $\frac{\tau}{\tau'}$ term to the Gaussian component is because there is no evolution due to the dipolar coupling during the finite pulse lengths.

The experimental conditions, with finite pulses, that lead to a strong Gaussian component were found using Eq. (4.17) and the limit $\theta_{tot} = \pi \pm d$ of the 180° condition. This led to the constraint that

$$\left| \cos \theta_a \cos \frac{\theta_b}{2} - \sin \theta_a \sin \frac{\theta_b}{2} \hat{n}_b \cdot \hat{k} \right| \leq \frac{d}{2}. \quad (4.30)$$

This equation must be satisfied for a large portion of the sample in order to see the rapid decay in the signal due to the dipolar coupling. But θ_a , θ_b , and $\hat{n}_b \cdot \hat{k} = \frac{\theta_a}{\theta_b} \frac{t_p}{\tau}$ all vary among nuclei due to the EFG inhomogeneity, while θ_b and $\hat{n}_b \cdot \hat{k}$ also vary with the random alignment of the rf with respect to the crystallite's orientation. In order to satisfy the inequality, it is necessary to keep both the cosine ($\cos \theta_a \cos \frac{\theta_b}{2}$) and sine ($\sin \theta_a \sin \frac{\theta_b}{2} \hat{n}_b \cdot \hat{k}$) terms small. The conditions which make this possible for a large portion of the sample determine the pulse and sample characteristics necessary to observe the decay due to dipolar coupling.

The sine term is small for all crystallites when

$$|\hat{n}_b \cdot \hat{k}| \leq \frac{d}{2}, \quad (4.31)$$

which is easily met when the value of $\frac{t_p}{\tau} \ll 1$. The cosine term is small for all crystallites when $|\cos \theta_a| \leq \frac{d}{2}$. If Δf represents the average off-resonance then $\theta_a = 2\pi(\Delta f + \delta f_{EFG})\tau$, where δf_{EFG} is a nuclei's additional off-resonance due to EFG inhomogeneity. The cosine inequality is fully satisfied when $\Delta f = \frac{1}{4\tau} + \frac{m}{2\tau}$ and $2\pi\delta f_{EFG} \leq \frac{\alpha_{y_{eff}}}{2}$. This shows that the 180° condition is met for a majority of the sample when the linewidth broadening due to EFG inhomogeneity is less than or equal to that due to W -level dipolar coupling. This condition is unnecessarily strict for pulse strengths where $\theta_b \approx \pi$, corresponding to a 90-180 sequence, as will be shown experimentally with a sample where the linewidth broadening is clearly dominated by EFG inhomogeneity.

In addition to the requirement that θ_{tot} be close to π , the direction of the net rotation must be close to \hat{i} in order to both avoid heavy oscillations and to accurately measure the dipolar coupling. Examining Eq. (4.18) under the assumption $\theta_{tot} = \pi$ reveals that $\hat{n}_{tot} \approx \hat{i}$ when $\theta_b \approx \pi$ and $\hat{n}_b \approx \hat{i}$. The latter condition can only be met when the rotation due to off-resonance during the pulse is kept small. This requires $\Delta f = \pm \frac{1}{4\tau'}$, when τ' is small, but allows $\Delta f = \frac{1}{4\tau'} + \frac{m}{2\tau'}$ as τ' increases. Together these constraints define the experimental conditions under which the strongest decay due to the dipolar coupling should appear: a 90-180 sequence and $\Delta f = \pm \frac{1}{4\tau'}$. In addition to the frequency and strength of the pulse, the timing of the pulses must be chosen with respect to the duration in time of the pulses. Since the finite pulse lengths can inhibit the decay, the minimum τ to operate at is derived from the requirement that

$|\hat{n}_b \cdot \hat{k}| \leq \frac{d}{2}$. This leads to the relation $\tau_{min}^2 \geq \frac{|\theta_a|}{\theta_b} \frac{2t_p}{\alpha_{y_{eff}}} \approx \frac{t_p}{\alpha_{y_{eff}}}$, for the 90-180, which is in good agreement with the experimental results shown in Section 4.5.

4.5 Experimental Results

Examples of theoretical and actual signal behavior for various experimental parameters are shown in Fig. 4.3 for the narrow sample at frequencies close to ω_y . Since the model does not include the long term T_{2e} effects, its accuracy is limited in the long term behavior for both sequences. For this reason we compare the initial signal to theoretical calculations which have been scaled to match the data. However, the rapidly alternating initial signal near $\Delta f = \frac{1}{4\tau'} + \frac{m}{2\tau'}$ for the 90-90s due to the anti-resonant kicking is captured by the model. Additionally the conditions where dipolar coupling is not refocused for a large portion of the sample are seen in the undulating signal of the 90-180s near the $\Delta f = \frac{1}{4\tau'} + \frac{m}{2\tau'}$ locations. The period of the undulations depends on the second moment in Table 4.2, and is given as $\frac{2\pi}{\alpha_{y_{eff}}} \frac{\tau'}{\tau}$. For small τ these undulations are weak as the finite pulses prevent a large portion of the sample from experiencing the 180° condition. For larger τ , as the ratio of t_p to τ makes the pulses appear more like delta functions, the oscillations become more apparent, as expected. These undulations are not observed in the corresponding actual signals since they manifest themselves as a Gaussian decay in the signal due the variations in the phasing of the signals from the interaction of a large number of nuclei, as opposed to just a pair, as is modeled.

While not shown in Fig. 4.3, the experimental data was symmetrical as a function of off-resonance for the low Q probe configuration. The 90-90 signals were periodic as a function of off-resonance, in excellent agreement with the model. The peaks correspond to $\Delta f = \frac{m}{2\tau'}$, where the magnetization is locked along the \hat{i} direction, and

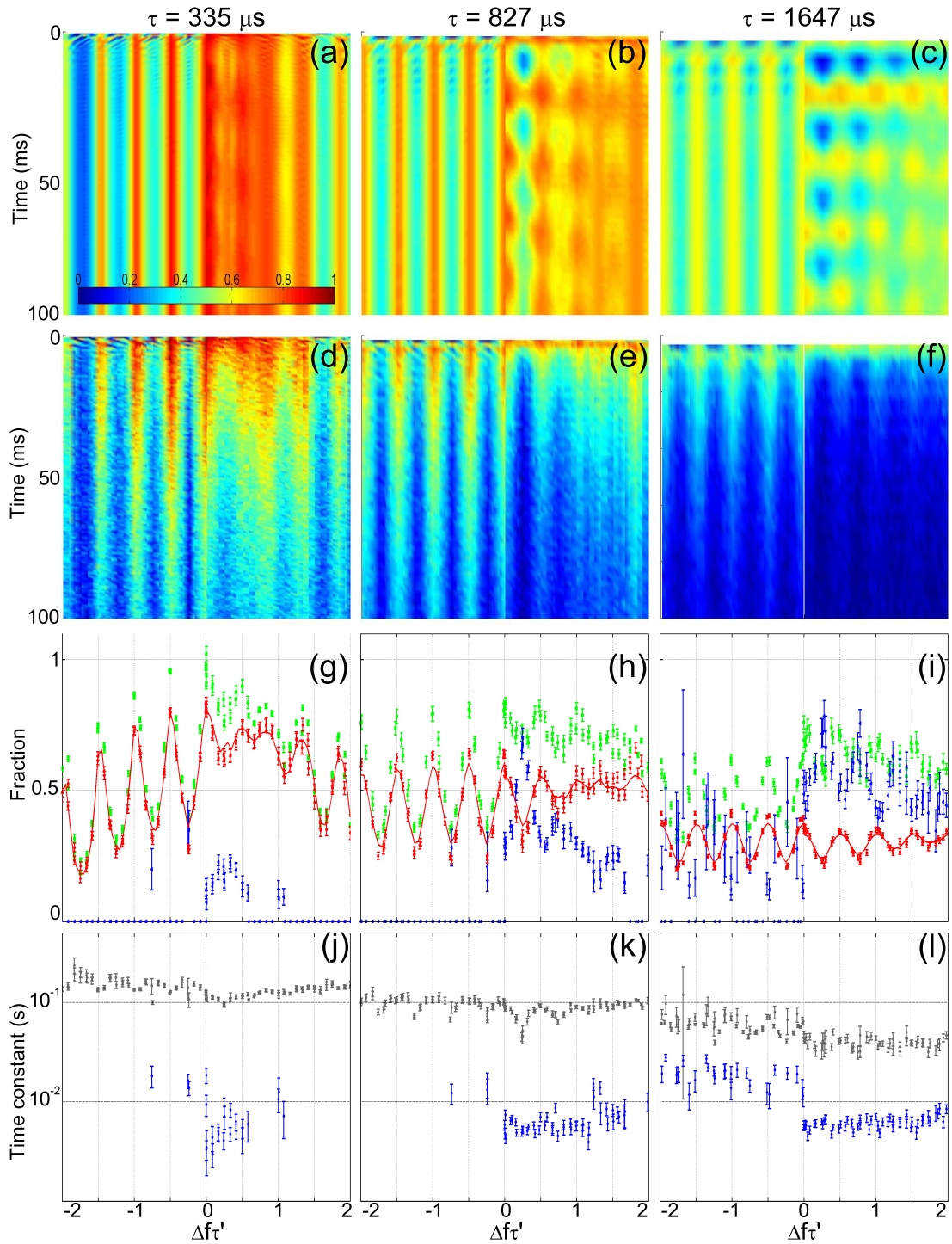


Figure 4.3: The theoretical (a)-(c) and experimental data (d)-(f) are compared with off-resonance for both 90-90 and 90-180 sequences, the left and right halves of each image respectively, for three values of τ . The model for a powder with finite pulses is from Section 4.2. The fit parameters A (green squares) and p_g (blue triangles) of the observed signal, the average echo (red circles) over the $\frac{2\pi}{\alpha_{y,eff}} \frac{\tau'}{\tau}$ period of the dipolar coupling for ω_y , and the predicted average echo (red line) are given in (g)-(i). The fit parameters T_{2e} (grey diamonds) and T_d (blue circles) are given in (j)-(l).

the troughs to $\Delta f = \frac{1}{4\tau'} + \frac{m}{2\tau'}$, where signal is lost due to the anti-resonant kicking. By increasing τ the sharpness of the oscillations is reduced since the linewidth of the sample begins to approach $\frac{1}{4\tau'}$. As this condition is met, the signal is no longer dominated by either the on or off-resonance effects, but by a mixture of the two. Similarly, the larger EFG component of the broad sample reduces the variation in signal behavior with frequency compared to the narrow sample, for the same experiments.

The 90-180 data, again agreeing well with the model, shows a similar periodicity as the 90-90 data in off-resonant behavior, but with notable differences. For instance, while having roughly the same period, the local maxima and minima are not all at the $\Delta f = \frac{m}{4\tau'}$ conditions. This is because strong dips in the average signal are not primarily due to signal lost to anti-resonant kicking, but to achieving the 180° condition. For low τ and small Δf the dips are fairly small because the 180° condition is hard to achieve at low τ with finite pulses. But as τ is increased a strong decay is observed first at the $\Delta f = \pm \frac{1}{4\tau'}$ condition and then later at $\Delta f = \frac{1}{4\tau'} + \frac{m}{2\tau'}$, as expected.

Fitting the data to Eq. (4.29), it was found that A roughly tracked the average signal for all 90-90s. This was because there was no rapid decay in the echo train due to nuclei achieving the 180° condition. For the 90-180s, however, A tracked the average signal well for short τ , but diverged for larger τ as the Gaussian component of the decay rapidly drove the average signal down. This is apparent at $\Delta f = \pm \frac{1}{4\tau'}$ for $\tau = 827 \mu\text{s}$. As τ increased the separation between A and the average echo became noticeable across all off-resonances, as more of the signal experienced the 180° condition. This same explanation is used for the behavior of p_g for 90-180s. For low τ , p_g is close to zero since the 180° condition is met for only a small subset of spins. Then, near the predicted value of τ_{min} at $\Delta f = \pm \frac{1}{4\tau'}$, p_g becomes substantial as the 180° condition is met for a larger percentage of the sample, approaching the $\frac{2}{3}$ rds

value predicted by Eq. (4.19). As p_g plateaus for large τ , it becomes significant across the entire range of off-resonances as the EFG inhomogeneity ensures a significant fraction of the spins experience the 180° condition, regardless of the off-resonance of the pulses.

While Fig. 4.3 focuses on the narrow sample at ω_y , in Fig. 4.4 it is shown that similar behaviors for 90-180 sequences at $|\Delta f| = \frac{1}{4\tau'}$ appear across all three NQR frequencies, even for a sample with a much larger EFG contribution to its linewidth. In particular, the values of p_g for $|\Delta f| = \frac{1}{4\tau'}$ are consistently higher than for $\Delta f = 0$, since more of the sample experiences the 180° condition. This also explains why the narrow sample consistently has a larger p_g for $|\Delta f| = \frac{1}{4\tau'}$ than the broad sample, but a smaller value for $\Delta f = 0$. Additionally, regardless of the contribution of linewidth due to EFG inhomogeneity, p_g approaches a constant value for $|\Delta f| = \frac{1}{4\tau'}$ as τ increases. The value of τ_{min} where this plateau is expected to arise comes from the argument in Sec. 4.4, and is marked by a vertical black line in Fig. 4.4. Beyond τ_{min} the measurements of T_d converged, as shown in Figs. 4.3 and 4.4, regardless of the sample or the off-resonance of the pulses. For ω_x and ω_y the converged values agree well with the theoretical values, after accounting for the effects of a powder sample. However, for both ω_y and ω_z the converged value was slightly higher than expected. It is known that the NO_2 ion in sodium nitrite exhibits rapid torsional oscillation about the x -axis of the PAF.[82] This would result in a reduction in the dipolar coupling strength for the ω_y and ω_z transitions.

As shown in Fig. 4.3, for the 90-90s there were very few off-resonance conditions at low τ that led to a significant Gaussian contribution to the echo train, since only a small portion of the nuclei experience the 180° condition. As τ increased, and the behavior of the signal became more uniform with frequency, T_d converged to a fixed value that was three times longer than the single crystal's value. A naive

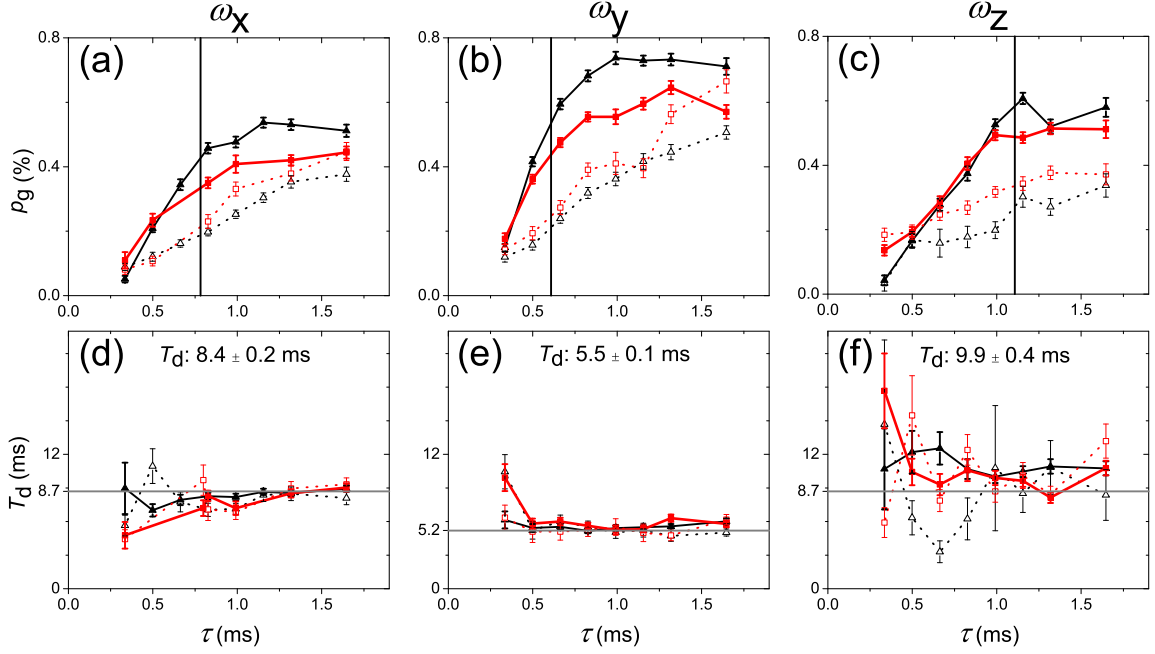


Figure 4.4: The percent of the decay in the echo train due to the Gaussian component p_g (a)-(c) and width of the Gaussian contribution T_d (d)-(f) as a function of τ for 90-180 sequences applied at the three transition frequencies. Values were obtained by fitting the echo trains of 90-180 sequences with Eq. (4.29). Measurements were made for both the narrow (black triangles) and broad (red squares) samples for $|\Delta f| = \frac{1}{4\tau'}$ (solid lines, symbols) and $\Delta f = 0$ (dashed lines, hollow symbols). The vertical line marks τ_{min} the theoretical minimum τ to observe a strong decay due to the dipolar coupling at $|\Delta f| = \frac{1}{4\tau'}$. This prediction does not depend on EFG inhomogeneity, as is experimentally validated since the plateau for the narrow sample matches that of the broad sample. Additionally, the predicted value accurately accounts for the impact of doubling the refocusing pulse length needed to perform the ω_z experiments. The measurements of T_d converge, regardless of the EFG inhomogeneity of the sample, close to the predicted values (grey lines). The average T_d , for $\tau > \tau_{min}$ and $\Delta f = 0, \pm \frac{1}{4\tau'}$, is given at the top of figures (d)-(f).

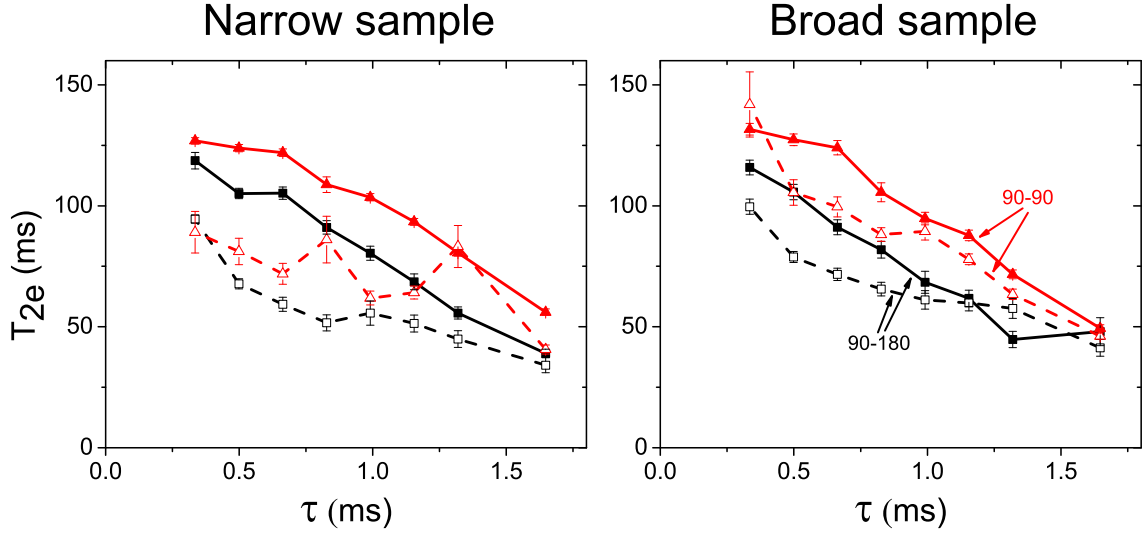


Figure 4.5: The value of T_{2e} for 90-180 (black squares) and 90-90 (red triangles) sequences is consistently greater when $\Delta f = 0$ (solid line and symbols) than for $|\Delta f| = \frac{1}{4\tau'}$ (dashed line and hollow symbols). 90-90s consistently produce longer T_{2e} s than 90-180s at the same off-resonance condition. For long τ , both sequences' on and off-resonance measurements converge, as the distinction between on and off-resonance signals disappears due to the EFG inhomogeneity. This also explains why the data for the broad sample shows less variation between $\Delta f = 0$ and $|\Delta f| = \frac{1}{4\tau'}$. Data is from the ω_y transition.

theoretical adjustment that ignores both EFG inhomogeneity and the powder average also predicts a lengthening of T_d , but only by a factor of two.

For a given τ , the measurements of T_{2e} varied by a factor of three within the range of off-resonances tested, a result comparable to the variations observed by Gregorovic et al. using PNT.[55] However, we observed longer values for T_{2e} for $\Delta f = \frac{m}{2\tau'}$ than for $\Delta f = \frac{1}{4\tau'} + \frac{m}{2\tau'}$, in contrast to Gregorovic, perhaps due to their focus on the long time echo data. Our general trend in T_{2e} as a function of τ was the same for all transition frequencies, and is shown for ω_y in Fig. 4.5. While our simple model does not predict the long time behavior, T_{2e} does seem correlated with the short time behavior caused by the 180° condition and anti-resonant kicking. For example, the 90-90 sequence at $\Delta f = 0$ predominantly produced a longer T_{2e} than the other sequences, for the

Table 4.4: The τ dependency of T_{2e} was found by fitting the observed values of T_{2e} at each τ value to Eq. (4.32) for $\Delta f = 0$ for both 90-180 and 90-90 SLSEs with the narrow sample.

	Narrow sample 90-180		Narrow sample 90-90	
	$T_{2e}(\tau = 400 \mu\text{s})$ ms	x	$T_{2e}(\tau = 400 \mu\text{s})$ ms	x
ω_x	83.3 ± 1.9	-0.19 ± 0.03	96.5 ± 2.3	-0.18 ± 0.03
ω_y	121.4 ± 9.4	-0.61 ± 0.11	128.8 ± 8.3	-0.37 ± 0.08
ω_z	206.5 ± 9.1	-0.30 ± 0.07	218.1 ± 8.4	-0.33 ± 0.05

same τ , in correspondence with the refocusing the W -levels. This is in contrast to the 90-180 sequence, where the W -levels are not refocused and there is less signal due to achieving the 180° condition, particularly for $|\Delta f| = \frac{1}{4\tau'}$ and the narrow sample. Additionally, for the 90-90 at $|\Delta f| = \frac{1}{4\tau'}$ the anti-resonant kicking causes a reduction in the initial signal.

The dependency of T_{2e} on τ was found by fitting the T_{2e} values for each sequence to the equation

$$T_{2e}(\tau) = T_{2e}(\tau = 400 \mu\text{s}) \left(\frac{\tau}{400 \mu\text{s}} \right)^x. \quad (4.32)$$

The fit parameters of Table 4.4 show that $T_{2e} \propto \tau^{-x}$ with $0.18 \leq x \leq 0.61$. This is in contrast to the τ^{-5} dependency observed by Marino and Klainer,[7] who operated at 77°K, however a weaker dependency has also been observed by Mikhaltsevitch and Rudakov at room temperature.[54] Additional work with sodium nitrite at 77°K suggests a more complex dependency between T_{2e} and τ . [49] Interestingly, it was found that the values of $T_{2e}(\tau = 400 \mu\text{s})$ decreased linearly with f_{NQR} for the on-resonant sequences.

For the real-world detection of illicit substances using NQR, the exact resonance frequency of the sample may only be known to within a certain range. This is due to the variation of the NQR frequencies with temperature, which can be several hundred

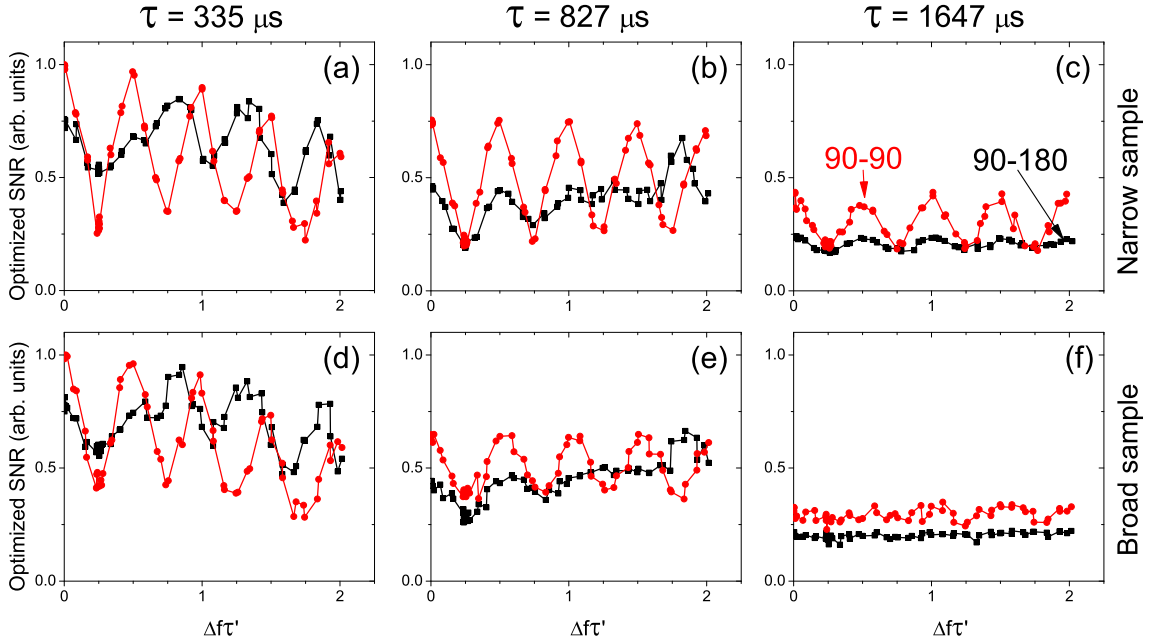


Figure 4.6: The optimal SNR calculated by integrating Eq. (4.29) for both 90-90 (red) and 90-180 (black) sequences with the experimentally derived fit parameters at ω_y for both the narrow (top row) and broad (bottom row) sample. The integration was performed from $t = 0$ to the time that maximized the SNR. While finite pulses would reduce the amount of time that signal that could be acquired, this adjustment is small and not included. SNRs are normalized to the 90-90, $\Delta f = 0$, $\tau = 335 \mu\text{s}$, $t_p = 100 \mu\text{s}$ signal for each sample. The increased EFG inhomogeneity of the broad sample averages the variation between the maxima and minima.

Hz per degree for a substance like RDX.[83] To prevent false negatives a detector operator would want to know that a useful signal can be detected at all frequencies within that range. To compare the sequences as functions of off-resonance, an optimal SNR was calculated by integrating Eq. (4.29) over the time found to maximize the SNR, with the results shown in Fig. 4.6. This allows us to define a useful signal as one achieving some minimum SNR. For short τ , the minimum possible SNR for the 90-90 sequence, over the given off-resonance domain, is considerably less than the minimum possible SNR of the 90-180 sequence, for both the narrow and broad samples. This is because the 90-90 sequence triggers a larger loss of signal due to anti-resonant kicking compared to that lost due to the 180° condition, which is inhibited at low τ due to finite pulses, for the 90-180. For the intermediate τ , the two sequences share the same minimum SNR for the narrow sample, as the signal lost to the 180° condition and the anti-resonant kicking become comparable between sequences. However, the 90-90 sequence is now slightly preferable for the broad sample at this intermediate τ . This shows that the optimal detection sequence for a given τ is a function of the relative strengths of the two dominant line broadening mechanisms. Finally, we note that at high τ the 90-90 sequence is stronger for both samples, with considerably less variation in amplitude with frequency for the broad sample, due to its larger EFG inhomogeneity.

4.6 Conclusion

Despite the naive simplicity of the two-spin model, we have shown that it still qualitatively predicts the short-time behavior of the spin-locked signal as a function of off-resonance. Furthermore, the model permits us to identify the conditions under which we would expect a significant fraction of the signal to exhibit decay due to

dipolar coupling alone. Namely, when the 180° condition is met for a large portion of the sample, the NQR signal experiences a rapid initial decay. To achieve this for a powder sample, one should operate with a 90-180 sequence, with an off-resonance $\Delta f = \pm \frac{1}{4\tau}$, and with pulse spacing governed by $\tau \geq \sqrt{\frac{t_p}{\alpha_{y_{eff}}}}$. We have shown that operating with these conditions produces an initially Gaussian decay whose width measures the dipolar coupling between the nitrogen nuclei, as shown in NaNO_2 . Our measurements agree within 15% of the theoretical prediction after accounting for the powder nature of the sodium nitrite samples, and we believe that motion may account for part of the deviations of the experimental values from the theoretical values. Successfully performed for the three transition frequencies, this is a robust measurement that does not vary with the EFG inhomogeneity of our samples, nor does it require an exact π pulse across the sample, as required in NMR.

For the purposes of substance detection, achieving the 180° condition for a large portion of the sample is to be avoided since it reduces the observed signal. However, the same conditions that can trigger the Gaussian decay can also trigger a loss of signal due to the anti-resonant kicking with a 90-90 sequence. By knowing the strength of the dipolar coupling relative to the measured linewidth it is possible to choose between these sequences to minimize the losses from their off-resonance effects. For substances where the dipolar coupling is unknown, this is not a problem. By simply running 90-180 sequences at $\Delta f = \pm \frac{1}{4\tau}$ with ever increasing τ the dipolar coupling should eventually reveal itself, allowing an accurate measurement to be made.

For short τ , the 180° condition is suppressed for 90-180 sequences at $\Delta f = \pm \frac{1}{4\tau}$ due to the large value of the ratio of the pulse length to τ . This is beneficial for substance detection because it preserves the signal size. However, as discussed in the next chapter, relatively small deviations of the pulse from square can trigger the 180°

condition, and corresponding decay, even with short pulse spacing.

Chapter 5: The Role of Imperfect Pulses

A practical implementation of NQR for substance detection would aim to maintain the highest SNR possible. For our configuration, this is achieved by using an antenna with a high Q to excite the sample and detect the signal. The pulse sequence would be designed to prevent the 180° condition from being met, since it could cause the average signal to be smaller than possible. While the previous chapter would suggest that the parameters under which the 180° condition is met for a large portion of a sample are well understood, some preliminary experimental work with sodium nitrite suggested a more complex picture. When performing 90-180 sequences with a high Q (180) probe, which would be desired for substance detection, we obtained asymmetric average signals, like those shown in Fig. 5.1, most noticeably at the $\Delta f = \pm \frac{1}{4\tau}$ conditions, and for short values of τ . This asymmetry was never observed for any 90-90 sequence. Since achieving the 180° condition leads to a rapid decay in signal strength for the echo train, the asymmetric data implied that the percentage of signal from spins experiencing the 180° condition was varying with the sign of the off-resonance.

To understand the asymmetry's source, the shapes of the actual refocusing pulses were used to model the behavior of a powder during a SLSE sequence. The pulse shapes were obtained by measuring the strength of the magnetic field in the main coil with the voltage induced in a sniffer coil described in Chapter 3. Using the model of Section 4.2, the percent of the initial signal due to the spins experiencing an effective 180° rotation p_{th} was calculated, with examples shown in Figs. 5.2 and 5.3. We found p_{th} perfectly rank ordered the normalized average signal size at the $\Delta f = \pm \frac{1}{4\tau}$ condition across multiple configurations of the probe, as shown in Fig. 5.4(a). Additionally,

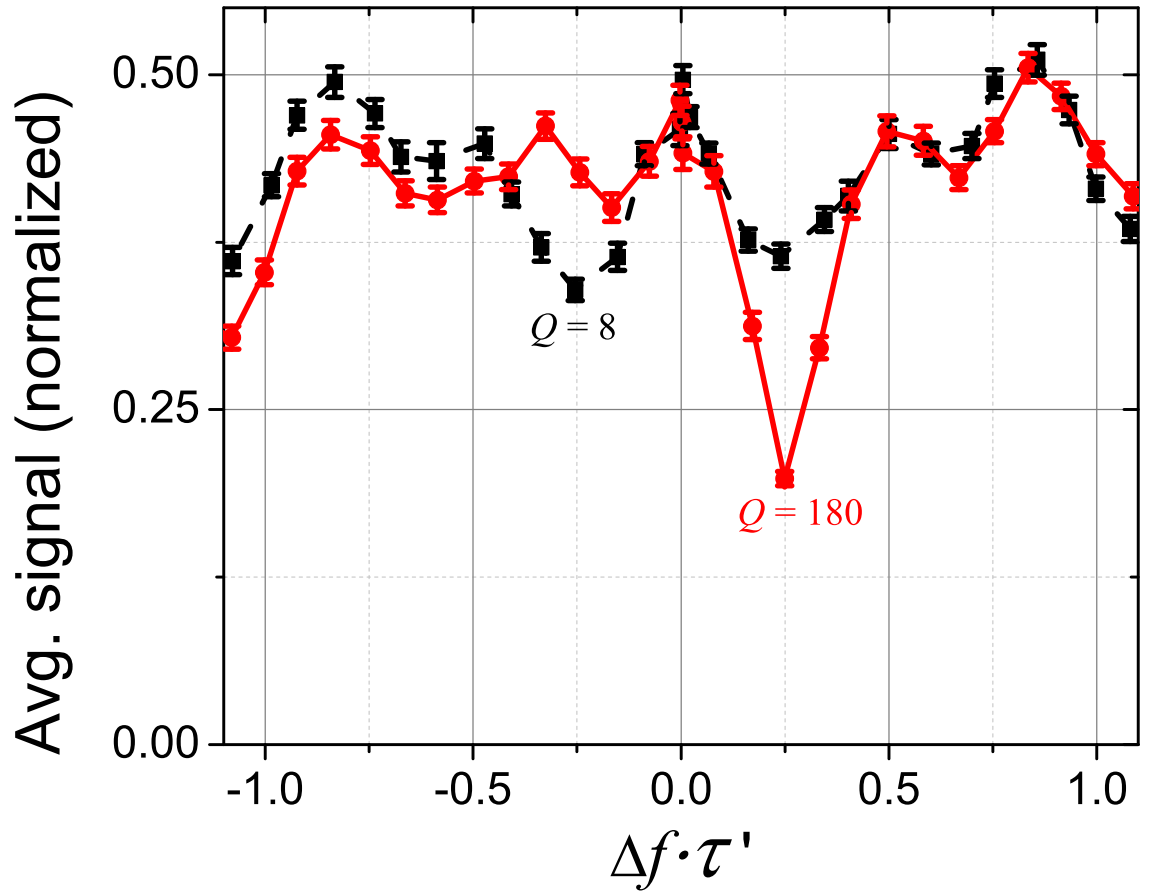


Figure 5.1: A plot of the average signal over 125 ms vs $\Delta f \cdot \tau'$ for fixed τ ($335 \mu\text{s}$) shows that the asymmetry between $\Delta f = \pm \frac{1}{4\tau'}$ was reduced by lowering the Q of the probe. Data was taken with a 90-180 sequence at ω_y , $t_p = 100 \mu\text{s}$, using the broad linewidth sample described in Chapter 4.

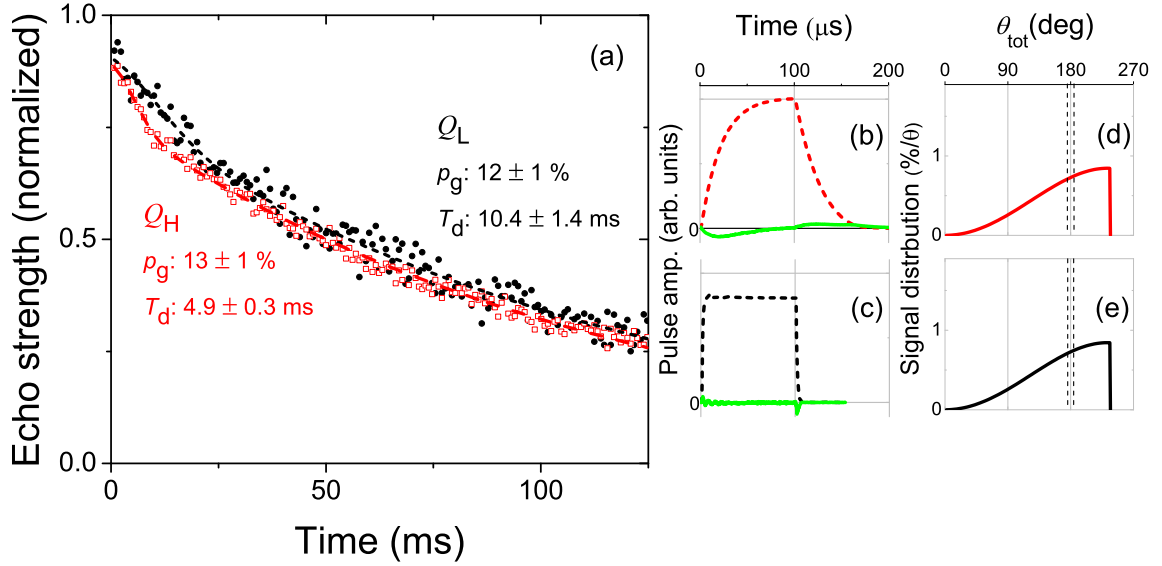


Figure 5.2: For $\Delta f = 0$ the echo trains (a) with high Q (Q_H , hollow red squares) and low Q (Q_L , black circles) are similar, despite their respective pulse shapes, (b) and (c), having very different real (dashed) and imaginary (green solid) components. This is understandable in view of the similarities of the calculated distributions of the initial signal as a function of θ_{tot} given in (d) and (e) for the pulse shapes to their left. The dashed black vertical lines correspond to the boundaries for $\theta_{tot} = \pi \pm d$ that determine the percentage p_{th} of the echo train due to a Gaussian component. This and the following data in this section are from a 90-180 sequence applied to the narrow sample at $\omega_y, \tau = 335 \mu s, t_p = 100 \mu s$.

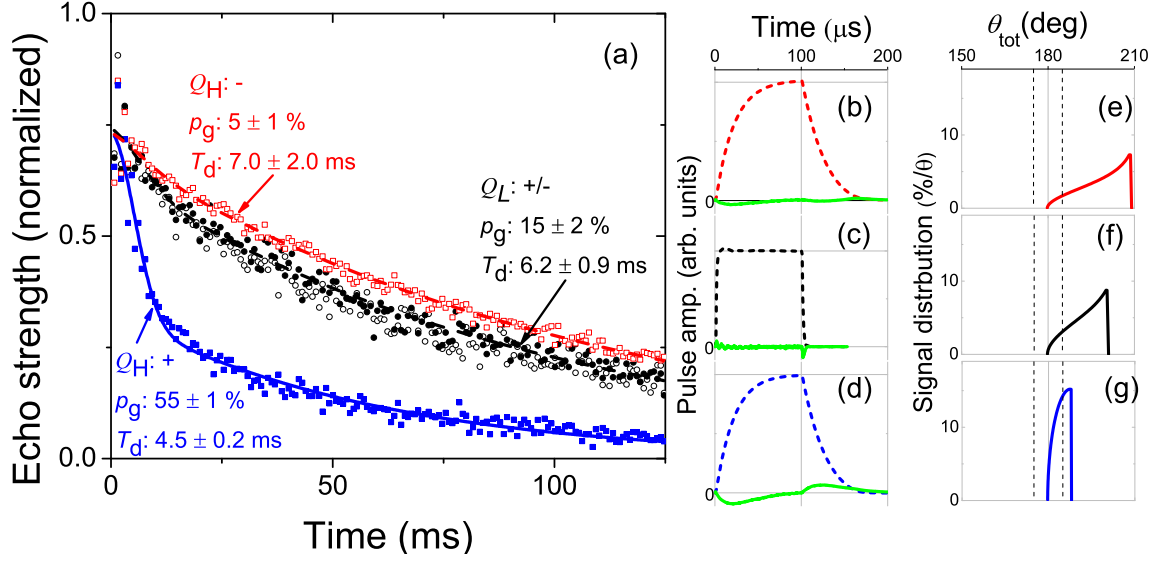


Figure 5.3: (Left) The echo trains (a) show that for a high Q (Q_H) probe a strong Gaussian component appeared at $\Delta f = +\frac{1}{4\tau'}$ (blue squares) whose width is somewhat below the prediction from Table 4.2. This requires further investigation. This component was absent for $\Delta f = -\frac{1}{4\tau'}$ (hollow red squares) and for both low Q (Q_L) trains at $\Delta f = +\frac{1}{4\tau'}$ (solid black circles) and $\Delta f = -\frac{1}{4\tau'}$ (hollow black circles). (Middle) Comparing pulse shapes, the Q_L configuration (c) has a different real (dashed) component compared to the Q_H configurations for both $\Delta f = -\frac{1}{4\tau'}$ (b) and $\Delta f = +\frac{1}{4\tau'}$ (d). Additionally, its small imaginary component (green solid) is less pronounced than both the Q_H $\Delta f = -\frac{1}{4\tau'}$ pulse and the Q_H $\Delta f = +\frac{1}{4\tau'}$ pulse, which has a large imaginary component. (Right) Corresponding to each pulse the distribution of the initial signal as a function of θ_{tot} was calculated. For the Q_L pulses, the distribution does not depend on the sign of Δf , which is why the echo trains for $\Delta f = -\frac{1}{4\tau'}$ and $\Delta f = +\frac{1}{4\tau'}$ are very similar. In comparison, for the Q_H pulses the combination of off-resonance and non-zero imaginary component works to reduce the distribution near $\theta_{tot} = 180^\circ$ for $\Delta f = -\frac{1}{4\tau'}$, while substantially increasing it for the $\Delta f = +\frac{1}{4\tau'}$ pulse distribution. For the former, the result is to reduce the strength of the observed Gaussian component compared to the Q_L trains. In the latter, the combination leads to the very strong decay.

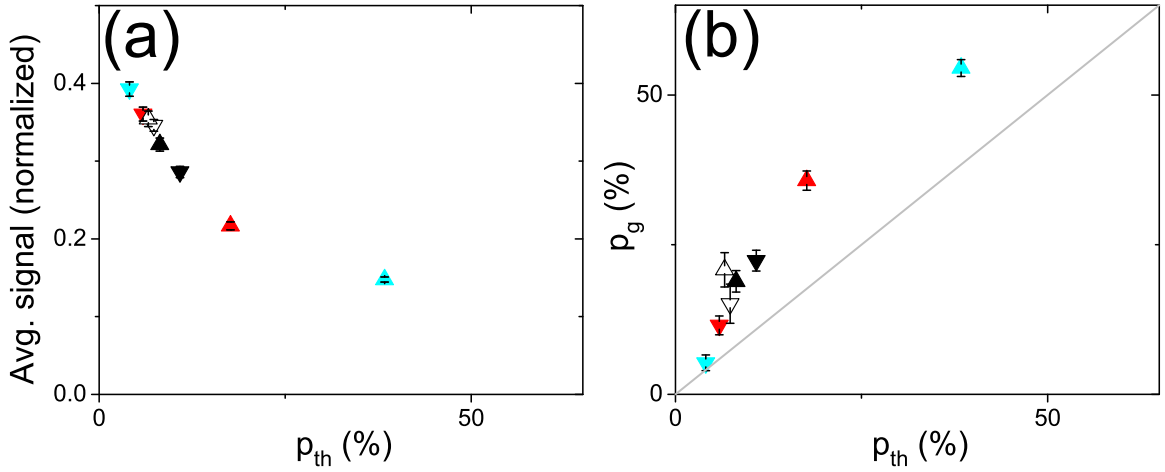


Figure 5.4: Average signal (a) and strength of the Gaussian contribution of the echo train (b) versus p_{th} , the calculated percent of the initial signal due to spins experiencing a 180° net rotation. For both values p_{th} does an excellent job rank ordering, validating the significance of the 180° condition to the behavior of the echo train. The data comes from several probe configurations. With a high Q (180) the probe was tuned to f_{NQR} (red), $f_{NQR} + \frac{1}{4\tau'}$ (green), and $f_{NQR} - \frac{1}{4\tau'}$ (blue). The hollow black data is at low Q (8) with the probe tuned to f_{NQR} . Data taken at $\Delta f = \frac{1}{4\tau'}$ is indicated by the upward triangles; $\Delta f = -\frac{1}{4\tau'}$, downward triangles. Data was taken over 125 ms.

fitting the echo train revealed p_{th} roughly predicted the Gaussian contribution associated with the percentage of spins experiencing a 180° rotation, as shown in Fig. 5.4(b). These results confirmed that the asymmetry of the average signal was due to variations in the distribution of spins experiencing the 180° rotation as a function of the pulse shapes.

By setting the imaginary component of the actual pulses to zero, the model produced symmetrical distributions of θ_{tot} for the high Q pulses at $\Delta f = \pm \frac{1}{4\tau'}$; these also conformed to the distributions from the low Q pulses at $\Delta f = \pm \frac{1}{4\tau}$. To see how the presence of a non-zero imaginary component could produce the asymmetric distributions, a fake pulse, shown in Fig. 5.5, was created that roughly mimicked the real pulse.

The net rotation due to this fake pulse at $\Delta f = \pm \frac{1}{4\tau'}$, *i.e.* the point of the major asymmetry in the data, was found by breaking the pulse into two nearly identical rotations, $\theta_{b1}\hat{n}_{b1}$ and $\theta_{b2}\hat{n}_{b2}$ differing only in the sign of their imaginary components:

$$\hat{n}_{b1} = \frac{R\hat{i} - I\hat{j} + W\hat{k}}{\theta_{b1}}, \quad \hat{n}_{b2} = \frac{R\hat{i} + I\hat{j} + W\hat{k}}{\theta_{b1}}; \quad (5.1)$$

$$\theta_{b1} = \theta_{b2} = \sqrt{R^2 + I^2 + W^2}, \quad (5.2)$$

where $W = \theta_a \frac{t_p}{\tau}$. Using quaternions to combine $\theta_{b1}\hat{n}_{b1}$ and $\theta_{b2}\hat{n}_{b2}$ as a single rotation $\theta_2\hat{n}_2$ [76, 84] reveals $\hat{n}_2 \cdot \hat{k} = 0$, making $\theta_{tot} = \pi$ via Eq. (4.17), when

$$\cos \frac{\theta_{b1}}{2} W = \sin \frac{\theta_{b1}}{2} \frac{RI}{\theta_{b1}}. \quad (5.3)$$

With a non-zero imaginary component, Eq. (5.3) can only be satisfied for one sign

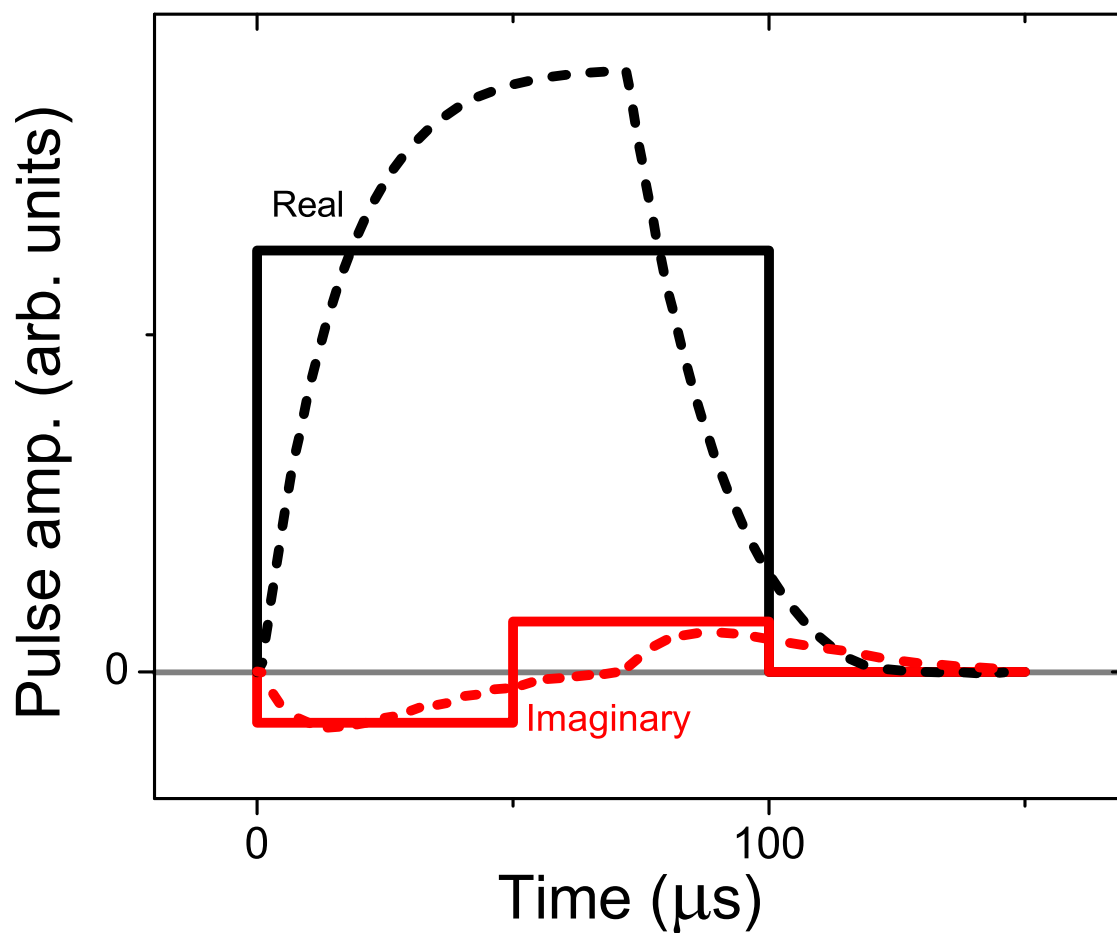


Figure 5.5: The real (black) and imaginary (red) components of an actual (dashed) and simplified (solid) refocusing pulse shape. The latter is useful for understanding the significance of the imaginary component to achieving the 180° condition.

of the off-resonance. This explains many observed phenomena. It explains the origin of the asymmetry, because the 180° condition now depends on the sign of the off-resonance. It explains why dropping the Q reduced the asymmetry, because it forced the imaginary component to zero. And finally, it explains why the asymmetry was reduced with τ : as τ increases, W approaches 0 and Eq. (5.3) is no longer satisfied for either sign of off-resonance.

This is an important observation for substance detection work. Operating with a high Q probe is desirable because of the higher SNR and lower power requirements for the rf pulsing. However, it can unintentionally cause the signal to decay, decreasing the efficiency of the search. As shown in Chapter 4, the 90-180 sequence can be preferred over the 90-90 for substance detection work, depending on the relative strengths of the broadening mechanisms, so avoiding the 90-180 sequence may not be advisable. Care must be taken in the design of the NQR detection configuration to balance the need for SNR and efficient sample detection, as determined by the shape of the pulses.

Chapter 6: Heteronuclear Dipolar Coupling

6.1 Introduction

In this thesis, we focus on three broadening mechanisms to explain the linewidth of the NQR signal. The first, EFG inhomogeneity, is an inhomogeneous broadening mechanism caused by variations in the local electric field of the nuclei in the sample. Its size is a function of the sample's history, from its manufacturing process to its handling.[60] The second, homonuclear dipolar coupling, is a homogenous broadening mechanism that should be constant across samples of the same substance. The previous chapters revealed the experimental conditions under which a SLSE triggered a strong response due to homonuclear coupling. This chapter addresses the role of the third broadening mechanism to a SLSE sequence: heteronuclear dipolar coupling, another homogenous broadening mechanism. Heteronuclear coupling here is the coupling between the NQR target nuclei and all other types of nuclei. While we focus on spin 1/2 nuclei in Sec. 6.2, one should be able to make similar arguments for other spin nuclei, as long as their transition frequencies are not close to the NQR frequencies. By finding the conditions where heteronuclear broadening is refocused, we show that the strong homonuclear response can still be observed for substances with heteronuclear broadening.

6.2 Theory

To understand heteronuclear coupling's response to a multipulse sequence, the progression of a system modeled as a single spin- I (spin-1) nucleus, with angular momentum \mathbf{I} , coupled to a set of N_K spin- K (spin-1/2) nuclei, each with angular momentum $\mathbf{K}^{(k)}$, is examined through the evolution of the corresponding density matrix $\varrho(t)$. As before, the quadrupole Hamiltonian is

$$H_Q = \frac{eQ}{6I(2I-1)} [V_{xx}(3I_x^2 - I^2) + V_{yy}(3I_y^2 - I^2) + V_{zz}(3I_z^2 - I^2)].$$

The second derivatives of the electric potential V are found using the \hat{x} , \hat{y} , \hat{z} coordinate axes of the PAF. However, unlike sodium nitrite, for the sample of interest in this chapter, p-chloroaniline, there are two different PAFs within each unit cell, but with the \hat{x} axes still parallel.[85] For this reason we will focus on the ω_x transition, although the results should apply to any transition frequency where the corresponding axes are aligned.

During the refocusing pulses for this model, H_{rf} is

$$H_{rf}(t) = -\hbar B \hat{B} \cdot \left(\gamma_I \mathbf{I} + \gamma_K \sum_{k=1}^{N_K} \mathbf{K}^{(k)} \right) \cos \omega_{rf} t. \quad (6.1)$$

For our sample, \mathbf{K} corresponds to hydrogen with gyromagnetic ratio γ_K .

The heteronuclear dipolar Hamiltonian between the spin-1 nucleus and the N_k spin-1/2 nuclei is H_{IK} , where

$$H_{IK} = \sum_k^{N_K} \mathbf{K}^{(k)} \cdot \mathbf{D}_k \cdot \mathbf{I}, \quad (6.2)$$

and

$$\mathbf{D}_k \equiv \frac{\mu_0}{4\pi} \gamma_I \gamma_K \hbar^2 \frac{1}{r_k^3} \times (\mathbf{1} - 3\hat{\mathbf{r}}_k \otimes \hat{\mathbf{r}}_k), \quad (6.3)$$

and $\mathbf{r}_k = r_k \hat{\mathbf{r}}_k$ is the displacement vector between the spin 1 and k^{th} spin 1/2 nuclei. For convenience, the operator \mathbf{I} is expressed as

$$\mathbf{I} = (|y\rangle\langle z| + |z\rangle\langle y|)\hat{x} + (-i|x\rangle\langle z| + i|z\rangle\langle x|)\hat{y} + (|y\rangle\langle x| + |x\rangle\langle y|)\hat{z}, \quad (6.4)$$

so that it is clear that H_{IK} only connects states of different quadrupole eigenenergies. The homonuclear dipolar Hamiltonian between the spin 1/2 nuclei H_K is similarly defined, as is homonuclear dipolar Hamiltonian between the spin 1 nuclei H_I . In order to focus on the effects of heteronuclear coupling, H_I is dropped from this model, having already been treated in detail in Chapter 4. However, we discuss its contribution to the signal in Sec. 6.4.

6.2.1 Evolution

As in Chapter 4, to find the evolution of $\varrho(t)$ due a series of repeat units $(\tau - \theta_{1x} - \tau)_N$, we begin with the Liouville equation, Eq. (2.21), where the total Hamiltonian H is given by

$$H = H_Q + H_K + H_{IK} + H_{rf}(t). \quad (6.5)$$

When the rf is off, such as between pulses, the Hamiltonian is static and the evolution of the density matrix is

$$\varrho(t) = e^{-\frac{i}{\hbar}H(t-t_0)} \varrho(t_0) e^{\frac{i}{\hbar}H(t-t_0)}, \quad (6.6)$$

where $H = H_Q + H_K + H_{IK}$ and $\varrho(t_0)$ is the density matrix before the free evolution. In principle H can be diagonalized to a basis $|\psi_n\rangle$ with eigenvalues ϵ_n , allowing the free evolution operator to be written as

$$e^{-\frac{i}{\hbar}H(t-t_0)} = e^{-\frac{i}{\hbar}\sum_n \epsilon_n |\psi_n\rangle\langle\psi_n|(t-t_0)} \quad (6.7)$$

$$= \sum_n |\psi_n\rangle\langle\psi_n| e^{-\frac{i}{\hbar}\epsilon_n(t-t_0)}. \quad (6.8)$$

It is not computationally viable, however, to diagonalize H because of the large number of particles involved. Using perturbation theory, approximate expressions for $|\psi_n\rangle$ and ϵ_n are found by taking $H_0 = H_Q + H_K$ as the unperturbed Hamiltonian and H_{IK} as the perturbation. This a reasonable assumption when $\gamma_K \gg \gamma_I$, as in our sample where the ratio of $\gamma_K/\gamma_I \approx 14$. [86] Because H_{IK} only joins states with different quadrupole energies, non-degenerate perturbation theory can be used. Given the eigenstates of H_0 , $H_0|\alpha\beta\rangle = \epsilon_{\alpha\beta}|\alpha\beta\rangle$, where α corresponds to an eigenstate of H_Q and β to an eigenstate of H_K , the surviving lowest order correction to the energy will come from

$$\epsilon_n \approx \epsilon_{\alpha\beta} + \Delta\epsilon_{\alpha\beta}, \text{ where} \quad (6.9)$$

$$\Delta\epsilon_{\alpha\beta} = \sum_{j \neq \alpha} \sum_l \frac{|\langle jl|H_{IK}|\alpha\beta\rangle|^2}{\epsilon_{\alpha\beta} - \epsilon_{jl}}, \quad (6.10)$$

while for the wavefunction it is

$$|\psi_n\rangle \approx |\alpha\beta\rangle + \sum_{j \neq \alpha} \sum_l |jl\rangle \frac{\langle jl|H_{IK}|\alpha\beta\rangle}{\epsilon_{\alpha\beta} - \epsilon_{jl}}. \quad (6.11)$$

As discussed below, the experimental NQR linewidth is on the order of 100 Hz, while the NQR frequency is on the order of 1 MHz. Therefore, the ratio $R = \frac{\langle jI|H_{IK}|\alpha\beta\rangle}{\epsilon_{\alpha\beta} - \epsilon_{jl}}$ is on the order 10^{-4} , making $|\psi_n\rangle \approx |\alpha\beta\rangle$. This approximation permits the free evolution operator $e^{-\frac{i}{\hbar}H\tau}$ to be approximated in terms of $|\alpha\beta\rangle$:

$$e^{-\frac{i}{\hbar}H(t-t_0)} \approx \sum_m |\alpha\beta\rangle\langle\alpha\beta| e^{-\frac{i}{\hbar}(\epsilon_{\alpha\beta} + \Delta\epsilon_{\alpha\beta})(t-t_0)}. \quad (6.12)$$

To solve for the evolution due to the rest of the repeat unit it will be beneficial to use the interaction representation of \bar{H}_0 , where

$$\bar{H}_0 \equiv \bar{H}_Q + H_K, \quad (6.13)$$

and \bar{H}_Q is the reduced quadrupole Hamiltonian

$$H_Q = \bar{H}_Q - \Delta H_Q \quad (6.14)$$

$$\bar{H}_Q = \frac{\omega_{rf}}{\omega_{NQR}} H_Q, \quad (6.15)$$

where ΔH_Q is the same as in Eq. (4.4). While \bar{H}_0 and H_0 have the same eigenstates, $|\alpha\beta\rangle$, they will have different eigenvalues: $\epsilon_{\alpha\beta}$ for H_0 and $\bar{\epsilon}_{\alpha\beta}$ for \bar{H}_0 . After a period τ of free evolution, the density matrix in the interaction representation becomes

$$\tilde{\rho}(t = t_0 + \tau) = e^{\frac{i}{\hbar}\bar{H}_0 t} e^{-\frac{i}{\hbar}H\tau} e^{-\frac{i}{\hbar}\bar{H}_0 t_0} \tilde{\rho}(t_0) h.c. \quad (6.16)$$

$$= \left(\sum_{\alpha, \beta} |\alpha\beta\rangle\langle\alpha\beta| e^{-\frac{i}{\hbar}\Delta\epsilon_{\alpha\beta}\tau} \right) e^{-\frac{i}{\hbar}\Delta H_Q \tau} \tilde{\rho}(t_0) h.c., \quad (6.17)$$

where the last expression uses Eq. (6.12), $\bar{H}_0 = H_0 - \Delta H_Q$. The dipole operator $D \equiv \sum_{\alpha,\beta} |\alpha\beta\rangle\langle\alpha\beta| e^{-\frac{i}{\hbar}\Delta\epsilon_{\alpha\beta}\tau}$ simplifies:

$$D = \sum_{\beta} \sum_{\alpha=x,y,x} |\alpha\beta\rangle\langle\alpha\beta| e^{-\frac{i}{\hbar}\Delta\epsilon_{\alpha\beta}\tau} \quad (6.18)$$

$$= \sum_{\beta} \exp \left\{ -\frac{i}{\hbar}\tau [|x\beta\rangle\langle x\beta| \Delta\epsilon_{x\beta} + |y\beta\rangle\langle y\beta| \Delta\epsilon_{y\beta} + |z\beta\rangle\langle z\beta| \Delta\epsilon_{z\beta}] \right\}, \quad (6.19)$$

and becomes

$$D = \sum_{\beta} \exp \left\{ -\frac{i}{\hbar}\tau |x\beta\rangle\langle x\beta| \Delta\epsilon_{x\beta} \right\} \quad (6.20a)$$

$$\exp \left\{ -\frac{i}{\hbar}\tau (\mathbf{1} + I_{x4})(\Delta\epsilon_{y\beta} + \Delta\epsilon_{z\beta}) |\beta\rangle\langle\beta| \right\} \quad (6.20b)$$

$$\exp \left\{ -\frac{i}{\hbar}\tau I_{x3}(\Delta\epsilon_{y\beta} - \Delta\epsilon_{z\beta}) |\beta\rangle\langle\beta| \right\}, \quad (6.20c)$$

where $|\beta\rangle\langle\beta|$ shows that the state of the K spins is preserved. The terms in Eqs. (6.20a) and (6.20b) can be dropped because they will not contribute to the evolution of the signal, reducing D to

$$D = \sum_{\beta} e^{-\frac{i}{\hbar}\tau I_{x3}(\Delta\epsilon_{y\beta} - \Delta\epsilon_{z\beta}) |\beta\rangle\langle\beta|}. \quad (6.21)$$

In contrast, during the pulse, the contribution of H_{IK} is ignored since H_{rf} is much stronger for the nuclei that will produce the signal. This assumption was found to be

valid for H_I in Chapter 4. The perturbing Hamiltonian H_1 is then given by

$$H_1 = -\Delta H_Q + H_{rf}(t), \quad (6.22)$$

where

$$\Delta H_Q = \hbar(\Delta\omega I_{x3} + \Delta\omega' I_{x4}), \quad (6.23)$$

with $\Delta\omega = \omega_{rf} - \omega_x$, $\Delta\omega' = \frac{1}{3} \frac{(\omega_y - \omega_z)(\omega_x - \omega_{rf})}{\omega_x}$, $H_{rf} = -\omega_1 \hbar I_x \cos(\omega_{rf} t)$. In the interaction representation of \bar{H}_0 , the perturbation is given by

$$\begin{aligned} \tilde{H}_1 &= -\Delta H_Q + e^{\frac{i}{\hbar} \bar{H}_0 t} H_{rf}(t) e^{-\frac{i}{\hbar} \bar{H}_0 t} \\ &= -\Delta H_Q - \hbar\omega_1 I_{x1}, \end{aligned} \quad (6.24)$$

where in the last line we have used the secular approximation. The evolution of the density matrix during the pulse is

$$\tilde{\rho}(t + t_p) = e^{-\frac{i}{\hbar} \tilde{H}_1 t_p} \tilde{\rho}(t) e^{\frac{i}{\hbar} \tilde{H}_1 t_p}, \quad (6.25)$$

where

$$e^{-\frac{i}{\hbar} \tilde{H}_1 t_p} = e^{i(\Delta\omega I_{x3} + \omega_1 I_{x1}) t_p} e^{i\Delta\omega' t_p I_{x4}}. \quad (6.26)$$

Using Eqs. (6.17) and (6.21) the complete evolution due to a repeat unit can now be

written as

$$\tilde{\varrho}(t + 2\tau + t_p) = \sum_{\beta} e^{-\frac{i}{\hbar}(\Delta\epsilon_{y\beta} - \Delta\epsilon_{z\beta})\tau I_{x3}} |\beta\rangle\langle\beta| \quad (6.27a)$$

$$e^{i\Delta\omega\tau I_{x3}} e^{i(\Delta\omega t_p I_{x3} + \omega_1 t_p I_{x1})} e^{i\Delta\omega I_{x3}\tau} \quad (6.27b)$$

$$e^{i\Delta\omega'\tau' I_{x4}} \quad (6.27c)$$

$$\sum_{\beta'} e^{-\frac{i}{\hbar}(\Delta\epsilon_{y\beta} - \Delta\epsilon_{z\beta})\tau I_{x3}} |\beta'\rangle\langle\beta'| \quad (6.27d)$$

$$\tilde{\varrho}(t) h.c. \quad (6.27e)$$

The exponential operator containing I_{x4} will not contribute to the evolution of the signal, and is dropped: it only includes the identity operator and the states not addressed by the rf pulse. As a result the only remaining operators are the fictitious angular momentum operators, the product of which can be represented as a single rotation operator of angle θ_{β} and direction \hat{n}_{β} found through Eqs. (4.17) and (4.18), where $\theta_a = [\Delta\omega - (\Delta\epsilon_{y\beta} - \Delta\epsilon_{z\beta})]\tau$, $\hat{n}_a = \hat{x}_3$, $\theta_b \equiv t_p\sqrt{\omega_1^2 + \Delta\omega^2}$, and $\hat{n}_b = t_p\frac{\omega_1\hat{x}_1 + \Delta\omega\hat{x}_3}{\theta_b}$. This means that \hat{n}_{β} lies in the x_1x_3 -plane. The final expression is

$$\tilde{\varrho}(t + 2\tau') = \sum_{\beta} e^{i\theta_{\beta}\mathbf{I}_x \cdot \hat{n}_{\beta}} |\beta\rangle\langle\beta| \tilde{\varrho}(t) h.c., \quad (6.28)$$

with the evolution over N pulses being

$$\tilde{\varrho}(t_0 + 2N\tau') = \sum_{\beta} e^{iN\theta_{\beta}\mathbf{I}_x \cdot \hat{n}_{\beta}} |\beta\rangle\langle\beta| \tilde{\varrho}(t_0) h.c. \quad (6.29)$$

As will be discussed in Sec. 6.2.3, before the application of a repeat unit, the components of $\tilde{\varrho}(t_0)$ that produce signal can be expressed as

$$\tilde{\varrho}(t_0) = \sum_{\beta} \sum_{j=1}^3 c_j \mathbf{I}_x \cdot \hat{x}_j |\beta\rangle \langle \beta| \quad (6.30)$$

$$= \sum_{\beta} \mathbf{I}_x \cdot \{ \hat{n}_{\beta} [(c_1 \hat{x}_1 + c_3 \hat{x}_3) \cdot \hat{n}_{\beta}] + \hat{n}_{\beta\perp} [(c_1 \hat{x}_1 + c_3 \hat{x}_3) \cdot \hat{n}_{\beta\perp}] + c_2 \hat{x}_2 \} |\beta\rangle \langle \beta|, \quad (6.31)$$

where $\hat{n}_{\beta\perp} \equiv \hat{n}_{\beta} \times \hat{x}_2$, and the coefficients c_j for a SLSE are given in Sec. 6.2.3. Recognizing that[74]

$$e^{i\theta \mathbf{I}_x \cdot \hat{n}} (\mathbf{I}_x \cdot \hat{n}_0) e^{-i\theta \mathbf{I}_x \cdot \hat{n}} = \mathbf{I}_x \cdot [\cos \theta \hat{n}_0 + (1 - \cos \theta) \hat{n} (\hat{n} \cdot \hat{n}_0) + \sin \theta (\hat{n}_0 \times \hat{n})] \quad (6.32)$$

it is possible to see that after N repeat units with finite θ , as in Eq. (6.29), that the only terms of the density matrix that contribute to the signal are

$$\tilde{\varrho}(t) = \sum_{\beta} (\mathbf{I}_x \cdot \hat{n}_{\beta}) (c_1 \hat{x}_1 + c_3 \hat{x}_3) \cdot \hat{n}_{\beta} |\beta\rangle \langle \beta|. \quad (6.33)$$

The I_{x3} term makes no contribution to the observed signal, and, as explained later, phase cycling results in $c_3 = 0$. [74] Therefore the effective density matrix reduces to

$$\tilde{\varrho}(t) = \sum_{\beta} c_1 I_{x1} |\beta\rangle \langle \beta| (\hat{x}_1 \cdot \hat{n}_{\beta})^2, \quad (6.34)$$

which is the projection model of Chapter 2.

The above is for a single spin-1 nucleus. Expanding the density matrix to include

all N_I nuclei with similar directions for \hat{x}

$$\tilde{\varrho}(t) = \sum_{i=1}^{N_I} \sum_{\beta} c_1 I_{x1}^{(i)} |\beta\rangle \langle \beta| (\hat{x}_1 \cdot \hat{n}_{\beta}^{(i)})^2. \quad (6.35)$$

Values of $\hat{n}_{\beta}^{(i)}$ are given by \hat{n}_{tot} of Eq. (4.18), replacing $\Delta\omega$ with $\Delta\bar{\omega} + \delta\omega^{(i)}$, where

$$\Delta\bar{\omega} = \bar{\omega}_x - \omega_{rf}, \quad (6.36)$$

$\bar{\omega}_x$ is the average NQR frequency, and $\delta\omega^{(i)}$ is the deviation from this average by a particular nucleus i . For hard pulses, i.e. $\omega_1 \gg \delta\omega^{(i)}$, the rotation axis $\hat{n}_{\beta}^{(i)}$ is a function of

$$\theta_b \hat{n}_b = t_p (\omega_1 \hat{x}_1 + \Delta\bar{\omega} \hat{x}_3) \quad (6.37)$$

$$\theta_a^{(i)} \hat{n}_a^{(i)} = \tau [\Delta\bar{\omega} + \delta\omega^{(i)} + (\Delta\epsilon_{y\beta} - \Delta\epsilon_{z\beta})] \hat{x}_3. \quad (6.38)$$

Significantly, the broadening mechanisms $\delta\omega^{(i)}$ and $(\Delta\epsilon_{y\beta} - \Delta\epsilon_{z\beta})$ do not appear separately in the above rotation, but are summed together.

6.2.2 The observable

The sample is excited by the same coil used to detect the signal. In this case the signal is proportional to

$$\langle \mathbf{I} \cdot \hat{B} \rangle = \text{Tr}\{\mathbf{I} \cdot \hat{B}_{\varrho}\}, \quad (6.39)$$

and the average ω_x signal from the spin-1 nuclei with the same \hat{x} of their PAFs is

$$\langle \mathbf{I} \cdot \hat{B} \rangle = \frac{\hat{x} \cdot \hat{B}}{N_I} \sum_{i=1}^{N_I} \text{Tr}\{I_x^{(i)} \varrho\} \quad (6.40)$$

$$= \frac{\hat{x} \cdot \hat{B}}{N_I} \sum_{i=1}^{N_I} \text{Tr}\{\tilde{I}_x^{(i)} \tilde{\varrho}\} \quad (6.41)$$

$$= \frac{\hat{x} \cdot \hat{B}}{N_I} \sum_{i=1}^{N_I} 2 \left[\text{Tr}\{I_{x1}^{(i)} \tilde{\varrho}\} \cos \omega_{rf} t - \text{Tr}\{I_{x2}^{(i)} \tilde{\varrho}\} \sin \omega_{rf} t \right], \quad (6.42)$$

when solved in the interaction representation of \bar{H}_0 . From the projection model, the locked signal only contains the $I_{x1}^{(i)}$ term, allowing the $I_{x2}^{(i)}$ term to be dropped. Further, the double summation in Eq. (6.35) can be replaced by a double integral over two normalized distribution functions, $f(\delta\omega)$ for the electric field gradient distribution and $g(\Delta\epsilon_y - \Delta\epsilon_z)$ for the distribution in heteronuclear dipolar coupling:

$$\langle \mathbf{I} \cdot \hat{B} \rangle = c_1 \cos \omega_{rf} t (\hat{x} \cdot \hat{B}) \int d(\delta\omega) f(\delta\omega) \int d(\Delta\epsilon_y - \Delta\epsilon_z) g(\Delta\epsilon_y - \Delta\epsilon_z) (\hat{x}_1 \cdot \hat{n}_\beta)^2. \quad (6.43)$$

This double integral is equivalent to

$$\langle \mathbf{I} \cdot \hat{B} \rangle = c_1 \cos \omega_{rf} t (\hat{x} \cdot \hat{B}) \int d(\delta\varpi) h(\varpi) (\hat{x}_1 \cdot \hat{n}_\beta [\theta_a(\Delta\bar{\omega}, \delta\varpi), \theta_b(\Delta\bar{\omega}, \omega_1)])^2 \quad (6.44)$$

where $\delta\varpi = \delta\omega + \Delta\epsilon_y - \Delta\epsilon_z$, and the linewidth function $h = f * g$ is the convolution of f with g . In the above we emphasize the functional dependency of \hat{n}_β , θ_a , and θ_b on the broadening $\delta\bar{\omega}$ and the pulse parameters $\Delta\bar{\omega}$ and ω_1 . The broadening from the two different mechanisms contribute in the same way to the final signal.

In Chapter 4 we showed how the 90-180 SLSE should refocus broadening due EFG inhomogeneity.[73] That EFG and heteronuclear dipolar coupling contribute in the same way to the signal allows us to extend that conclusion to broadening due to heteronuclear coupling. The above solution, Eq. (6.44), is for a single crystal. To obtain the powder averaged signal the integration on the direction cosine $\hat{x} \cdot \hat{B}$ would be made, again with $\omega_1 = \gamma B \hat{x} \cdot \hat{B}$.

6.2.3 Initial density matrix

As shown in Fig. 6.1, subtle differences in the timing of the sequence before the application of the repeat unit can have big impacts on the SLSE signal behavior. To derive an expression for the density matrix before the repeat units as they occur in our experiments, it is assumed that the sample is in thermal equilibrium and at the high-temperature limit. In this case the initial density matrix $\rho(0)$ is taken as the reduced density matrix of H_Q [11]

$$\rho(t < 0) = \hbar\omega_x \mathbf{I}_x \cdot \hat{x}_3 |\beta\rangle\langle\beta|. \quad (6.45)$$

The rf pulse during excitation is $\mathbf{B} = B\hat{B} \cos(\omega_{rf}t + \pi/2)$, which differs in phase by $\pi/2$ compared to the refocusing pulse. Similar to the derivation in Eq. (6.24), in the interaction representation of \bar{H}_0 , the perturbing Hamiltonian of the excitation pulse is given by

$$\tilde{H}_1 = -\Delta H_Q + e^{\frac{i}{\hbar}\bar{H}_0 t} H_{rf}(t) e^{-\frac{i}{\hbar}\bar{H}_0 t} \quad (6.46)$$

$$= -\Delta H_Q + \omega_1 \hbar I_{x2}, \quad (6.47)$$

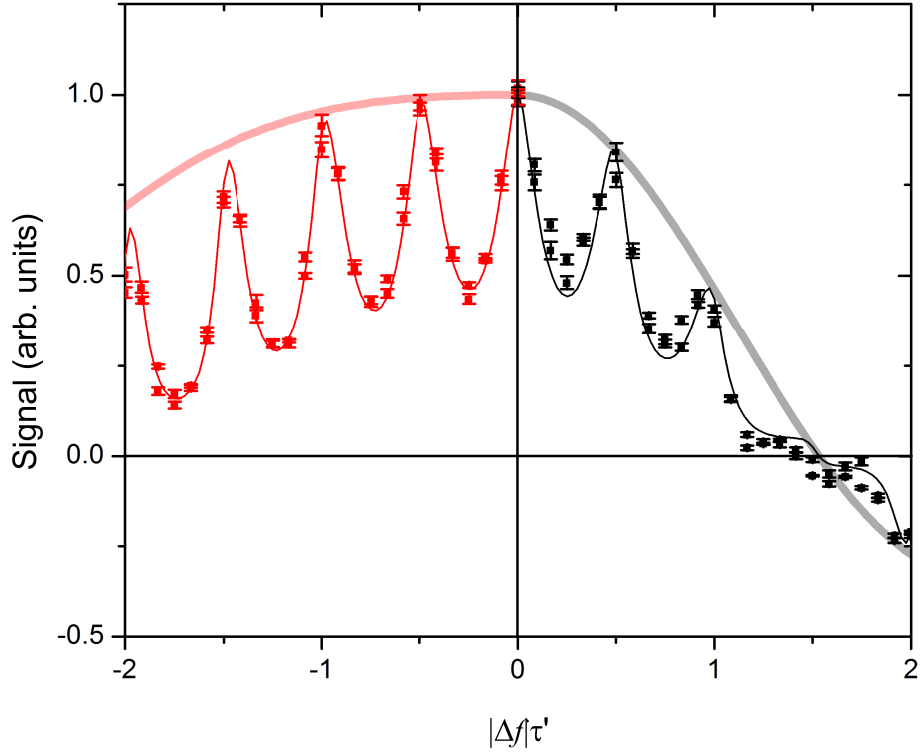


Figure 6.1: The 90-90 SLSE signal on the left (red dots) due a standard sequence has a stronger response as a function of Δf than a nearly identical sequence on the right (black dots). The only difference is that the first free evolution of the left sequence has been adjusted to $\tau_R = \tau - t_0/2$. As discussed below, this reduced free evolution ensures that the density matrix is suitable for pulse spin locking at large off resonances. The thick lines are the predicted signal strengths of the projection model Eq. (6.34), and agree quite well with the data. The thicker shaded lines correspond to the density matrix before application of the repeat unit, given in Eq. (6.50). Data is from the S1 sample of p-chloroaniline, taken at ω_x with $\tau' = 390 \mu\text{s}$, $t_p = 110 \mu\text{s}$, and averaged over 63 ms. Both signals are normalized to the same value, and both sequences are symmetrical about $\Delta f = 0$.

where the secular approximation is used in the last line. The evolution of the density matrix from the excitation pulse with length t_0 is given by Eq. (6.32), with $\hat{n}_0 = \hat{x}_3$, and $\theta\hat{n} = (-\omega_1\hat{x}_2 + \Delta\omega\hat{x}_3)t_0$. The product $\omega_1 t_0$ is chosen in order to be close to 90° for the majority of the crystallites contributing to the signal.[68] In order to isolate the echo train and reduce transient pulse effects, successive experiments in which B is inverted are subtracted.[74] Therefore $\tilde{\varrho}(t_0)$ is effectively

$$\tilde{\varrho}(t_0) = \omega_x \mathbf{I}_x \cdot \frac{\omega_1 t_0}{\theta} \left[\sin \theta \hat{x}_1 - \frac{\Delta\omega t_0}{\theta} (1 - \cos \theta) \hat{x}_2 \right], \quad (6.48)$$

which means that for certain values of θ which occur at large off-resonances the $\mathbf{I}_x \cdot \hat{x}_1$ component of the effective density matrix that produces the locked signal is small, while the $\mathbf{I}_x \cdot \hat{x}_2$ component that does not produce signal is large.

The time between pulses in the echo train is 2τ , or if measured from the center of the pulses $2\tau'$. However, there is some ambiguity in how far the excitation pulse should be separated from the first refocusing pulse. In practice, the midpoint of the excitation pulse to the midpoint of the first refocusing pulse is also set to τ' . This means that the time between the excitation pulse and the refocusing pulse must be reduced to $\tau_R = \tau - t_0/2$. For delta function pulses, or for long values of τ , the difference between τ and τ_R is inconsequential. For short enough values of τ , however, this adjustment provides advantages for large Δf , as shown in Fig. 6.1. To incorporate this τ_R into the theory above only requires a small adjustment to the initial density matrix. This is done by performing a negative rotation after the excitation pulse using the operator

$$\tilde{\varrho}(t_0) \equiv e^{-i\Delta\omega t_0 I_{x3}/2} \tilde{\varrho}(t_0) e^{i\Delta\omega t_0 I_{x3}/2} \quad (6.49)$$

Using again Eq. (6.32), with the rotation in the exponent given by $-\frac{\Delta\omega t_0}{2}\hat{x}_3$, and recognizing that only the I_{x1} component gets locked by series of repeat units, the relevant expression for the density matrix before the first repeat unit is

$$\tilde{\rho}(t_0) = \omega_x \frac{\omega_1 t_0}{\theta} \left[\sin \theta \cos \Theta + \frac{\Delta\omega t_0}{\theta} (1 - \cos \theta) \sin \Theta \right] I_{x1}, \quad (6.50)$$

where $\Theta = \Delta\omega t_0/2$. The coefficient in front of I_{x1} is the c_1 of Eq. (6.44). The excitation pulse is such that for $\Delta f = 0$, $\Theta = 0$, while for increasing values of $|\Delta f|$, Θ increases. In the limit as $|\Theta|$ approaches $\pi/2$ the second term in the square brackets compensates for what would be a loss of signal. This explains why the adjusted sequence produces the stronger signal in those cases since it creates a larger initial signal that can be spin-locked.

6.3 Experimental procedure

The general experimental procedure is given in Chapter 3. Particular to the data in this chapter, experiments were performed on three 100 g powder samples of 98% purity p-chloroaniline $\text{ClC}_6\text{H}_4\text{NH}_2$ from Sigma-Aldrich. These samples were never removed from their glass jars. Initially all three samples had the same FWHM linewidth as the first sample, S1. In order to create samples with a range in broadening due to EFG inhomogeneity the second and third samples, S2 and S3, were melted by submerging their jars in water warmed above 74 C. Once the samples had entirely melted they were allowed to recrystallize. For S2, the heat source of the water was simply turned off and sample and water were allowed to cool slowly. This only increased the linewidth slightly from 117 Hz to 124 Hz, as shown in Table 6.1. After melting S3, its jar was placed in a bath of room temperature water and gently rocked as the sample

recrystallized. Interestingly, an audible cracking noise was observed as the sample solidified. This process greatly increased the linewidth of the sample to from 117 Hz to 190Hz, however, over the course of two weeks the linewidth then fell to 160Hz, where it remained for the duration of data collection. For this reason we distinguish between S3, the sample immediately after recrystallization, and S3*, the sample after the linewidth stopped dropping.

6.4 Results

While our previous work used sodium nitrite NaNO_2 , this project used p-chloroaniline because its nitrogen to hydrogen dipolar coupling was expected to contribute much more to the linewidth than the nitrogen to sodium dipolar coupling of sodium nitrite. This is because the second order broadening $\langle \Delta\omega^2 \rangle^{NK}$ of heteronuclear coupling is proportional to γ_K^4 and falls off faster than the distance separating the nitrogen and the other nuclei raised to the sixth power.[9] Since hydrogen has a gyromagnetic ratio approximately four times the value of sodium,[86] and the nitrogen-sodium bond length in sodium nitrite[87] is approximately 2.5 times the nitrogen-hydrogen bond lengths in the NH_2 group in p-chloroaniline,[85] p-chloroaniline should have much stronger heteronuclear coupling. Also, theoretical calculations had already been made for the second moments of both the homonuclear[73,74] and heteronuclear broadening.[9] And, as previously mentioned, the \hat{x} axes of the PAFs of neighboring nitrogen nuclei are aligned,[9] which simplifies the theoretical work for that transition.

If broadening due to heteronuclear coupling behaves like EFG inhomogeneity, as argued above, then the experimental parameters under which homonuclear dipolar coupling appear for a substance with heteronuclear dipolar coupling should be the same as found in Chapter 4: perform a 90-180 SLSE at $|\Delta f| = \frac{1}{4\tau}$, and for τ greater

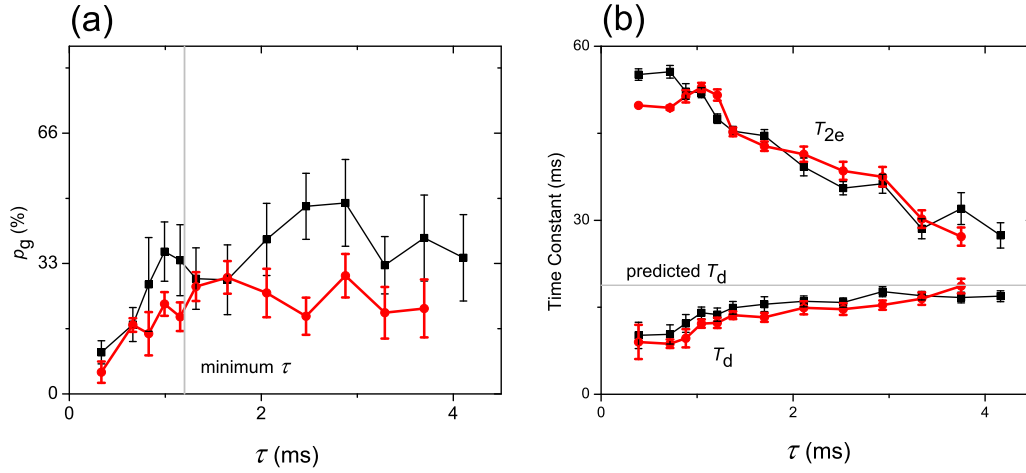


Figure 6.2: The fit parameters obtained from the 90-180 SLSE echo trains using Eq. (4.29) for various τ s at $\Delta f = -1/(4\tau')$ for both S1 (thin black line, squares) and S3 (thick red lines, circles). In (a) the strength of the Gaussian contribution p_g is low for values of τ below the minimum τ where the homonuclear response is predicted to be inhibited, and is consistently higher above that value. In (b) both samples show T_d approach the expected value for a powder 18.8 ms, while also remaining distinct from T_{2e} .

than a minimum τ , $\tau_{min} = \sqrt{t_p/\eta_{eff}}$, with the procedure for calculating the dipolar parameter η_{eff} given in Ref. [74]. For p-chloroaniline, $\eta_{eff}/(2\pi\tau) = 12$ Hz,[74] so the expected time constant due to homonuclear coupling $T_d = 1.16 \cdot \sqrt{3/2}\tau/\eta_{eff} = 18.8$ ms for the powder sample,[73]. This was less than the observed T_1 of 57 ± 10 ms. To see if a homonuclear response in p-chloroaniline could be obtained, a series of 90-180 SLSEs were run both at $\Delta f = 0$ and $\Delta f = \pm \frac{1}{4\tau'}$ for various values of τ , and the echo trains then fit to Eq. (4.29). The results shown in Fig. 6.2 are consistent with the previous observations for sodium nitrite. As τ' increases the Gaussian contribution gets stronger and the value of T_d converges to the expected value of 18.8 ms, regardless of the EFG component of the sample. This is shown for both S1 and S3, with the values for both samples converging to within 10% of the expected value. The values of p_g are somewhat smaller than that observed for sodium nitrite.[73] This is attributed

to the smaller η_{eff} , which is less than half the value for sodium nitrite. In addition, for p-chloroaniline the homonuclear dipolar coupling represents a smaller fraction of the total line broadening, particularly for S3, as shown in Table 6.1.

The expected second moment due to heteronuclear coupling for p-chloroaniline was predicted to be approximately 1kHz by Vega, but the linewidths of the samples were as low as 117 Hz, far less than could be expected from Vega’s prediction. This had been noted before for p-chloroaniline.[88] Vega’s expected broadening was then re-derived assuming the protons were free to move rapidly within a sphere about their location,[85] since the original prediction was based on a purely static model. This motional averaging was found to decrease the expected broadening by orders of magnitude as the sphere of uncertainty increased in size. This suggests that motion is responsible for the narrower than expected line, but since the calculations were only qualitative no prediction of the second moment was made.

The inability to confirm the presence of the heteronuclear coupling from the linewidth alone resulted in uncertainty in declaring that the substance had heteronuclear broadening. However, in principle, one could measure the heteronuclear dipolar coupling after isolating the homonuclear and EFG contributions. In order to do that, the FID lineshapes from all of the samples were independently fit to a Voigt function

$$V(\nu) \propto \int_{-\infty}^{\infty} \exp[-\frac{1}{2}(\frac{x}{\sigma_G})^2] \cdot \frac{1}{(\nu-x)^2 + \gamma_L^2} dx, \quad (6.51)$$

where σ_G is the second moment of the Gaussian component and γ_L is the width associated with the Lorentzian profile. The results of the fits, shown in Table. 6.1, showed that the Gaussian component remained consistent between samples, within 10 Hz, while the Lorentzian components fluctuated on the scale of the observed changes in the linewidth. This suggests that EFG broadening has a Lorentzian behavior,

Table 6.1: The NQR signals from numerous resonant FIDs were averaged together and fit to a Voigt function, Eq. (6.51). This was done on two samples of sodium nitrite (Narrow and Broad) and three samples of p-chloroaniline (S1, S2, S3, and S3*) that varied in only in their broadening due to EFG inhomogeneity. Individually fitting the lineshapes revealed the Gaussian width's agreed within 10 Hz for the same substance and transition frequency. The Lorentzian components, however, varied with the full-width at half maximum linewidths, showing that EFG inhomogeneity manifests itself as a Lorentzian line shape, while the homogenous broadening mechanisms are well represented by a Gaussian lineshape. The results in this table are from fitting corresponding lineshapes simultaneously to the same Gaussian width, with the expected σ_G calculated from the expected broadening due to homogenous dipolar coupling only. The results show p-chloroaniline has an additional source of Gaussian broadening, seemingly due to heteronuclear coupling.

	Sodium Nitrite						P-Chloroaniline			
	ω_x		ω_y		ω_z		ω_x			
	N.	B.	N.	B.	N.	B.	S1	S2	S3	S3*
FWHM ± 2 Hz	178	364	154	289	122	173	117	124	187	161
$\gamma_L \pm 5$ Hz	51	163	37	123	25	61	27	32	73	57
Observed $\sigma_G \pm 5$ Hz	48		46		39		36			
Expected Homonuclear σ_G Hz	44		39		44		17			
Observed/Homonuclear	109%		118%		89%		212%			

since neither of the dipolar coupling broadening mechanisms should vary from sample to sample. As further confirmation, the two samples of sodium nitrite from our previous work were similarly examined. The results from all of the experiments are shown in Table 6.1 and are consistent with the conclusion that EFG broadening has a Lorentzian contribution while the homogenous broadening mechanisms are primarily Gaussian. Since the Gaussian contribution for p-chloroaniline was so much greater than expected from homonuclear dipolar coupling alone, which was not observed for sodium nitrite, we attribute this additional broadening to heteronuclear dipolar coupling.

For a 90-90 SLSE the dominant response should be due to off-resonance behavior. Using the projection model of Eq. (6.34) the 90-90 was modeled for various values of τ' . This produced an expected signal that is independent of broadening mechanisms. To account for the expected broadening due to EFG and heteronuclear dipolar coupling, the known homonuclear response was subtracted in quadrature from the Gaussian component of the observed lineshape for S2. This new distribution, $h(\varpi)$ of Eq. (6.44), was then convolved with the projection model. Using the lineshape data obtained with standard FIDs, however, did not produce a model consistent with the data. Surprisingly it was found that by taking an FID during the SLSE sequence, i.e. performing an FID acquisition immediately after a repeat unit, that the linewidth was narrower from that observed from a single excitation pulse. While this effect is relatively small, it is still significant. This was observed on both S2 and S3* but only after the second repeat unit; the linewidth after the first repeat unit was the same as a normal FID's. Using the lineshape from this SLSE-FID, the projection model predicted the observed signal quite well, as shown in Fig. 6.3, confirming the projection model for the 90-90 SLSE.

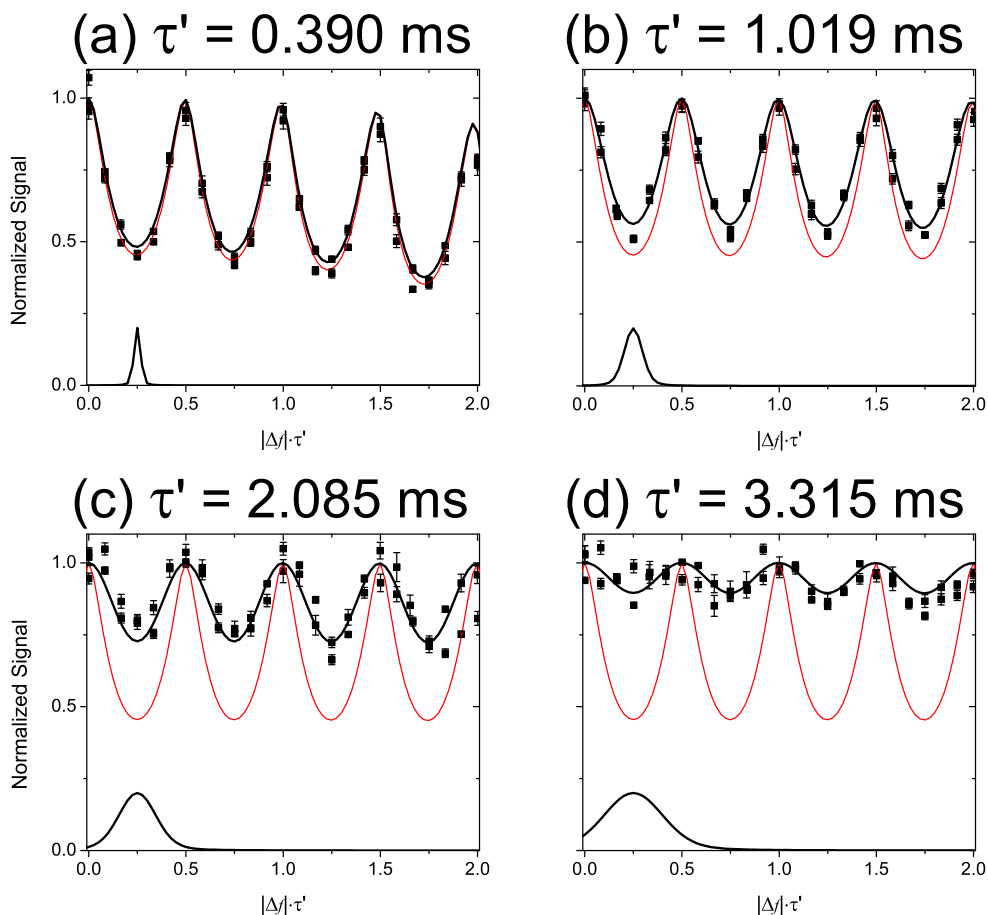


Figure 6.3: The average 90-90 SLSE signals (black squares) obtained from the first 63 ms of echoes, to maximize SNR, from S2 for various values of τ' and for various off-resonances ($\Delta f \cdot \tau'$). Signals were normalized to their respective values at $\Delta f = 0$. The expected contribution to the lineshape due to EFG and heteronuclear broadening is shown by the distribution centered around $\Delta f = 1/(4\tau')$ along the bottom axis. For low values of τ' this distribution in $\Delta f \cdot \tau'$ approaches a delta function, and the model that ignores line broadening behavior (red line) closely tracks the data. At longer τ' , a model incorporating the lineshape, black line, does a better job tracking the data. The linewidth data used here came from FIDs taken during a SLSE sequence, as discussed in the text. For S2 the linewidth narrowed from 124 Hz to 117 Hz; for S3*, from 161 Hz to 136 Hz.

6.5 Conclusion

We have theoretically demonstrated that broadening due to heteronuclear coupling and EFG inhomogeneity have the same response to a pulse sequence. In particular they are both refocused under a 90-180 SLSE sequence. By examining p-chloroaniline we see that the homonuclear response, which was previously addressed in Chapter 4, can still be observed, and at the same conditions observed in the simpler case: use a 90-180 SLSE, $|\Delta f| = \frac{1}{4\tau'}$, and $\tau \geq \sqrt{t_p/\eta_{eff}}$. In order to verify that heteronuclear coupling is present we found that the inhomogeneous broadening of the NQR line due to EFG has a Lorentzian shape, while the homogenous broadening has a Gaussian shape. Since the width of the Gaussian contribution can not be accounted for solely in terms of the homonuclear broadening that we observed, heteronuclear coupling should be the remainder. We note that heteronuclear coupling is much narrower than expected, and we argue that this may be due to the motion of the light hydrogen nuclei in the crystalline environment. The ability to separately determine the contribution of these broadening mechanisms can be used to fingerprint samples, to track their manufacturing origin, and help optimize detection sequences depending on the relative size of these broadening mechanisms.

Chapter 7: Conclusions

The results in this thesis explain the behavior of the NQR signal due to pulsed spin locking as a function of three broadening mechanisms: electric field gradient inhomogeneity, and homonuclear and heteronuclear dipolar coupling. Using simple models, the refocusing behavior of each component is described. Additionally, using a model based on the behavior of just two spins, the experimental conditions to isolate the strength of the homonuclear component were found. This occurs using a 90-180 SLSE sequence, at $\Delta f = 1/(4\tau')$, with the ideal pulse spacing determined partly by the strength of the homonuclear dipolar coupling. All of this is described theoretically and demonstrated experimentally on a number of samples. The conditions which trigger the homonuclear response are to be avoided in substance detection, since the result is a rapidly decaying Gaussian signal. Fortunately the model accurately predicts the conditions where this decay appears, even accounting for subtle differences in the shapes of the rf pulses.

While this homonuclear response is to be avoided in substance detection, due to the correspondingly weak signal, the width of the Gaussian decay was shown to be a measurement of the homonuclear dipolar coupling. This was also verified on several powder samples that varied in the relative strengths of their broadening mechanisms. With the ability to measure homonuclear dipolar coupling, NQR becomes a tool to analyze unknown substances.

Measuring homonuclear dipolar coupling also permits the strengths of the remaining broadening mechanisms to be estimated. With this, NQR is a much more useful tool for substance detection, since the most efficient detection sequence depends on

their relative strengths, as we show. Additionally, the ability to find the contribution of EFG inhomogeneity is important to fingerprint the manufacturing process, which could help trace contraband material back to its supplier.

Appendix A: The solution to $U = e^{i\theta\mathbf{I}\cdot\hat{b}}(\mathbf{I}\cdot\hat{a})e^{-i\theta\mathbf{I}\cdot\hat{b}}$

Given some three dimensional space \hat{x} , \hat{y} , \hat{z} , an angular momentum operator \mathbf{I} , and the general problem of simplifying $U = e^{i\theta\mathbf{I}\cdot\hat{b}}(\mathbf{I}\cdot\hat{a})e^{-i\theta\mathbf{I}\cdot\hat{b}}$, it is useful to start with three simple cases:

$$U = e^{i\theta\mathbf{I}\cdot\hat{x}}(\mathbf{I}\cdot\hat{x})e^{-i\theta\mathbf{I}\cdot\hat{x}} \quad (\text{A.1})$$

$$U = e^{i\theta\mathbf{I}\cdot\hat{y}}(\mathbf{I}\cdot\hat{x})e^{-i\theta\mathbf{I}\cdot\hat{y}} \quad (\text{A.2})$$

$$U = e^{i\theta\mathbf{I}\cdot\hat{z}}(\mathbf{I}\cdot\hat{x})e^{-i\theta\mathbf{I}\cdot\hat{z}} \quad (\text{A.3})$$

The solution to Eq. A.1, $U = e^{i\theta\mathbf{I}\cdot\hat{x}}(\mathbf{I}\cdot\hat{x})e^{-i\theta\mathbf{I}\cdot\hat{x}}$, is obviously just $U = \mathbf{I}\cdot\hat{x}$. The solution to Eq. A.2 is found by first expressing $e^{i\theta I_y}$ as a series

$$e^{i\theta I_y} = \mathbf{1} + i\theta I_y + \frac{1}{2}(i\theta I_y)^2 + \frac{1}{6}(i\theta I_y)^3 + \dots \quad (\text{A.4})$$

where $\mathbf{1}$ is an identity operator. The derivative of $e^{i\theta I_y}$ with respect to θ is

$$de^{i\theta I_y}/d\theta = 0 + iI_y\mathbf{1} + i\theta I_y + \frac{1}{2}iI_y(i\theta I_y)^2 + \dots \quad (\text{A.5})$$

$$= iI_y e^{i\theta I_y}. \quad (\text{A.6})$$

This allows Eq. A.2 to be expressed as

$$dU/d\theta = ie^{i\theta I_y}[I_y I_x - I_x I_y]e^{-i\theta I_y} \quad (\text{A.7})$$

$$= e^{i\theta I_y} I_z e^{-i\theta I_y}. \quad (\text{A.8})$$

Repeating the process

$$d^2U/d\theta^2 = ie^{i\theta I_y}[I_y I_z - I_z I_y]e^{-i\theta I_y} \quad (\text{A.9})$$

$$= -e^{i\theta I_y} I_x e^{-i\theta I_y} \quad (\text{A.10})$$

$$= -U. \quad (\text{A.11})$$

But the expression $d^2U/d\theta^2 = -U$ is a familiar second order differential equation with solution

$$U = A \cos \theta + B \sin \theta. \quad (\text{A.12})$$

Since $U(\theta = 0) = I_x$, $A = I_x$. Similarly, since $dU(\theta = 0)/d\theta = I_z$, $B = I_z$ and

$$U = e^{i\theta I_y} I_x e^{-i\theta I_y} \quad (\text{A.13})$$

$$= I_x \cos \theta + I_z \sin \theta \quad (\text{A.14})$$

Similarly Eq. A.3 can be shown to be

$$U = e^{i\theta I_z} I_x e^{-i\theta I_z} \quad (\text{A.15})$$

$$= I_x \cos \theta - I_y \sin \theta \quad (\text{A.16})$$

with cyclic permutations of x, y, z providing all the other cases.

For the general case $U = e^{i\theta \mathbf{I} \cdot \hat{b}} (\mathbf{I} \cdot \hat{a}) e^{-i\theta \mathbf{I} \cdot \hat{b}}$ we define a new, primed, orthogonal coordinate system $\hat{x}', \hat{y}', \hat{z}'$, related to the original frame by some rotation such that $\hat{x}' = \hat{b}$. This coordinate system defines a new set of operators $\mathbf{I} = [I'_x, I'_y, I'_z]$, which must commute like angular momentum operators. The new operators allow the equation to be rewritten:

$$e^{i\theta \mathbf{I} \cdot \hat{x}'} (\mathbf{I} \cdot \hat{a}) e^{-i\theta \mathbf{I} \cdot \hat{x}'} = e^{i\theta \mathbf{I} \cdot \hat{x}'} [\hat{a} \cdot \hat{x}' I'_x + \hat{a} \cdot \hat{y}' I'_y + \hat{a} \cdot \hat{z}' I'_z] e^{-i\theta \mathbf{I} \cdot \hat{x}'} \quad (\text{A.17})$$

From above, this has the known solution

$$\hat{a} \cdot \hat{x}' I'_x + \hat{a} \cdot \hat{y}' (I'_y \cos \theta - I'_z \sin \theta) + \hat{a} \cdot \hat{z}' (I'_z \cos \theta + I'_y \sin \theta), \quad (\text{A.18})$$

which is the same as

$$\mathbf{I} \cdot [\cos \theta \hat{a} + (1 - \cos \theta) \hat{b} (\hat{b} \cdot \hat{a}) + \sin \theta (\hat{a} \times \hat{b})]. \quad (\text{A.19})$$

The result is the same as dotting \mathbf{I} with \hat{a}' , which is \hat{a} after being rotated by an angle θ about \hat{b} with a clockwise rotation.[89] This is clearly consistent with the particular solutions for Eqs. A.14-A.16.

Appendix B: The FID processing procedure

For samples with a long enough T_2^* the single pulse FID sequence provides an easily obtained NQR signal that is useful both for basic analysis and as a diagnostic tool for the system. For the research described in this thesis, four variables were commonly generated from FID sequences: ω_{NQR} , the phase of the FID, linewidth, and the back projected intercept.

A visual representation of how ω_{NQR} and the FID's phase are found is presented in Fig. B.1. It starts with the spectrometer's output which is a set of complex numbers $x[n]$. These are the quadrature detection representation of the voltage from the detector coil, sampled discretely with a dwell time T_{dwell} . For electronics reasons there may be a baseline offset to $x[n]$ that artificially and uniformly increases each value. To remove any potential baseline from the FID the average values of the real and imaginary components of the last $1/8^{th}$ of the data are subtracted from each $x[n]$. Since the typical FID was 1024 points of data, with $T_{dwell} = 10 \mu s$, and because the typical FID decay constant T_2^* could be on the order of 2 ms or less, the signal has decayed to about 1% of the initial value by $7/8^{th}$ s of 10.24 ms. Therefore removing the baseline offset shouldn't have removed any of the desired signal.

The sequence is then shifted to the left by the number of points necessary to remove any ringing or data collection artifacts. This removed the early data from all further analysis. The undesirable points were typically obvious from visual analysis of the signal, given a sufficiently high SNR. Match filtering is then applied by multiplying each data point by an exponential function with a decay constant given by the linewidth FWHM of the sample measured previously:

$$x[n] = e^{-\pi \cdot FWHM \cdot n \cdot T_{dwell}} \quad (\text{B.1})$$

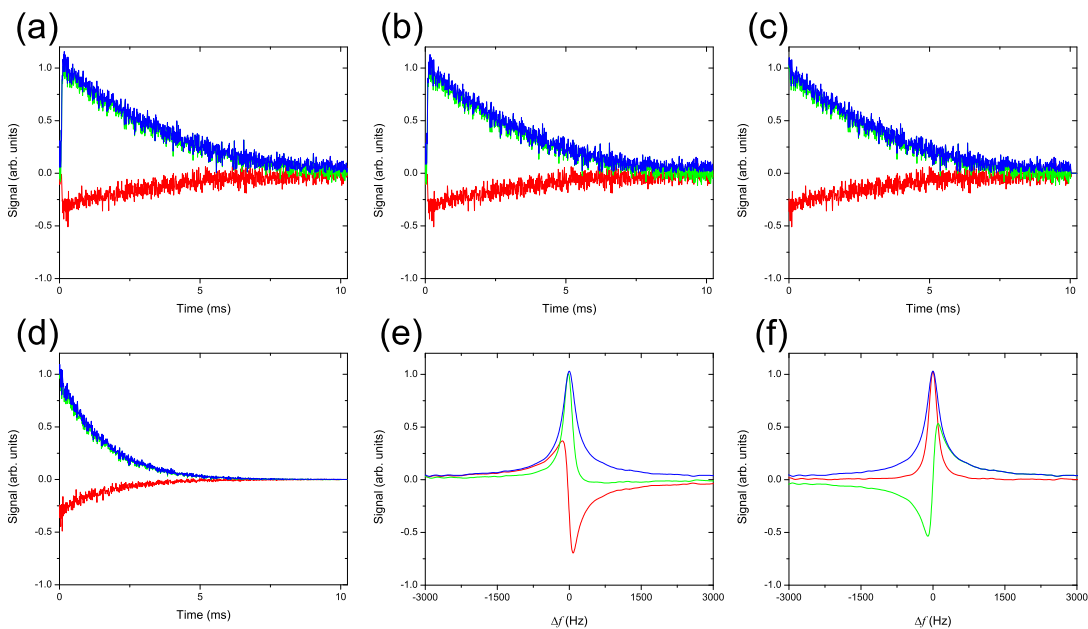


Figure B.1: A visualization of the typical FID processing necessary to calculate the off-resonance and the phase of the signal, where red corresponds to the real component of the signal, green to the imaginary, and blue to the magnitude. The raw FID data (a) has some acquisition artifacts, perhaps due to probe ringing. The baseline offset calculated from the last 1/8th of data, however, must be removed (b) from each component before addressing this early data. For this example, removing the baseline offset decreased the peak magnitude by almost 3%. Once the baseline is removed, the early data is then removed (c) by a left-shift; in this case it is the first 20 points. The signal is then match filtered (d) using a linewidth of 120 Hz. The fast Fourier transform of the remaining signal (e) has a peak magnitude at $\Delta f = 0$, which means the signal was acquired on resonance. The change in phase necessary to make the peaks of the real component and magnitude occur at the same Δf (f) determines the phase of the signal. Data is from sample S1 of p-chloroaniline and obtained at ω_x . The excitation pulse width was 110 μs .

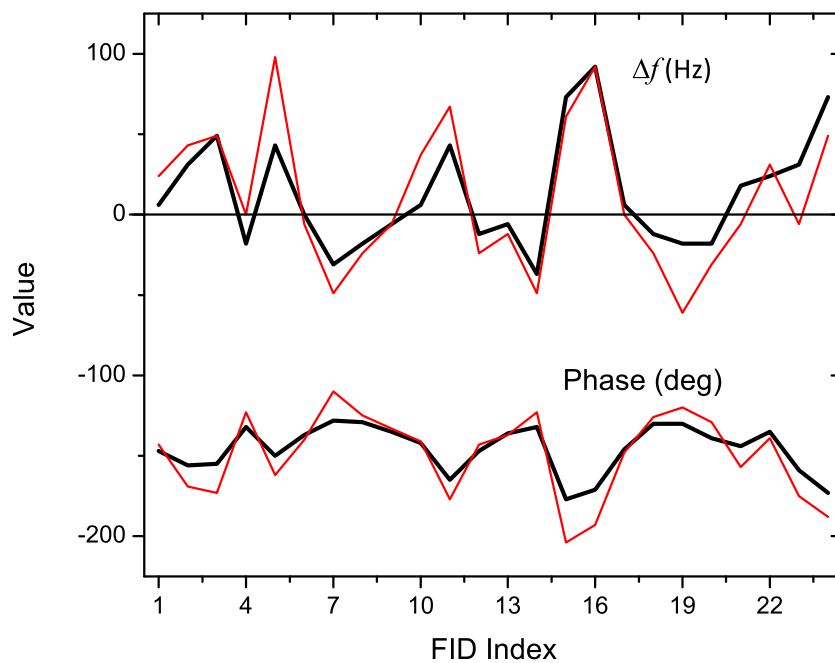


Figure B.2: Calculations of Δf and the FID's phase made using match filtering (thick black lines) show less variation than the same calculations performed without match filtering (thin red lines). This is quantified by comparing the standard deviations in each measurement. For Δf it is 35 vs 44 Hz, in favor of match filtering; for phase it is 15 vs 26 degrees, again favoring match filtering. The data used here was from a series of identical FID sequences performed on the broad sample of sodium nitrite at ω_z since this was the most difficult data to process.

This effectively weights each data point by the expected signal response, and leads to a higher SNR and more consistent measurements of the desired values, as shown in Fig. B.2. A large number of data points are then appended to $x[n]$ that consist of zeros. This zero-filling artificially increases the acquisition time of the experiment, permitting finer measurements of ω_{NQR} . Typically $x[n]$ was zero-filled to a length of 16384 points. Zero-filling is justified because the signal should be effectively zero by the 1024th data point, as already argued above. The data is then Fourier transformed with a discrete fast Fourier transform FFT to create $X[\nu]$. The peak of the signal in the frequency domain corresponds to the off-resonance of the signal. This is then added to the observation frequency of the sequence to determine the NQR frequency, with an accuracy around ± 12 Hz or better. The phase adjustment necessary to make peak of the real part of $X[\nu]$ equal to the peak of the magnitude of $X[\nu]$, is called the phase of the signal. These are typically compared to the phase of the signal when $\Delta f = 0$, which acts as a reference phase.

As shown in Fig. B.3, the procedure to obtain the FID linewidth is similar: remove baseline, left shift data, zero fill, Fourier transform and phase to the previously determined value. The resulting real component provides the lineshape of the signal and is used to calculate the full-width at the half-maximum FWHM. As an intermediate step in this process, the first 40-80 points of clean data are plotted against time with $t=0$ corresponding to the end of the pulse. These point are then fit to a straight line in order to calculate the value at $t = 0$. This is the back projected intercept, which is useful for calculating normalization coefficients of the signal. Additionally, changes in the back projected intercept would be proof of a dramatic change in the strength of the pulses, so this also helps track the consistency of the electronics.

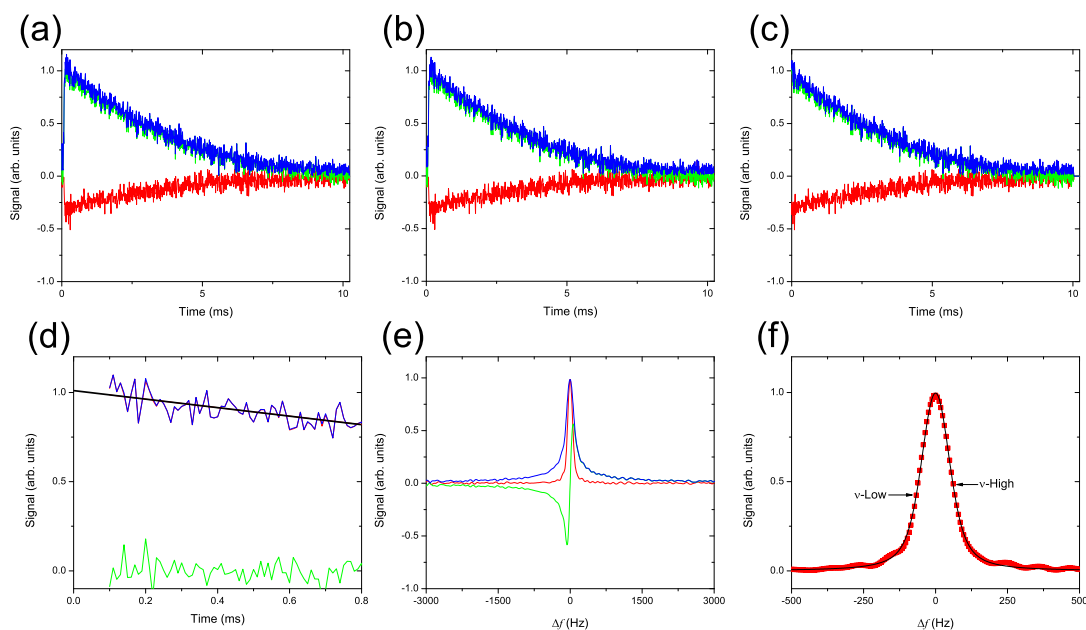


Figure B.3: A visualization of the FID processing used to obtain the back projected intercept and lineshape, where red corresponds to the real component of the signal, green to the imaginary, and blue to the magnitude. As in Fig. B.1, in (a) the raw FID signal still contains artifacts. However, baseline correcting must be performed (b) before the early time data can be dropped (c). After phasing to the previously calculated value, the first ~ 80 points of clean data are then plotted against the time from the end of the pulse (d). These points are then fit with a straight line to find the back projected intercept, useful for normalizing signals and tracking the strength of the pulses. After zero-filling the data from (c) the signal is Fourier transformed (e). The real component of the Fourier transform provides the lineshape of the signal (f), which can be processed to find the full-width at the half-maximum FWHM.

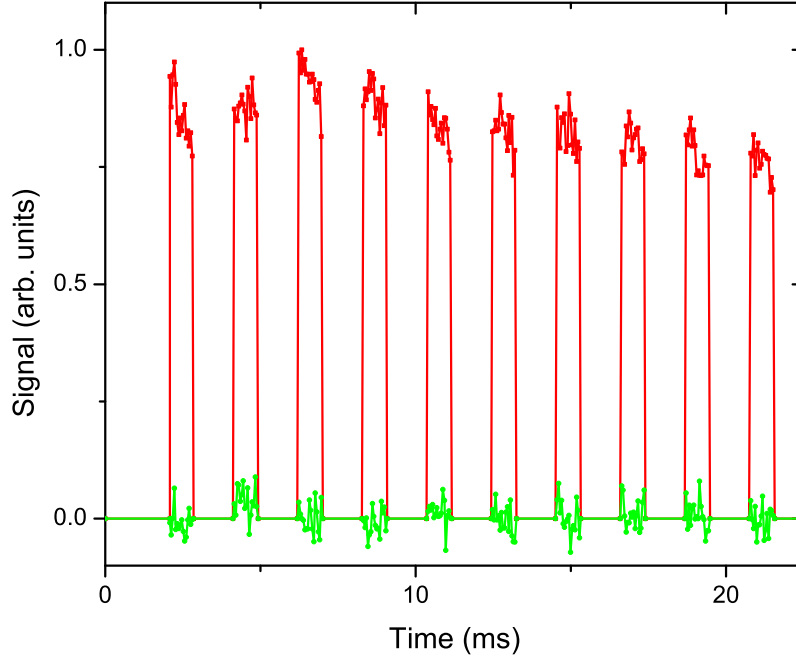


Figure C.1: A representative view of the first 10 echoes acquired during a SLSE sequence. Only the 16 clean data points are shown for each echo which are separated in time by $2 \cdot \tau'$. Data is from the Narrow sample with a 90-90 SLSE with $\tau' = 1.04ms$ at ω_x

Appendix C: The SLSE processing procedure

To make the signal processing consistent for the many values of τ , the SLSE sequences were built around the data acquisition. For processing reasons, 22 data points, each of duration T_{dwell} , were collected for each echo. The first and the last five data points were dropped, because they were questionable. This left 16 clean data points for each echo, such as those shown in Fig. C.1. The rest of the SLSE timing was built around ensuring that time τ after the refocusing pulse was also the midpoint of the first clean data point in the echo acquisition. With this configuration a larger τ was obtained by increasing T_{dwell} , and then adjusting the rest of the sequence parameters as needed.

Values of T_{dwell} used in this thesis varied from 16 μs to 180 μs .

The number of echoes acquired was always enough to ensure that at least 1.25 times the maximum expected T_{2e} of data was acquired in time. This would present the largest SNR for the average echo signals for an exponential signal.

A marked baseline was found in some of the SLSE data. Because of this a second set of noise only data was accumulated after the signal. This was used to identify any potential baseline which would then be subtracted from the SLSE signal.

The SLSE's were processed for two different signals: the average echo signal and the echo train. The average echo was the sum of the first N clean echoes, where N was the number of echoes acquired in $1.25 \cdot T_{2e}$, to maximize SNR. The summed signal was then zero-filled out to 256 points, Fourier transformed, and phased to a reference phase. The reference phase was the phase necessary to make the peak of the real signal match the peak of the magnitude of the signal when $\Delta f = 0$. Also, a note was made of the location in the frequency domain where the peak average echo signal occurred. This was necessary for the echo train analysis.

To analyze the echo trains, each individual echo of clean data was zero-filled to 256 points, Fourier transformed, and then phased to the same reference phase used to process the average echo signals. The real component from each echo was then sampled at the location in the frequency domain obtained by processing the average echo signal. Using the expected off-resonance from the FID would have been more accurate, but computationally it was easier to exploit the average echo signal. Each echo signal could then be plotted against time, separated by $2 \cdot \tau'$, and processed as desired.

Appendix D: A Low Power NQR System

D.1 Overview

Over November and December of 2012 I was invited to work as a guest researcher with a group at Osaka University led by Dr. Hideo Itozaki. While my research is in the physics of NQR signal creation, Dr. Itozaki's lab focused on the electronics of NQR signal detection. While at his lab I assembled the components of a custom NQR system, from the signal generator to the spectrometer. This system had very low power requirements and cost compared to the equipment in use at Dr. Sauer's lab at George Mason University. All of the other experiments described in this thesis could easily have been performed using such a simple and cheap system as we developed at Osaka University. The following report summarizes my work in Dr. Itozaki's lab.

D.2 Abstract

We describe a complete, portable, low power, low cost NQR system. While a typical NQR system is impedance matched to 50Ω , our system is based around an efficient, low power, class-D amplifier with an output impedance in the single Ω region. We demonstrate the ability to use this system to perform basic NQR experiments and measure the peak instantaneous power requirements to be a little over 10 W.

D.3 Introduction

As shown in Fig. D.1, a typical NQR system consists of a five parts: there is the signal generator to create the rf excitation pulse; an amplifier (1 kW common) to

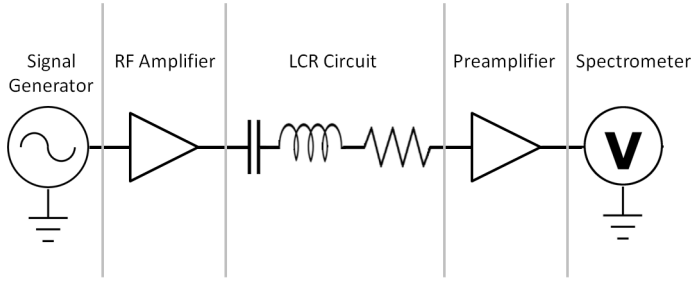
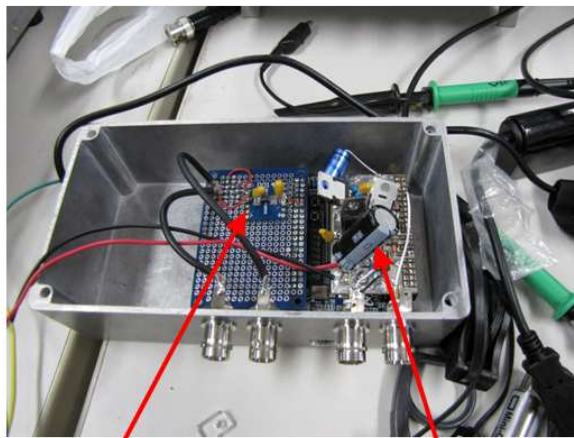


Figure D.1: An overview of a typical NQR system.

give the pulses enough power; a resonant LCR circuit tuned near ω_{NQR} , with the inductor serving to both create the initial magnetic field and collect the resulting signal; and preamplifiers to make the signal large enough for the spectrometer. Typically, components of an NQR system in a laboratory are impedance matched to 50Ω . Impedance matching makes the transfer of power from the amplifier to the main coil more efficient.[90] However, the power requirements of the amplifier are proportional to its output impedance, for a given I . By reducing the output impedance of the amplifier to a few Ω , and matching the rest of the system to that lower value, the power requirements of the amplifier, and therefore the entire system, can be reduced significantly.

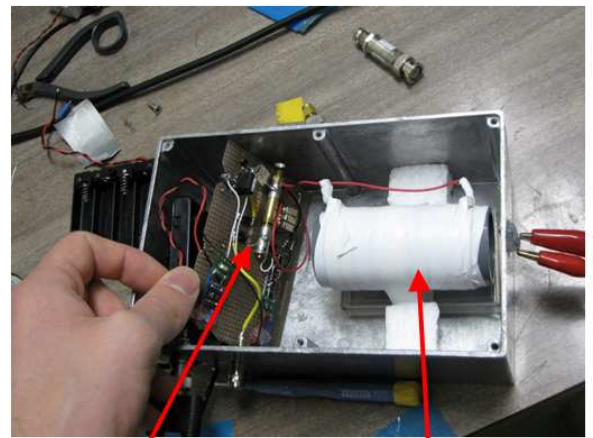
D.4 The system in detail

The heart of our system was a field programmable gate array (FPGA) from the Altera Corporation: the DE0-Nano development board. The FPGA generated the rf pulse, sequenced the MOSFETs in the probe, controlled the analog to digital (A2D) converter, and performed the signal analysis. Unlike the sinusoidal rf signal generated by the more common Tecmag spectrometer, the signal from the FPGA was simply a series of step functions. This signal was fed into a class-D amplifier designed around a Texas Instrument LM5101A high voltage gate driver. A class-D amplifier was used



A2D

Class D Amp.



LCR Circuit

Main Coil

Figure D.2: The image on the left shows the shielded processing box holding the A2D, the class-D amplifier, and the FPGA located directly under the amplifier. Room has been left for a battery source on the left side of the box. The various BNC connections are for connecting this processing box to the probe box, shown on the right. The main coil of the probe box, which holds the sample, has been wrapped in Teflon tape to eliminate arcing. On the right of the probe box the output terminals of the sniffer probe are seen connected to a pair of alligator clips.

specifically because of its efficiency and low output impedance. The amplifier used a voltage source of 12 to 24 V, typically provided by low noise batteries, to increase the rf signal's peak to peak voltage to that of the voltage source.

The entire circuitry, shown in Fig. D.3A, was designed to isolate the probe portion during excitation, as shown in Fig. D.3B. This ensured power went into generating the field and not into damaging the preamplifiers. The isolation was made possible because the transmit receive (T/R) switches and the MOSFETs acted as open circuits when exposed to the high voltage of the pulse. Another benefit of isolation was to obtain a high Q during the pulse, since no purely resistive elements were left in the circuit, which kept the power requirements of the amplifier low.

Two methods were used to determine the Q of the probe during excitation. The first was to find the voltage amplification of the probe. When a resonant pulse with an amplitude of 12 V was applied to the probe, the amplitude of the voltage across the inductor was approximately 1 kV, which was measured directly. This amplification factor of 83 is one estimate of the Q .

A second estimate of Q was found by analyzing the rise and fall times of the excitation pulse. These were obtained by measuring the actual pulse shapes using a single loop of wire, with terminals outside the probe box, placed adjacent to the main coil. Due to inductive coupling, a voltage was induced on this sniffer coil that was proportional to the magnetic field strength of the main coil. The observed rise and fall times provide an estimate of Q through the equation

$$Q = \pi \cdot f \cdot t_c \tag{D.1}$$

where f is the frequency of the pulse, and t_c is pulse's rise or fall time constant. The time constants were found by fitting the pulse shapes to the functions $Pulse(t) =$

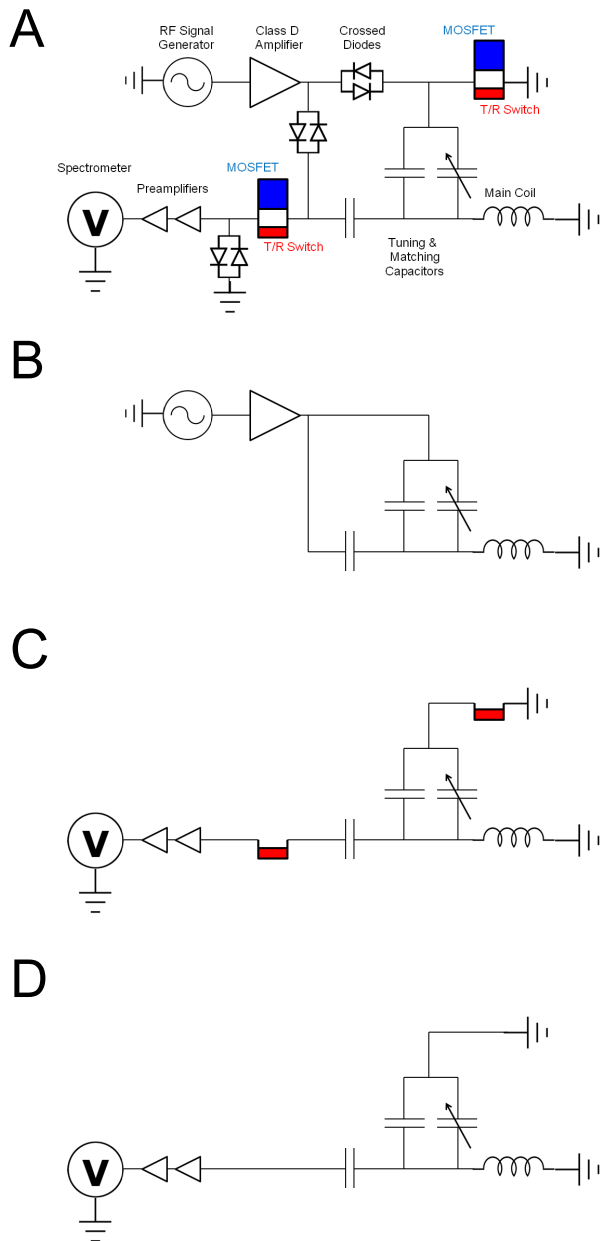


Figure D.3: A schematic of the main components of the circuitry is shown in A. The effective circuit of the high Q excitation configuration is shown in B. Here the high resistance of the T/R switch and MOSFETs isolates and protects parts of the full circuit by removing the path to ground. The effective circuit of the low Q recovery configuration, when the remaining pulse energy is quickly removed from the system, is shown in C. This is facilitated by the T/R switches providing a finite resistance to ground. Finally, the effective circuit of the high Q reception configuration is shown in D. The MOSFETs are triggered to provide a low resistance path to ground, increasing the Q substantially.

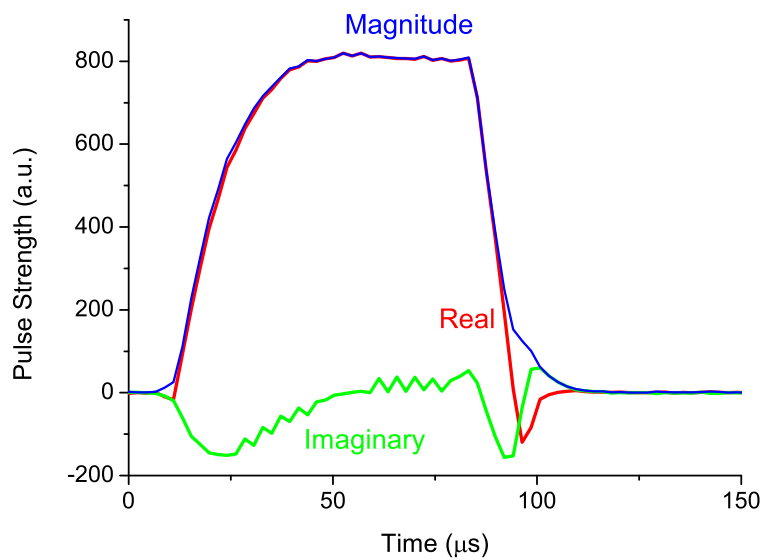


Figure D.4: The excitation pulse of the class-D amplifier observed using the sniffer coil reveals a difference in the rise ($10.6 \pm 1.1 \mu s$) and fall ($6.3 \pm 0.1 \mu s$) times. The different time constants show that the Q changes when the pulse stops, which helps to rapidly remove the energy from the coil and increase signal acquisition time. The complex analysis of the pulse shape reveals a more complete picture than looking at the magnitude alone, since the presence of the non-zero imaginary component during excitation is responsible for certain signal behaviors observed in other systems.[73]

$A(1 - e^{-t/t_{rise}})$ for the rise, and $Pulse(t) = Ae^{-t/t_{fall}}$ for the fall, where A is the pulse amplitude. Analyzing the excitation pulse shape in Fig. D.4 reveals a change in Q from 45 for the rise to 25 for the fall. This change in Q occurred passively and by design. Remaining in a high Q configuration after the pulse would create ringing as the system slowly removed the pulse energy. This ringing signal, with its initially high voltage, would obscure the NQR signal, and reduce the observation time of the already weak and decaying signal. Designing the circuit to enter the configuration shown in Fig. D.3C lowers the Q and reduces the ringing signal after the pulse. We note that the Q based on rise time disagrees with the value based on amplification. This is probably due to the non-linearity of the MOSFETs and the T/R switches making Q change as the pulse is applied. So while the Q observed through the time constants is less accurate, its calculation is useful to show that Q decreased after the pulse.

Once the ringing has fallen below a safe threshold, the MOSFETs are switched into a low resistance state by the FPGA. This puts the probe into the high Q configuration shown in Fig. D.3D. In this state, there are no significantly resistive elements left in the circuit. This is achieved with the virtual short from the probe to the first preamplifier, shown in Fig. D.6, which results from grounding the non-inverting pin of the preamplifier, via a $1\ \mu\text{F}$ capacitor, and connecting the inverting pin to the probe. The virtual short results in a very low input impedance between the coil and the first amplifier, at 1.37 MHz, and an efficient transfer of power. The difference in the Q between the recovery and reception configurations is found in Fig. D.5 by comparing signals observed by the probe, due to a known input, in the two configurations.

While the gain of the first preamplifier was measured to be approximately 40 dB, a second preamplifier was used to increase the signal even further before measurement by the A2D. Several different configurations were tested for the second preamplifier.

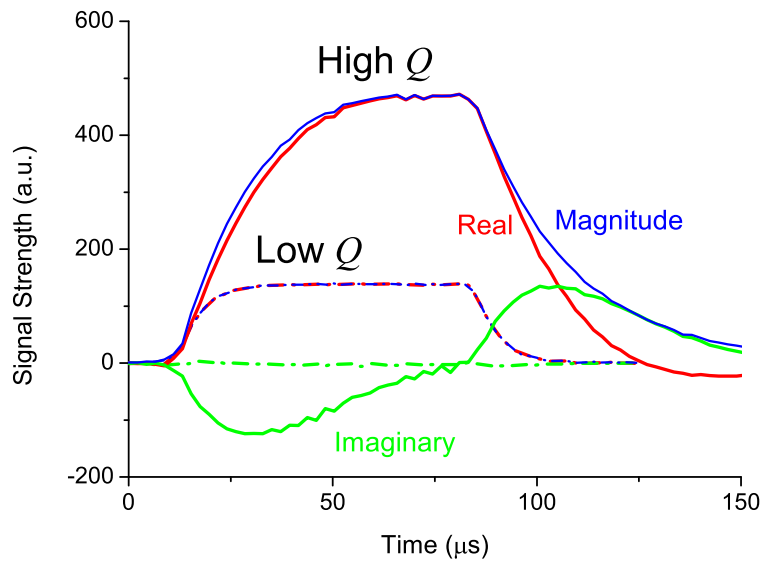


Figure D.5: Signals obtained by toggling the MOSFETs into the low Q (dashed) and high Q (solid) configuration, as described in Fig. D.3, demonstrate the Q switching is working. The signals were created by applying a square pulse to the sniffer coil which induced a voltage in the main coil that was detected with the NQR system. The results show a nearly 3.5 times increase in the observed signal strength for the same input in the high Q configuration. The fall times of the two signals estimate the Q to be approximately 100 for the high Q configuration, and 25 for the low Q configuration: consistent with the Q observed during the fall of the excitation pulse.

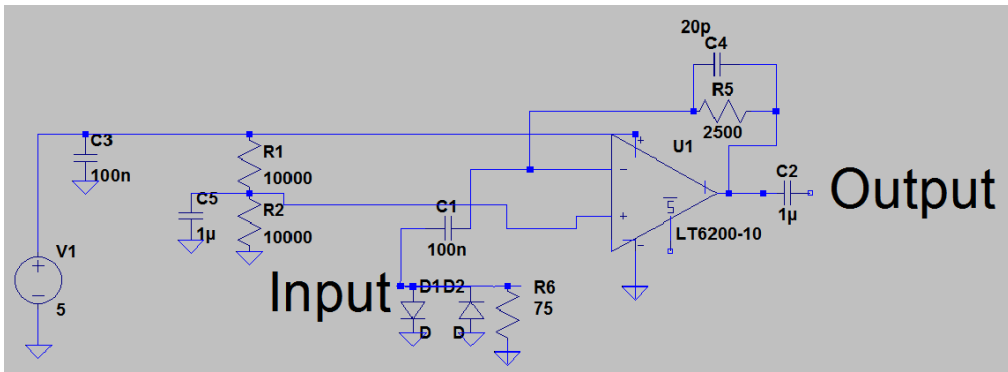


Figure D.6: The circuit diagram of the first preamplifier, showing the virtual short for the input terminal.

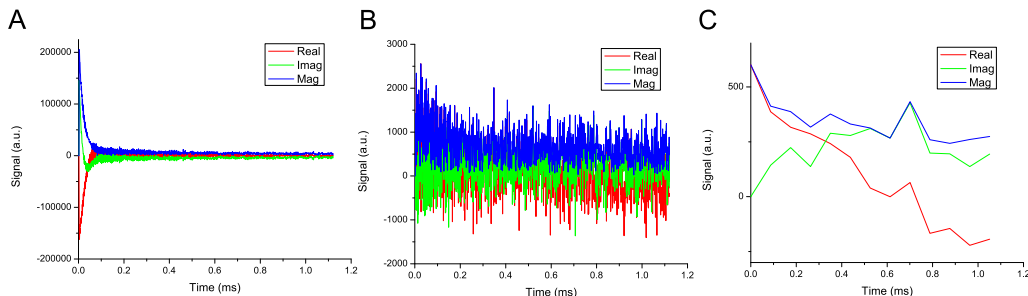


Figure D.7: Three representative signals obtained with the system obtained after a single excitation pulse. In A the initial ringing from the probe is much larger than any other feature observed in the signal, showing that acquisition has been started too soon. In B the data acquisition has been started after the ringing has finished, and reveals the exponential decay associated with the NQR signal. Finally, C shows the same data as B, except neighboring points have been averaged to remove high frequency noise. The real and imaginary lines cross, since the sequence was not taken exactly at $\Delta f = 0$.

The best performance was found with it designed around the same integrated circuit as the first, but with an input impedance of 50Ω and a low output impedance. The output of the second preamplifier was connected to the A2D, which had an input impedance of 50Ω . The output of the A2D was analyzed using quadrature detection by the FPGA with the results sent to a laptop for further processing.

D.5 Experimental details and observations

A 40 g powder sample of imidazole, $C_3H_4N_2$, was used to obtain NQR signals, such as shown in Fig. D.7, to verify the systems functionality. Imidazole was chosen because its 1.37 MHz line is a good substitute for the 1.22 MHz line of the real target substance: methamphetamine hydrochloride, $C_{10}H_{15}N$. The signal for various θ s should form a characteristic signal response if the signal is a real NQR signal.[68] The set of signals shown in Fig. D.8 was obtained by holding the intensity of the pulses constant and varying t_{pw} . For the imidazole sample, the resulting curve shows the gross features of the expected curve, with the difference attributed to the large filling factor of the

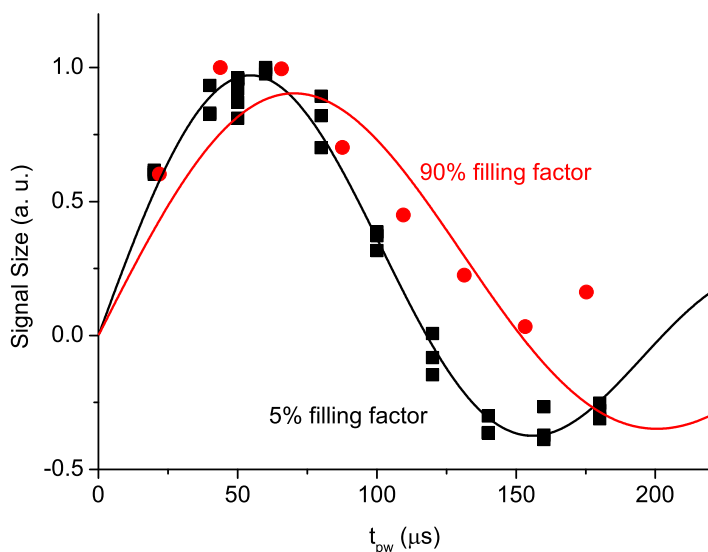


Figure D.8: A comparison of calibration curves for two different filling factors: the ratio of sample volume to main coil volume. Filling factor provides a qualitative measure of the inhomogeneity of the applied field strength over the sample, i.e. a smaller filling factor results in a more homogenous field over the sample than for a large filling factor. Because of the larger field homogeneity, the experiment with the smaller filling factor fits the expected functional form better than the experiment with the larger filling factor. However, the general behavior of the NQR calibration curve is still observed with the larger filling factor. Data from the small filling factor sample were obtained from a 100 g sample of p-chloroaniline in a conventional NQR system. Data from the large filling factor sample came from the sample of imidazole and NQR system described in this appendix.

sample resulting in an inhomogeneity in B across the sample. Therefore, instead of a single calibration curve, the net response is the sum of several calibration curves. The result suggests that an inhomogeneous field may be better for a detection, since not all of the substance can produce a minimum signal, but more work must be done on this topic. The data is the summation of 50 repetitions for a given pulse length, with no phase cycling between scans to remove noise, as is usually done. We note one surprising way to increase the SNR of this system was to ensure that the laptop powering the USB connection to the FPGA was under battery power. It was clearly seen in the output of the preamplifiers that the signal was much noisier with the laptop under AC power than under battery power.

Finally, we measured the power requirements of the system by observing the voltage drop across a 0.1Ω resistor temporarily put in series with the output of the amplifier during pulsing. The voltage drop observed was 0.370 mV peak to peak, corresponding to a peak instantaneous current across the resistor of 1.85 A . Since the amplitude of the corresponding pulse was 6 V , the peak instantaneous power of the system was 11.1 W . Knowing the peak power, we can estimate the resistance of the NQR system during pulsing. Starting with $P = V^2/R$, we get $R = 36 \text{ V}^2/11.1 \text{ W} = 3.2 \Omega$. This is consistent with another approximation to measure R , $R = \omega_{rf}L/Q$, where L is the inductance of the main coil. Using the measured value of $L = 31 \mu\text{H}$, and $Q = 83$, this method also gives a value for $R = 3.2 \Omega$ for the excitation pulse.

D.6 Conclusion

We have demonstrated the creation of a complete NQR system optimized for low power requirements. We have shown that its results are comparable to that performed with a high power NQR system, for single shot experiments. The results suggest that

an inhomogeneous field might be advantageous for substance detection, since the signal behavior is not dominated by a single response. The power requirements are achieved using the low output impedance of a class-D amplifier, which resonantly drives an LCR circuit with an input impedance around 3Ω . The power requirements are quite low, on the order of 10 W, compared to the kW power requirements of some NQR systems. The system is small, occupying less than 2 liters, and quite affordable. Additional electronics work is to demonstrate multipulse experiments and improve the software control of the system.

Appendix E: Example Visual Basic Script for Tecmag Automation

E.1 Overview

Automating the Tecmag with Visual Basic Script (VBS) required numerous tricks to make it work nicely. To aid others hoping to use this time saver, the following example script is provided. This particular code was used to run a series of FID sequences with the various pulse lengths specified in the “pws” array. The code begins with the required VBScript-NMRScript Header for the script to interface with the Tecmag unit. Note that an open .tnt file is required for all VBS scripts to run. After the header, a set of user defined variables is created. A set of template .tnt files are then created, which are updated with the user defined variables and saved in the experimental folder.

With the templates defined, the resonance frequency of the sample is found. The FID processing necessary to find the resonance frequency is found by invoking a Java program. The java program is designed to output the resonance frequency to a text file, which is then read by the script. The call to Java and the reading of the text file are contained in the function “getFIDresFreq()” at the bottom of the code. It is a convoluted method, but it worked very well.

Each program that is run is limited to the name “current.tnt”. This kept the number of files open at any time to a minimum, something the Tecmag software seemed to appreciate. By carefully opening and closing files, any problems with the number of files open was kept to a minimum.

Also, there are many “WScript.Sleep wait” or “WScript.Sleep 100” commands. These are to intentionally slow down the program to ensure the previous command

is executed before the next command is processed.

```
1
2 '#####'
3 ' * VBScript-NMRScript Header, v2-020716'
4 ' *'
5 ' * use "App.CommandName" to communicate'
6 ' *'   with the Application Object
7 ' * use 'Data.CommandName' to communicate'
8 ' *   with the topmost data file (Document Object)'
9
10 Dim App, Data, pathToDoc
11 Set App = GetObject(, "NTNMR.Application")
12 pathToDoc = App.GetActiveDocPath
13 If pathToDoc="" Then
14     MsgBox "Script requires an open data file !",_
15         vbOKOnly + vbCritical, "NMRScript"
16     WScript.Quit() 'exit immediately'
17 End If
18 Set Data = GetObject(pathToDoc)
19 '#####'
20
21 amp90      = 11.3
22 pw90      = "110u"
23 amp180     = 27
24 freqGuess = 2.768
25 fidRD     = "50u"
26 fidAD     = "50u"
27 scans1D   = 64
28 points2D  = 3
29 recGain   = 100
30 tDw       = "10u"
31 FIDpts    = 1024
32 delay     = "500m"
33
34 Running   = 1
35 wait     = 200
36
```

```

37     tmpPath = "C:\malone\paper2\templates\"
38     fidPath = "C:\malone\javaOnly\data\"
39     expPath = "C:\malone\paper2\tuningY\timeCal\"
40     pws     = Array("50u","20u","60u","100u","140u","180u","50u")
41     exps    = Ubound(pws)
42
43     '#####'
44     '#####'
45
46     '**---Create templates---**'
47     Data.OpenFile tmpPath &"FID_template.tnt"
48     Data.SaveAs   expPath &"FID_temp.tnt"
49     App.CloseFile tmpPath &"FID_template.tnt"
50
51     Set Data = GetObject(App.GetActiveDocPath)
52
53     Data.SetNMRParameter "f1_amplitude"    ,amp180
54     Data.SetNMRParameter "pulseWidth"     ,pw90
55     Data.SetNMRParameter "Observe Freq."  ,freqGuess
56     Data.SetNMRParameter "Scans 1D"      ,scans1d
57     Data.SetNMRParameter "Points 2D"     ,points2D
58     Data.SetNMRParameter "RD"            ,fidRD
59     Data.SetNMRParameter "AD"            ,fidAD
60     Data.SetNMRParameter "Receiver Gain" ,recGain
61     Data.SetNMRParameter "Dwell Time"    ,tDw
62     Data.SetNMRParameter "Acq. Points"   ,FIDpts
63     Data.SetNMRParameter "delay"         ,delay
64     App.Save
65
66
67     '#####'
68     '#####'
69
70     '**---Run FID to find resonance frequency---**'
71     Data.OpenFile expPath &"FID_temp.tnt": WScript.Sleep wait
72     Data.SaveAs   expPath &"current.tnt":   WScript.Sleep wait
73     App.CloseFile expPath &"FID_temp.tnt": WScript.Sleep wait
74     Set Data = GetObject(App.GetActiveDocPath): WScript.Sleep wait

```

```

75
76     Data.SetNMRParameter "f1_amplitude" ,amp90
77     Data.SetNMRParameter "Observe Freq." ,freqGuess
78     Data.SetNMRParameter "Points 2D" ,1
79
80         runAndSave()
81
82     '**---Calculate resonace frequency using java---**'
83     deleteFiles()
84     Data.SaveAs fidPath &"FID.tnt": WScript.Sleep wait
85     App.CloseFile fidPath &"FID.tnt": WScript.Sleep wait
86     ResFreq = getFIDresFreq() : WScript.Sleep wait: deleteFiles()
87
88     '#####'
89     '#####'
90     '**---Perform experiment---**'
91
92     i = 0
93     Do While (i<=exps)
94
95         IF i < 10 THEN
96             expInd = "_0" &i
97         ELSE
98             expInd = "_" &i
99         END IF
100
101
102     Data.OpenFile expPath &"FID_temp.tnt": WScript.Sleep wait
103     Data.SaveAs expPath &"current.tnt"
104     App.CloseFile expPath &"FID_temp.tnt": WScript.Sleep wait
105     Set Data = GetObject(App.GetActiveDocPath)
106
107     Data.SetNMRParameter "Observe Freq." ,ResFreq
108     Data.SetNMRParameter "pulseWidth" ,pws(i)
109
110         runAndSave()
111
112     Data.SaveAs expPath &"timeCal" &expInd &".tnt"

```

```

113             App.CloseFile expPath &"timeCal" &expInd &".tnt"
114
115     i = i + 1
116 Loop
117
118
119 '#####'
120 '#####'
121
122 '**---Funtions---**'
123 Function getFIDresFreq() '**---V1.2
124     set WshShell = WScript.CreateObject("WScript.Shell")
125     WshShell.Run "cmd": WScript.Sleep 100
126     WshShell.AppActivate "C:\Windows\system32\cmd.exe": WScript.Sleep 100
127     WshShell.SendKeys "cd C:\malone\javaOnly\{enter}": WScript.Sleep 100
128     WshShell.SendKeys "java -jar processFID1.jar {ENTER}": WScript.Sleep
        100
129     WshShell.SendKeys "exit{ENTER}": WScript.Sleep 100
130
131     WScript.Sleep 2000
132
133     Dim objFSO, strTextFile, strData, strLine, arrLines
134
135     strTextFile = "C:\malone\javaOnly\result\resFreq.txt" 'name of the
        text file
136     Set objFSO = CreateObject("Scripting.FileSystemObject") 'Create a
        File System Object
137     strData = objFSO.OpenTextFile(strTextFile,1).ReadAll 'Open the
        text file - strData now contains the whole file
138     arrLines = Split(strData,vbCrLf) 'Split the text file into lines
139     getFIDresFreq = arrLines(0)
140     Set objFSO = nothing
141 End Function
142
143 Function deleteFiles()
144     dim filesys
145
146     Set filesys = CreateObject("Scripting.FileSystemObject")

```

```
147     If filesys.FileExists("C:\malone\javaOnly\data\FID.tnt") Then
148         filesys.DeleteFile "C:\malone\javaOnly\data\FID.tnt"
149     End If
150
151     If filesys.FileExists("C:\malone\javaOnly\result\resFreq.txt") Then
152         filesys.DeleteFile "C:\malone\javaOnly\result\resFreq.txt"
153     End If
154 End Function
155
156
157 Function runAndSave()
158     IF (Running = 2) THEN
159         msgBox("advance?")
160     END IF
161
162     IF(Running=1) THEN
163         App.ZG
164         Do While Not Data.CheckAcquisition
165             Loop
166
167         App.Save
168     END IF
169 END Function
```

Appendix F: Java processing code: TecmagReader

F.1 Overview

A large Java code library called TecmagReader was written to process the volume of data that was collected. The idea behind TecmagReader was to create a scripting language that could process a collection of spectra. This was implemented by processing an object of the class Set, which was simply an array of TNT objects described in Appendix G.

An example of the TecmagReader code is given below. This particular program is designed to process the collection of FIDs, and their corresponding pulse shapes from the sniffer coil, to create a Result object: a simple text spreadsheet that could easily be read by Excel, OriginLab or other more specialized tools.

The goal of showing this snippet of code is to reveal the natural language nature of the TecmagReader code, should someone wish to implement it for their own project. However, no additional documentation is available, except for the particular code used to read the .tnt files given in Appendix G

The source code will be made available online at a later date through

http://physics.gmu.edu/~ksauer/mrl_index.htm

although no effort has been made to make it useable, and no guarantees are made regarding its functionality or utility. Additionally, certain functions (FFT, fitting) will be unavailable due to licensing issues.

F.2 Example Code

```
1 public class calibrationExampleCode
2 {
```

```

3     public static void main(String args[])
4     {
5         int files    = 7;
6         int lineWidth = 160;
7         int leftShift = 20;
8
9         String path = "Y:\\paper2\\tuningX\\";
10
11        Set fids    = Set.readNumberedFiles(path + "ampCal_" , files);
12        Set sniff   = Set.readNumberedFiles(path + "sniffV_" , files);
13
14        Result data = new Result();
15
16        sniff.leftShift(0);
17        sniff.plot(1);
18        sniff.fourierTransform(1);
19        sniff.calcPhase();
20        double[] phases = sniff.getPhase();
21        sniff.phaseData(phases);
22        int[] peaks = sniff.getPeakLocation(100);
23
24        data.add(new Result(sniff.getTypeAt(peaks, "R"), "sniff_Real", 1));
25
26        fids.reportFID(4, leftShift, lineWidth, 16384, 40,
27            100e-6).print(0,0);
28        fids.removeOffset(fids.getOffset(8));
29        fids.leftShift(leftShift);
30        fids.zerofill(16384);
31        fids.exponentialMultiply(lineWidth);
32        fids.fourierTransform(1);
33        fids.calcPhase();
34        phases = fids.getPhase();
35        fids.phaseData(phases[0]);
36        peaks = fids.getPeakLocation(1);
37
38        data.add(new Result(fids.getTypeAt(peaks, "R"), "fid_Real", 1));
39        data.add(new Result(fids.getFFTnoise("R"), "error", 1));
40        data.add(new Result(fids.getTypeAt(peaks, "I"), "fid_Imag", 1));

```

```
40     data.add(new Result(fids.getFFTnoise("I"), "error",1));
41     data.print(0,0);
42 }
43 }
```

Appendix G: A .tnt reader

G.1 Overview

Below is a Java program that reads a set of variables from the *.tnt Tecmag file format and places them into a TNT object. This program has been heavily updated from the original code written by Martin Anderson.

G.1.1 TNT Class

A section of the TNT class that holds the data.

```
1 public class TNT
2 {
3     private double[] real; //real component of the .tnt file
4     private double[] imag; //imaginary component of the .tnt file
5     private double freq; //observation frequency of the .tnt file
6     private double fileTime; //operating system's file creation time
7     private double phase; //tracks phase adjustments to signal
8     private double tDwell; //the dwell time
9     private boolean fft; //tracks if data in time or freq domain
10    private int[] scans; //array of points[1d, 2d, 3d, 4d]
11    private String date; //time and date of the .tnt data
12 }
```

G.1.2 TNTreader Class

The TNTreader class that actually reads the .tnt file.

```
1 import java.io.DataInputStream;
2 import java.io.File;
3 import java.io.FileInputStream;
4 import java.io.FileNotFoundException;
5 import java.io.IOException;
```

```

6 import java.nio.ByteBuffer;
7 import java.nio.ByteOrder;
8
9 /*
10  * @author Martin Anderson / updated by Michael Malone
11  */
12 public class TNTreader
13 {
14     public static void main(String[] args)
15     {
16         TNTreader reader = new TNTreader();
17
18         TNT tnt = reader.readFile("C:/example.tnt");
19         tnt.report();
20         System.out.println(tnt.getDateD());
21     }
22     /*
23      * Given a fully qualified file path, return a TNT data object.
24      */
25     public TNT readFile(String filePath)
26     {
27         TNT tnt = new TNT();
28
29         if (filePath.indexOf(".tnt" )==-1) filePath+="tnt";
30
31         try
32         {
33             // Create data input stream
34             DataInputStream dis = new DataInputStream(new
35                 FileInputStream(filePath));
36
37             // skip bool
38             dis.skipBytes(16);
39
40             // Determine tecmag structure length
41             int structureLength = getLEInt(dis);
42
43             // Skip techmag structure

```

```

43     //System.out.println("Skipping: " +
        dis.skipBytes(ntnmr.getTecmagStructLen()));
44     dis.skipBytes(structureLength + 4 + 4);
45
46     // Grab data length
47     int dataLength = getLEInt(dis);
48
49     // Yank all the RI pairs
50     double[][] data = new double[dataLength/8][2];
51     for(int i=0; i<(dataLength / 8); i++)
52     {
53         data [i][0] = getLEFloat(dis);
54         data [i][1] = getLEFloat(dis);
55     }
56     tnt.setData(data);
57
58     // Shut down the input stream
59     dis.close();
60
61     //Get last Modified Date from the file information
62     File f1 = new File(filePath);
63     tnt.setFileTime(f1.lastModified());
64
65     DataInputStream disT = new DataInputStream(new
        FileInputStream(filePath));
66     disT.skipBytes(20);
67     int[] scans = new int[4];
68     scans[0] = getLELong(disT);//20+4
69     scans[1] = getLELong(disT);//20+8
70     scans[2] = getLELong(disT);//20+12
71     scans[3] = getLELong(disT);//20+16
72     tnt.setScans(scans);
73
74     disT.skipBytes(36);//20+16+36 = 52
75     int scans1d = getLELong(disT);//20+16+36+4 = 20+56
76
77     disT.skipBytes(28);//20+56+28 = 20+76+8
78     tnt.setFreq(Math.round(getLEDouble(disT)*1000000));//20+76+40

```

```

79         disT.skipBytes(156); //20+76+164+32
80         tnt.setTDwell(getLEDouble(disT)); //20+76+164+64 = 324
81
82         disT.skipBytes(66); //20+76+164+128+2
83         int recGain = getLEShort(disT); //20+76+164+128+4 = 392
84
85         disT.skipBytes(492);
86         byte[] b = new byte[19];
87         disT.read(b);
88         String date = new String(b);
89         date = date.substring(0, date.lastIndexOf(':')+3);
90         tnt.setDate(date);
91
92         String report = " ";
93         report += "Freq: " + tnt.getFreq() + " ";
94         report += "tD: " + tnt.getTDwell() + " ";
95         report += "Rec Gain: " + recGain + " ";
96         report += "Scans: " + scans1d + " x ";
97         report +=
98             "["+scans[0]+", "+scans[1]+", "+scans[2]+", "+scans[3]+"]; ";
99         report += "Date: " + date + " ";
100        report += filePath + " ";
101        report += "File Time: " + tnt.getFileTime();
102
103        System.out.println(report);
104    }
105    catch (FileNotFoundException e)
106    {
107        e.printStackTrace();
108        System.out.println("Invalid file: " + e.getMessage());
109    }
110    catch (IOException e)
111    {
112        e.printStackTrace();
113        System.out.println("Problem reading file: " + e.getMessage());
114    }
115    return tnt;
116 }

```

```

116
117     private int getLEInt(DataInputStream dis) throws IOException
118     {
119         return getLittleEndian(dis,4).getInt();
120     }
121     private float getLEFloat(DataInputStream dis) throws IOException
122     {
123         return getLittleEndian(dis,4).getFloat();
124     }
125     private double getLEDouble(DataInputStream dis) throws IOException
126     {
127         return getLittleEndian(dis,32).getDouble();
128     }
129     private int getLELong(DataInputStream dis) throws IOException
130     {
131         return getLittleEndian(dis,4).getInt();
132     }
133     private int getLEShort(DataInputStream dis) throws IOException
134     {
135         return getLittleEndian(dis,2).getShort();
136     }
137     private ByteBuffer getLittleEndian(DataInputStream dis, int length)
138         throws IOException
139     {
140         byte[] value = new byte[length];
141         dis.read(value, 0, length);
142         ByteBuffer bb = ByteBuffer.wrap(value);
143         bb.order(ByteOrder.LITTLE_ENDIAN);
144         return bb;
145     }

```

Bibliography

Bibliography

- [1] B. H. Suits, “Nuclear quadrupole resonance spectroscopy,” in *Handbook of Applied Solid State Spectroscopy*, D. Vij, Ed. Springer, 2006.
- [2] J. B. Miller, “Nuclear quadrupole resonance detection of explosives: an overview,” pp. 801 715–801 715–7, 2011. [Online]. Available: + <http://dx.doi.org/10.1117/12.887213>
- [3] A. Garroway, M. Buess, J. Miller, B. H. Suits, A. Hibbs, G. Barrall, R. Matthews, and L. Burnett, “Remote sensing by nuclear quadrupole resonance,” *Geoscience and Remote Sensing, IEEE Transactions on*, vol. 39, no. 6, pp. 1108–1118, 2001.
- [4] J. Miller and G. Barrall, “Explosives detection with nuclear quadrupole resonance,” *American Scientist*, vol. 93, no. 1, p. 50, 2005. [Online]. Available: <http://dx.doi.org/10.1511/2005.1.50>
- [5] R. V. Pound, “Nuclear electric quadrupole interactions in crystals,” *Phys. Rev.*, vol. 79, pp. 685–702, Aug 1950. [Online]. Available: <http://link.aps.org/doi/10.1103/PhysRev.79.685>
- [6] H.-G. Dehmelt and H. Kruger, “Kernquadrupolfrequenzen in festem dichlorthylen,” *Naturwissenschaften*, vol. 37, no. 5, pp. 111–112, 1950. [Online]. Available: <http://dx.doi.org/10.1007/BF00623717>
- [7] R. A. Marino and S. M. Klainer, “Multiple spin echoes in pure quadrupole resonance,” *The Journal of Chemical Physics*, vol. 67, no. 7, pp. 3388–3389, 1977. [Online]. Available: <http://link.aip.org/link/?JCP/67/3388/1>
- [8] E. D. Ostroff and J. S. Waugh, “Multiple spin echoes and spin locking in solids,” *Phys. Rev. Lett.*, vol. 16, no. 24, pp. 1097–1098, Jun 1966.
- [9] S. Vega, *Advances in Magnetic Resonance*, 1st ed., J. S. Waugh, Ed. Academic Press, 1973.
- [10] ———, “Fictitious spin 1/2 operator formalism for multiple quantum NMR,” *The Journal of Chemical Physics*, vol. 68, no. 12, pp. 5518–5527, 1978. [Online]. Available: <http://link.aip.org/link/?JCP/68/5518/1>

- [11] R. S. Cantor and J. Waugh, "Pulsed spin locking in pure nuclear quadrupole resonance," *J. Chem. Phys.*, vol. 73, no. 3, p. 1054, Aug 1980.
- [12] J. Vanier, "Temperature dependence of the pure nuclear quadrupole resonance frequency in KClO_3 ," *Canadian Journal of Physics*, vol. 38, no. 11, pp. 1397–1405, 1960. [Online]. Available: <http://www.nrcresearchpress.com/doi/abs/10.1139/p60-146>
- [13] A. Ohte and H. Iwaoka, "A precision nuclear quadrupole resonance thermometer," *Instrumentation and Measurement, IEEE Transactions on*, vol. IM-25, no. 4, pp. 357–362, 1976.
- [14] G. B. Benedek and T. Kushida, "Precise nuclear resonance thermometer," *Review of Scientific Instruments*, vol. 28, no. 2, pp. 92–95, 1957.
- [15] S. A. Vierkötter, "A novel strain gauge for QNDE of composites," *AIP Conference Proceedings*, vol. 509, no. 1, pp. 2037–2044, 2000. [Online]. Available: <http://link.aip.org/link/?APC/509/2037/1>
- [16] Y. Ihara, Y. Kimura, K. Kumagai, E. Bauer, G. Rogl, and P. Rogl, "Local electric state of noncentrosymmetric superconductor $\text{Mo}_3\text{Al}_2\text{C}$ revealed by Mo NQR and NMR experiments," *Journal of Physics: Conference Series*, vol. 400, no. 2, p. 022033, 2012. [Online]. Available: <http://stacks.iop.org/1742-6596/400/i=2/a=022033>
- [17] S. Kitagawa, K. Ishida, K. Nakano, T. Yajima, and H. Kageyama, "*s*-wave superconductivity in superconducting $\text{BaTi}_2\text{Sb}_2\text{O}$ revealed by $^{121/123}\text{Sb}$ -NMR/nuclear quadrupole resonance measurements," *Phys. Rev. B*, vol. 87, p. 060510, Feb 2013. [Online]. Available: <http://link.aps.org/doi/10.1103/PhysRevB.87.060510>
- [18] W. M. Potteet, R. F. Tipsword, and C. D. Williams, "Pure nuclear quadrupole resonance in superconducting and normal double-hcp ^{139}La metal," *Phys. Rev. B*, vol. 1, pp. 1265–1266, Feb 1970. [Online]. Available: <http://link.aps.org/doi/10.1103/PhysRevB.1.1265>
- [19] R. Blinc, J. Seliger, A. Zidansek, V. Zagar, F. Milia, and H. Robert, " ^{14}N nuclear quadrupole resonance of some sulfa drugs," *Solid State Nuclear Magnetic Resonance*, vol. 30, no. 2, pp. 61 – 68, 2006. [Online]. Available: <http://www.sciencedirect.com/science/article/pii/S0926204006000142>
- [20] J. Barras, D. Murnane, K. Althoefer, S. Assi, M. D. Rowe, I. J. F. Poplett, G. Kyriakidou, and J. A. S. Smith, "Nitrogen-14 nuclear quadrupole resonance spectroscopy: A promising analytical methodology for medicines authentication and counterfeit antimalarial analysis," *Analytical Chemistry*, vol. 85, no. 5, pp. 2746–2753, 2013. [Online]. Available: <http://pubs.acs.org/doi/abs/10.1021/ac303267v>

- [21] T. Rudakov, P. Hayes, and J. Flexman, "Optimised NQR pulse technique for the effective detection of heroin base," *Solid State Nuclear Magnetic Resonance*, vol. 33, no. 3, pp. 31 – 35, 2008. [Online]. Available: <http://www.sciencedirect.com/science/article/pii/S0926204008000040>
- [22] J. P. Yesinowski, M. L. Buess, A. N. Garroway, M. Ziegeweid, and A. Pines, "Detection of ^{14}N and ^{35}Cl in cocaine base and hydrochloride using NQR, NMR, and SQUID techniques," *Analytical Chemistry*, vol. 67, no. 13, pp. 2256–2263, 1995. [Online]. Available: <http://pubs.acs.org/doi/abs/10.1021/ac00109a053>
- [23] J. Shinohara, H. Sato-Akaba, and H. Itozaki, "Nuclear quadrupole resonance of methamphetamine hydrochloride," *Solid State Nuclear Magnetic Resonance*, vol. 43-44, no. 0, pp. 27 – 31, 2012. [Online]. Available: <http://www.sciencedirect.com/science/article/pii/S0926204012000215>
- [24] B. Suits, A. Garroway, J. Miller, and K. Sauer, " ^{14}N magnetic resonance for materials detection in the field," *Solid State Nuclear Magnetic Resonance*, vol. 24, no. 2-3, pp. 123 – 136, 2003. [Online]. Available: <http://www.sciencedirect.com/science/article/pii/S0926204003000456>
- [25] R. M. Deas, I. A. Burch, and D. M. Port, "Detection of RDX and TNT mine-like targets by nuclear quadrupole resonance," pp. 482–489, 2002. [Online]. Available: + <http://dx.doi.org/10.1117/12.479120>
- [26] G. V. Mozzhukhin, S. V. Molchanov, G. S. Kupriyanova, A. V. Bodnya, V. V. Fedotov, H. Guoxin, J. Yanbo, R. Tianliang, and Z. Guojin, *The Detection of Industrial Explosives by the Quadrupole Resonance Method: Some Aspects of the Detection of Ammonium Nitrate and Trinitrotoluene*, 2009, p. 231.
- [27] J. A. S. Smith, "Nitrogen-14 quadrupole resonance detection of RDX and HMX based explosives," in *European Convention on Security and Detection, 1995*, 1995, pp. 288–292.
- [28] B. H. Suits and A. N. Garroway, "Optimizing surface coils and the self-shielded gradiometer," *Journal of Applied Physics*, vol. 94, no. 6, pp. 4170–4178, 2003. [Online]. Available: <http://link.aip.org/link/?JAP/94/4170/1>
- [29] B. Suits, A. Garroway, and J. Miller, "Noise-immune coil for unshielded magnetic resonance measurements," *Journal of Magnetic Resonance*, vol. 131, no. 1, pp. 154 – 158, 1998. [Online]. Available: <http://www.sciencedirect.com/science/article/pii/S1090780797913355>
- [30] S.-K. Lee, K. L. Sauer, S. J. Seltzer, O. Alem, and M. V. Romalis, "Subfemtotesla radio-frequency atomic magnetometer for detection of nuclear quadrupole resonance," *Applied Physics Letters*, vol. 89, no. 21, p. 214106, 2006. [Online]. Available: <http://link.aip.org/link/?APL/89/214106/1>

- [31] Y. Tan, S. Tantum, and L. Collins, “Kalman filtering for enhanced landmine detection using quadrupole resonance,” *Geoscience and Remote Sensing, IEEE Transactions on*, vol. 43, no. 7, pp. 1507–1516, 2005.
- [32] A. Jakobsson, M. Mossberg, M. Rowe, and J. Smith, “Exploiting temperature dependency in the detection of NQR signals,” *Signal Processing, IEEE Transactions on*, vol. 54, no. 5, pp. 1610–1616, 2006.
- [33] S. Somasundaram, A. Jakobsson, and N. Butt, “Countering radio frequency interference in single-sensor quadrupole resonance,” *Geoscience and Remote Sensing Letters, IEEE*, vol. 6, no. 1, pp. 62–66, 2009.
- [34] N. Butt and A. Jakobsson, “Efficient removal of noise and interference in multichannel quadrupole resonance,” in *Signals, Systems and Computers (ASILOMAR), 2011 Conference Record of the Forty Fifth Asilomar Conference on*, 2011, pp. 1072–1076.
- [35] K. Sauer, B. Suits, A. Garroway, and J. Miller, “Three-frequency nuclear quadrupole resonance of spin-1 nuclei,” *Chemical Physics Letters*, vol. 342, no. 3-4, pp. 362–368, 2001. [Online]. Available: <http://www.sciencedirect.com/science/article/pii/S0009261401006029>
- [36] D. Osokin and R. Khusnutdinov, “Two-frequency composite pulses in NQR,” *Applied Magnetic Resonance*, vol. 30, no. 1, pp. 7–11, 2006. [Online]. Available: <http://dx.doi.org/10.1007/BF03166977>
- [37] G. Mozzhukhin, B. Rameev, R. Khusnutdinov, N. Dogan, and B. Aktas, “Three-frequency composite multipulse nuclear quadrupole resonance technique for explosive detection,” *Applied Magnetic Resonance*, vol. 43, no. 4, pp. 547–556, 2012. [Online]. Available: <http://dx.doi.org/10.1007/s00723-012-0326-9>
- [38] G. Mozjoukhine, “The two-frequency nuclear quadrupole resonance for explosives detection,” *Applied Magnetic Resonance*, vol. 18, no. 4, pp. 527–535, 2000. [Online]. Available: <http://dx.doi.org/10.1007/BF03162299>
- [39] J. Pirnat, J. Luznik, and Z. Trontelj, “A study of continuous-wave two-frequency NQR,” *Applied Magnetic Resonance*, vol. 30, no. 1, pp. 43–53, 2006. [Online]. Available: <http://dx.doi.org/10.1007/BF03166981>
- [40] J. Luznik and Z. Trontelj, “The radiofrequency coil design and the signal intensity for continuous-wave NQR and NMR spectrometers,” *Journal of Magnetic Resonance (1969)*, vol. 30, no. 3, pp. 551 – 556, 1978. [Online]. Available: <http://www.sciencedirect.com/science/article/pii/0022236478902809>
- [41] D. W. Prescott, J. B. Miller, C. Tourigny, and K. L. Sauer, “Nuclear quadrupole resonance single-pulse echoes,” *Journal of Magnetic*

- Resonance*, vol. 194, no. 1, pp. 1 – 7, 2008. [Online]. Available: <http://www.sciencedirect.com/science/article/pii/S1090780708001705>
- [42] D. W. Prescott, M. W. Malone, S. P. Douglass, and K. L. Sauer, “Rabi and Larmor nuclear quadrupole double resonance of spin-1 nuclei,” *The Journal of Chemical Physics*, vol. 137, no. 21, p. 214201, 2012. [Online]. Available: <http://link.aip.org/link/?JCP/137/214201/1>
- [43] D. Prescott, “Nuclear Quadrupole Spin Dynamics: How Weak RF Pulses and Double Resonance Cross-Relaxation Contribute to Explosives Detection.” Ph.D. dissertation, George Mason University, 2010.
- [44] K. R. Thurber, K. L. Sauer, M. L. Buess, C. A. Klug, and J. B. Miller, “Increasing ^{14}N NQR signal by ^1H - ^{14}N level crossing with small magnetic fields,” *Journal of Magnetic Resonance*, vol. 177, no. 1, pp. 118 – 128, 2005. [Online]. Available: <http://www.sciencedirect.com/science/article/pii/S1090780705002429>
- [45] T. Rudakov and P. Hayes, “Cross-polarisation method for improvement of ^{14}N NQR signal detectability,” *Journal of Magnetic Resonance*, vol. 183, no. 1, pp. 96 – 101, 2006. [Online]. Available: <http://www.sciencedirect.com/science/article/pii/S1090780706002448>
- [46] J. Seliger and V. Zagar, “Double resonance detection of (mainly nitrogen) NQR frequencies in explosives and drugs,” in *Explosives Detection Using Magnetic and Nuclear Resonance Techniques*, ser. NATO Science for Peace and Security Series B: Physics and Biophysics, J. Fraissard and O. Lapina, Eds. Springer Netherlands, 2009, pp. 139–158. [Online]. Available: <http://dx.doi.org/10.1007/978-90-481-3062-7-9>
- [47] —, “New methods for detection of ^{14}N NQR frequencies,” *Applied Magnetic Resonance*, vol. 43, no. 4, pp. 469–484, 2012. [Online]. Available: <http://dx.doi.org/10.1007/s00723-011-0303-8>
- [48] D. Osokin, “Pulsed line narrowing in Nitrogen-14 NQR,” *physica status solidi (b)*, vol. 102, no. 2, pp. 681–686, 1980. [Online]. Available: <http://dx.doi.org/10.1002/pssb.2221020229>
- [49] —, “Coherent multipulse sequences in nitrogen-14 NQR,” *Journal of Molecular Structure*, vol. 83, pp. 243 – 252, 1982. [Online]. Available: <http://www.sciencedirect.com/science/article/pii/0022286082851880>
- [50] O. Zueva and A. Kessel, “Dynamic line narrowing of nuclear quadrupole resonance,” *Journal of Molecular Structure*, vol. 83, pp. 383 – 386, 1982. [Online]. Available: <http://www.sciencedirect.com/science/article/pii/0022286082852162>

- [51] M. M. Maricq, “Quasistationary state and its decay to equilibrium in the pulsed spin locking of a nuclear quadrupole resonance,” *Phys. Rev. B*, vol. 33, no. 7, pp. 4501–4513, Apr 1986.
- [52] V. T. Mikhaltsevitch and T. N. Rudakov, “Study of quasistationary and stationary states in the short-repetition-time sequences in the NQR of nitrogen,” *Solid State Nuclear Magnetic Resonance*, vol. 25, no. 1-3, pp. 99 – 111, 2004, 31st Congress Ampere, Magnetic Resonance and Related Phenomena. [Online]. Available: <http://www.sciencedirect.com/science/article/pii/S0926204003000833>
- [53] S. Meiboom and D. Gill, “Modified spin-echo method for measuring nuclear relaxation times,” vol. 29, no. 8, pp. 688–691, 1958. [Online]. Available: <http://dx.doi.org/doi/10.1063/1.1716296>
- [54] V. T. Mikhaltsevitch and T. N. Rudakov, “On the NQR detection of nitrogenated substances by multi-pulse sequences,” *physica status solidi (b)*, vol. 241, no. 2, pp. 411–419, 2004. [Online]. Available: <http://dx.doi.org/10.1002/pssb.200301930>
- [55] A. Gregorovic and T. Apih, “Relaxation during spin-lock spin-echo pulse sequence in ^{14}N nuclear quadrupole resonance,” *The Journal of Chemical Physics*, vol. 129, no. 21, p. 214504, 2008. [Online]. Available: <http://link.aip.org/link/?JCP/129/214504/1>
- [56] M. Engelsberg and C. S. Yannoni, “The determination of bond lengths in solids using the Carr-Purcell sequence,” *Journal of Magnetic Resonance (1969)*, vol. 88, no. 2, pp. 393 – 400, 1990. [Online]. Available: <http://www.sciencedirect.com/science/article/pii/002223649090198I>
- [57] M. J. Lizak, T. Gullion, and M. S. Conradi, “Measurement of like-spin dipole couplings,” *Journal of Magnetic Resonance (1969)*, vol. 91, no. 2, pp. 254 – 260, 1991. [Online]. Available: <http://www.sciencedirect.com/science/article/pii/0022236491901905>
- [58] T. Gullion, D. B. Baker, and M. S. Conradi, “New, compensated Carr-Purcell sequences,” *Journal of Magnetic Resonance (1969)*, vol. 89, no. 3, pp. 479 – 484, 1990. [Online]. Available: <http://www.sciencedirect.com/science/article/pii/0022236490903313>
- [59] J. Seliger, V. Zagar, R. Blinc, and F. Milia, “Temperature dependence of ^{17}O and ^{14}N NQR frequencies in commercial TNT,” *Applied Magnetic Resonance*, vol. 29, no. 4, pp. 541–548, 2005. [Online]. Available: <http://dx.doi.org/10.1007/BF03166330>
- [60] M. Buess and S. Caulder, “Factors affecting the NQR line width in nitramine explosives,” *Applied Magnetic Resonance*, vol. 25, no. 3-4, pp. 383–393, 2004. [Online]. Available: <http://dx.doi.org/10.1007/BF03166536>

- [61] S. Laks, A. Pelander, E. Vuori, E. Ali-Tolppa, E. Sippola, and I. Ojanper, “Analysis of street drugs in seized material without primary reference standards,” *Analytical Chemistry*, vol. 76, no. 24, pp. 7375–7379, 2004, pMID: 15595882. [Online]. Available: <http://pubs.acs.org/doi/abs/10.1021/ac048913p>
- [62] C. P. Slichter, *Principles of Magnetic Resonance*, 3rd ed. Springer-Verlag, Berlin ; New York :, 1990.
- [63] L. P. Gaffney and all, “Studies of pear-shaped nuclei using accelerated radioactive beams,” *Nature*, vol. 497, pp. 199–204, May 2013.
- [64] A. Abragam, *The Principles of Nuclear Magnetism*, 2nd ed. Clarendon, Oxford, 1961.
- [65] C. Cohen-Tannoudji, B. Diu, and F. Laloe, *Quantum mechanics*. Wiley New York, 1977. [Online]. Available: <http://www.loc.gov/catdir/toc/wiley023/76005874.html>
- [66] R. P. Feynman, F. L. Vernon, and R. W. Hellwarth, “Geometrical representation of the Schroedinger equation for solving maser problems,” *Journal of Applied Physics*, vol. 28, no. 1, pp. 49–52, 1957.
- [67] E. Fukushima and S. B. Roeder, *Experimental Pulse NMR: A Nuts and Bolts Approach*. Addison-Wesley Publishing Company, 1981.
- [68] S. Vega, “Theory of T_1 relaxation measurements in pure nuclear quadrupole resonance for spins $I = 1$,” *The Journal of Chemical Physics*, vol. 61, no. 3, pp. 1093–1100, 1974. [Online]. Available: <http://link.aip.org/link/?JCP/61/1093/1>
- [69] I. S. Gradshteyn and I. M. Ryzhik, *Table of Integrals Series and Products*, 4th ed. Academic Press, 1965.
- [70] M. T. Flanagan. Michael Thomas Flanagan’s Java Scientific Library. [Online]. Available: www.ee.ucl.ac.uk/mflanaga
- [71] [Online]. Available: <http://www.jfree.org/jfreechart>
- [72] M. Malone and K. Sauer, “Homocuclear dipolar coupling and CPMG spin-echoes in NQR,” *Applied Magnetic Resonance*, vol. 43, no. 4, pp. 541–546, 2012. [Online]. Available: <http://dx.doi.org/10.1007/s00723-012-0324-y>
- [73] M. W. Malone, M. McGillvray, and K. L. Sauer, “Revealing dipolar coupling with NQR off-resonant pulsed spin locking,” *Phys. Rev. B*, vol. 84, p. 214430, Dec 2011. [Online]. Available: <http://link.aps.org/doi/10.1103/PhysRevB.84.214430>
- [74] K. L. Sauer and C. A. Klug, “Spin dynamics in the pulsed spin locking of nuclear quadrupole resonance,” *Phys. Rev. B*, vol. 74, no. 17, p. 174410, Nov 2006.

- [75] E. W. Weisstein. Dirac matrices. [Online]. Available: <http://mathworld.wolfram.com/DiracMatrices.html>
- [76] K. Sauer, C. Klug, J. Miller, and A. Garroway, “Using quaternions to design composite pulses for spin-1 NQR,” *Applied Magnetic Resonance*, vol. 25, pp. 485–500, 2004, 10.1007/BF03166543. [Online]. Available: <http://dx.doi.org/10.1007/BF03166543>
- [77] T. N. Rudakov, V. T. Mikhaltsevich, and O. P. Selchikhin, “The use of multi-pulse nuclear quadrupole resonance techniques for the detection of explosives containing RDX,” *Journal of Physics D: Applied Physics*, vol. 30, no. 9, p. 1377, 1997. [Online]. Available: <http://stacks.iop.org/0022-3727/30/i=9/a=013>
- [78] G. Petersen and P. J. Bray, “ ^{14}N nuclear quadrupole resonance and relaxation measurements of sodium nitrite,” *The Journal of Chemical Physics*, vol. 64, no. 2, pp. 522–530, 1976. [Online]. Available: <http://dx.doi.org/doi/10.1063/1.432241>
- [79] K. L. Sauer, B. H. Suits, A. N. Garroway, and J. B. Miller, “Secondary echoes in three-frequency nuclear quadrupole resonance of spin-1 nuclei,” *The Journal of Chemical Physics*, vol. 118, no. 11, pp. 5071–5081, 2003. [Online]. Available: <http://dx.doi.org/doi/10.1063/1.1545442>
- [80] P. K. Kadaba, D. E. O’Reilly, and R. Blinc, “ N^{14} nuclear quadrupole resonance in ferroelectric NaNO_2 ,” *physica status solidi (b)*, vol. 42, no. 2, pp. 855–858, 1970. [Online]. Available: <http://dx.doi.org/10.1002/pssb.19700420243>
- [81] S. K. Song, B. S. Kim, T. H. Noh, Y. M. Park, I. Jeon, Y. M. Seo, and K. H. Kang, “NQR lineshape study of the local properties of disorder in solids,” *J. Korean Phys. Soc.*, vol. 36, no. 5, pp. 287–292, 2000.
- [82] R. Ambrosetti, R. Angelone, A. Colligiani, and A. Rigamonti, “ ^{14}N NQR and relaxation at the ferroelectric transition in NaNO_2 ,” *Phys. Rev. B*, vol. 15, no. 9, pp. 4318–4327, May 1977.
- [83] R. J. Karpowicz and T. B. Brill, “Librational motion of hexahydro-1,3,5-trinitro-s-triazine based on the temperature dependence of the nitrogen-14 nuclear quadrupole resonance spectra: the relationship to condensed-phase thermal decomposition,” *The Journal of Physical Chemistry*, vol. 87, no. 12, pp. 2109–2112, 1983. [Online]. Available: <http://pubs.acs.org/doi/abs/10.1021/j100235a017>
- [84] M. H. Levitt, “Composite pulses,” *Progress in Nuclear Magnetic Resonance Spectroscopy*, vol. 18, no. 2, pp. 61 – 122, 1986. [Online]. Available: <http://www.sciencedirect.com/science/article/pii/007965658680005X>
- [85] J. Trotter, S. H. Whitlow, and T. Zobel, “The crystal and molecular structure of p-chloroaniline,” *J. Chem. Soc. A*, pp. 353–356, 1966. [Online]. Available: <http://dx.doi.org/10.1039/J19660000353>

- [86] R. E. Sheriff and D. Williams, "Nuclear gyromagnetic ratios. iii," *Phys. Rev.*, vol. 82, pp. 651–655, Jun 1951. [Online]. Available: <http://link.aps.org/doi/10.1103/PhysRev.82.651>
- [87] G. B. Carpenter, "The crystal structure of sodium nitrite," *Acta Crystallographica*, vol. 5, no. 1, pp. 132–135, Jan 1952. [Online]. Available: <http://dx.doi.org/10.1107/S0365110X52000265>
- [88] R. Ambrosetti, A. Colligiani, P. Grigolini, and F. Salvetti, "Conformation of the NH₂ group in a single crystal of p-chloroaniline as determined by combined Zeeman effects on the ³⁵Cl and ¹⁴N nuclear quadrupole resonances," *The Journal of Chemical Physics*, vol. 60, no. 2, pp. 459–467, 1974. [Online]. Available: <http://link.aip.org/link/?JCP/60/459/1>
- [89] H. Goldstein, C. P. Poole, and J. L. Safko, *Classical Mechanics (3rd Edition)*, 3rd ed. Addison-Wesley, Jun. 2001. [Online]. Available: <http://www.worldcat.org/isbn/0201657023>
- [90] D. Bugg, *Electronics: Circuits, Amplifiers And Gates*. Taylor & Francis Group, 2006. [Online]. Available: <http://books.google.co.jp/books?id=9bhePeGfBhYC>

Curriculum Vitae

Michael Malone graduated with a B.A. from St. John's College (Annapolis) in 2004. He then spent the next four years as a research analyst at Fannie Mae developing consumer credit scores. He enrolled at George Mason University in 2008 and immediately began research with Dr. Karen L. Sauer in nuclear quadrupole resonance spectroscopy, focusing on the physics of pulsed spin locking. During his time at GMU he has published four papers, and attended four conferences, twice as a poster presenter and twice as an invited speaker.